Title

Functional Nanofiber Mats for Biomedical Applications via Coextrusion and Surface Initiated Polymerization

Author

Hochberg, Justin Davis

Publication Date

2022

Peer reviewed|Thesis/dissertation

UNIVERSITY OF CALIFORNIA SAN DIEGO

Functional Nanofiber Mats for Biomedical Applications via Coextrusion and Surface Initiated Polymerization

A Dissertation submitted in partial satisfaction of the requirements
for the degree Doctor of Philosophy

in

NanoEngineering

by

Justin Davis Hochberg

Committee in charge:

Professor Jonathan Pokorski, Chair
Professor Jinhye Bae
Professor Darren Lipomi
Professor Lisa Poulikakos
Professor Michael Sailor

2022

The Dissertation of Justin Davis Hochberg is approved, and it is acceptable in quality and form for publication on microfilm and electronically.

University of California San Diego

2022

DEDICATION

To my family and friends that supported me throughout this process, particularly Mom and Dad. Thank you for being there for me during this endeavor. Thank you as well to my lab mates for all the support and friendship; and thank you to Jon for being such a kind and supportive mentor over the years.

EPIGRAPH

"I was told a million times of all the troubles in my way. Mind you grow a little wiser, little better every day. But if I crossed a million rivers and I rode a million miles. Then I'd still be where I started bread and butter for a smile. Well I sold a million mirrors in a shopping alley way. But I never saw my face in any window any day. Now they say your folks are telling you to be a super star. But I tell you just be satisfied, stay right where you are."

—Brian Harold May, Ph.D.

TABLE OF CONTENTS

LIST OF FIGURES

LIST OF TABLES

ACKNOWLEDGEMENTS

I would like to thank Professor Jonathan Pokorski for his mentorship and support since hiring me in 2017. Having an extremely supportive and kind mentor has made this long and challenging road much more pleasant and enjoyable than expected.

Professors Jinhye Bae, Darren Lipomi, Lisa Poulikakos, and Michael Sailor are thanked for their time and advice as members of the committee in charge.

I would like to acknowledge the members of the Pokorski Lab from 2017-2022, whose friendship and brains have helped me both in and out of the lab. Of particular thanks is David Wirth, whose engineering abilities have been paramount to designing the setup of many experiments. I would also like to acknowledge my undergraduate student Pooja Shah, for her long hours and hard work spent working with me.

I would like to thank my collaborators from the Adolphe Merkle Institute at the University of Friobourg: Dr. Giovanni Spiaggia, Professor Alke Fink, and Professor Barbara Rothen. I would also like to thank my collaborators from the UCSD Mechanical Engineering Department: Paula Kirya, Samantha Bordy, and Professor Lisa Poulikakos.

Chapter 2, in full, is a reprint of the material as it appears in Applied Polymer Materials, Hochberg, J.D.; Wirth, D.M.; Spiaggia, G.; Shah, P.; Rothen-Rutishauser, B.; Fink, A.; Pokorski, J.K., American Chemical Society, 2022. The dissertation author was the primary researcher and author of this paper.

Chapter 3, in full, is a reprint of the material as it appears in Macromolecular Bioscience, Hochberg, J.D.; Wirth, D.M.; Pokorski, J.K., Wiley, 2022. The dissertation author was the primary researcher and author of this paper.

Chapter 4, in part is currently being prepared for submission for publication of the material. Hochberg, J.D.; Wirth, D.M.; Pokorski, J.K. The dissertation author was the primary researcher and author of this material.

Chapter 5 contains unpublished material coauthored with Hochberg, J.D.; Kirya, P.; Bordy, S.; Poulikakos, L.; and Pokorski, J.K. The dissertation author was the primary author of this chapter.

VITA

2016 Bachelor of Science, in Biochemistry, University of Florida

2019 Master of Science, in NanoEngineering, University of California San Diego

2022 Doctor of Philosophy, in NanoEngineering, University of California San Diego

PUBLICATIONS

Hochberg, J.D.; Wirth, D.M.; Pokorski, J.K. "PET-RAFT to Expand Surface-Modification Chemistry of Melt Coextruded Nanofibers", 2022, In Preparation

Hochberg, J.D.; Wirth, D.M.; Pokorski, J.K. "Surface-Modified Melt Coextruded Nanofibers Enhance Blood Clotting In Vitro", Macromolecular Bioscience, 2022, DOI: 10.1002/mabi.202200292

Hochberg, J.D.; Wirth, D.M.; Spiaggia, G.; Shah, P.; Rothen-Rutishauser, B.; Fink, A.; Pokorski, J.K. "High Throughput Manufacturing of Antibacterial Nanofibers by Melt Coextrusion and Post-Processing Surface Initiated Atom Transfer Radical Polymerization", ACS Applied Polymer Materials, 2022, 4, 260 –269

Shin, M.; Hochberg, J.D.; Pokorski, J.K.; Steinmetz, N.F. "The Bioconjugation of Active Ingredients to Virus Nanocarriers is Enhanced by Preincubation with a Pluronic F127 Polymer Scaffold", ACS Applied Materials and Interfaces, 2021, 13, 59618–59632

Calvo, P. R.; Sparks, C. A., Hochberg, J., Wagener, K. B., Sumerlin, B. S. "Hyperbranched Bisphosphonate-Functional Polymers via Self-Condensing Vinyl Polymerization and Postpolymerization Multicomponent Reactions", Macromolecular Rapid Communications, 2021, 42, 6

Wirth, D.M.; Jaquez, A.; Gandarilla, S.; Hochberg, J.D.; Church, D.C.; Pokorski, J.K. "A Highly Expandable Foam for Lithographic 3D Printing", ACS Applied Materials and Interfaces, 2020, 12, 19033 –19043

FIELD OF STUDY

Major Field: NanoEngineering

Studies in Applied Polymer Chemistry
Professor Jonathan Pokorski

ABSTRACT OF THE DISSERTATION

Functional Nanofiber Mats for Biomedical Applications via Coextrusion and Surface Initiated Polymerization

by

Justin Davis Hochberg

Doctor of Philosophy in NanoEngineering

University of California San Diego, 2022

Professor Jonathan Pokorski, Chair

Serious injuries occur every day and while medical technology has improved greatly in recent years, people still experience severe complications including death. While preventing an injury is the best way to avoid complications, it is an unrealistic goal. The development of materials to lessen the negative consequences of a serious injury is a major focus of the biomaterials community, and while a variety of products have been commercialized recently, there is still a strong need for improvement.

Polymeric nanofibers have gained significant attention in the biomedical community and have shown great use in drug delivery, tissue engineering, and for use as advanced bandages. A high-throughput melt-processing technique was recently developed to produce polymeric nanofibers and is particularly useful for fabricating polyester-based materials. Subsequent photochemical modifications have shown great utility in producing functional nanofiber materials for use in a variety of biomedical applications.

Described herein is the development of functional poly(ε-caprolactone) nanofibers to aid in the wound healing process by imparting antibacterial and blood clot enhancing characteristics utilizing a *grafting-from* surface-initiated polymerization technique. Further work is shown on expanding the chemistries and capabilities of this technology to widen the breadth of useful applications.

CHAPTER 1: INTRODUCTION

1.1 Polymeric Nanofibers: Polymeric nanofiber materials have attracted the attention of many due to their use as scaffolds in the biomedical arena, specifically in areas such as wound-healing, where altering the surface characteristics of nanofibers can lead to excellent antibacterial effectiveness without compromising biocompatibility. Other common uses of polymeric nanofibers include drug delivery technology, whereby fibrous materials can provide low diffusion distances, as well as tissue engineering materials that make use of a high surface area to volume ratio, leading to high porosity and ample sites for cellular adhesion.[1–6] Polymer processing technology and surface modification chemistries have been significantly advanced in recent years due to the specific need for improvements in human health and the biomedical arena as a whole. These recent advances allow for the application of these technologies to fabricate effective wound healing materials with various active moieties and combined chemistries for the development of multifunctional wound healing materials.

There is a plethora of methods in the literature for nanofiber fabrication, and each of those methods brings their own unique advantages and disadvantages. The most widely used nanofiber fabrication technique is electrospinning (**Figure 1.1A**) due to its inexpensive and simple set up as well as the ability to control the dimensions of fibers down to the nanoscale.[4,7] The applications of electrospun nanofibers is vast, but the size and quality of these fibers is dependent on the environmental parameters of the electrospinning system such as temperature and relative humidity.[8,9] Additionally, electrospinning presents a low maximum throughput with a maximum rate of 200 g h^{-1} on commercial grade instruments, and far less on those feasible in a laboratory environment. These low rates severely limit the commercial translatability of this technique.[10] Various newer nanofiber fabrication methods exist as well but also have their inherent limitations.

Firstly, melt electrospinning requires a higher voltage while experiencing a lower throughput than traditional electrospinning (**Figure 1.1B**);[11] rotary jet spinning (**Figure 1.1C**) produces fibers with

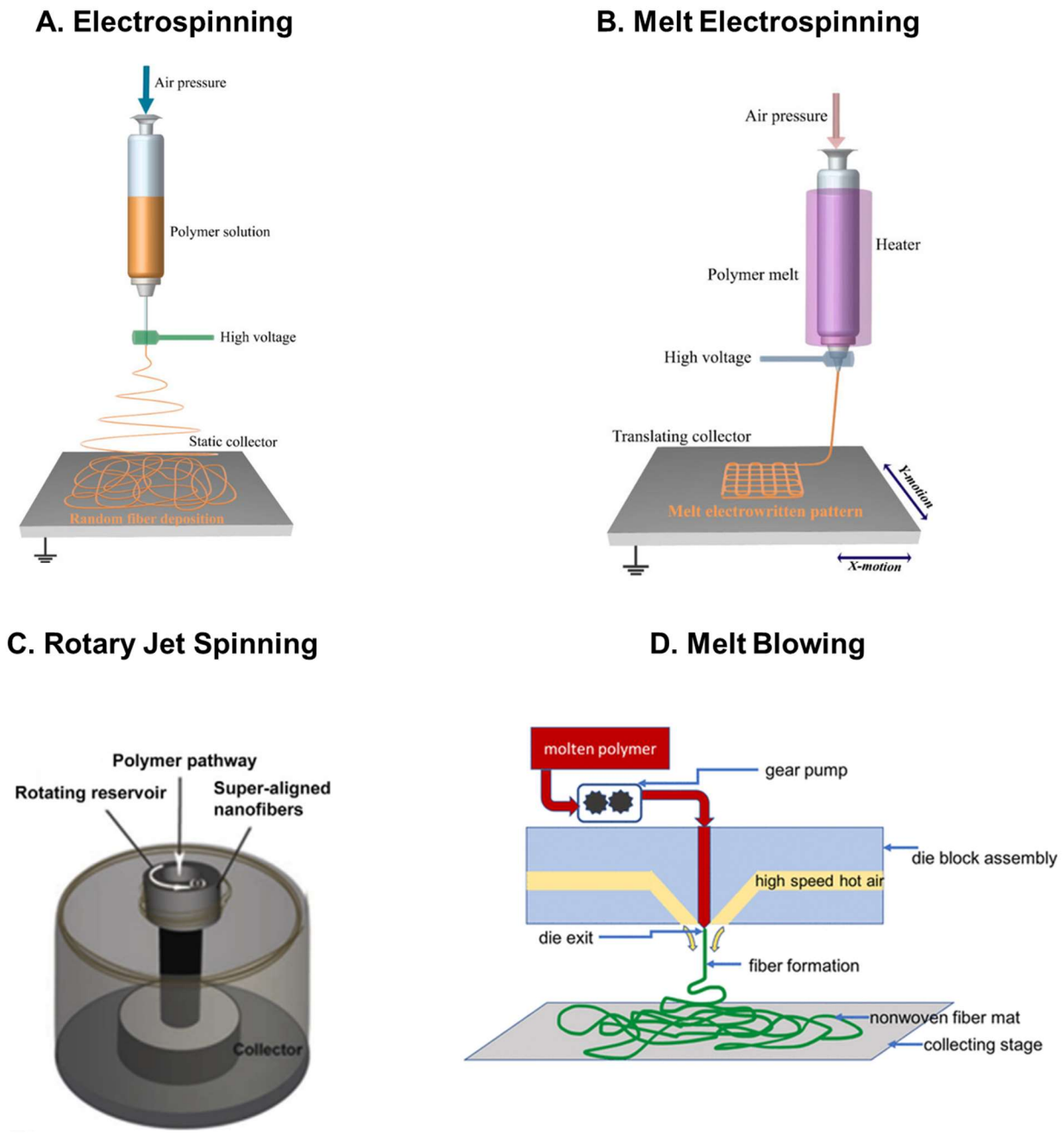

Figure 1.1: Methods of nanofiber functionalizatiom. (A) Electrospinning, (B) melt electrospinning, (C) rotary jet spinning, and (D) melt blowing. [A and B adapted from open-access article Afghah, F.; Dikyol, C.; Altunbek, M.; Koc, B. Biomimicry in Bio-Manufacturing: Developments in Melt Electrospinning Writing Technology Towards Hybrid Biomanufacturing. Appl. Sci. 2019, 9 (17), 3540. https://doi.org/10.3390/app9173540. C adapted with permission from Badrossamay, M. R.; Balachandran, K.; Capulli, A. K.; Golecki, H. M.; Agarwal, A.; Goss, J. A.; Kim, H.; Shin, K.; Parker, K. K. Engineering Hybrid Polymer-Protein Super-Aligned Nanofibers via Rotary Jet Spinning. Biomaterials 2014, 35 (10), 3188–3197. https://doi.org/10.1016/j.biomaterials.2013.12.072. Copyright 2022 American Chemical Society. D adapted with permission from Schmidt, J.; Shenvi Usgaonkar, S.; Kumar, S.; Lozano, K.; Ellison, C. J. Advances in Melt Blowing Process Simulations. Ind. Eng. Chem. Res. 2022, 61 (1), 65–85. https://doi.org/10.1021/acs.iecr.1c03444.. Copyright 2014 Elsevier.]

weak mechanical properties;[12,13] and fibers made via melt blowing are difficult to process into the nanometer regime (**Figure 1.1D**).[14] Melt coextrusion is a technique that has recently emerged as a nanofiber fabrication technique that is scalable, solvent-free, and easily yields nanoscale fibers.[15] Nanofibers produced via melt coextrusion have tunable cross-sectional dimensions and mechanical properties; and are made in a continuous, solvent-free process producing materials at a rate of 2 kg h^{-1} while using a laboratory scale instrument, significantly outperforming comparable electrospinning techniques. Melt coextrusion features two immiscible polymers entering the extrusion line together and undergoing layer rotation, vertical multiplication, surface layering, and horizonal multiplication steps (**Figure 1.2**).[15–17] Recent literature involving melt coextruded materials has shown applications for use as fuel filters,[18] antibacterial materials,[5] and biomedical scaffolds,[17,19] to name just a few.

1.2 Composition of Nanofibers: Most extrudable thermoplastics can be used in melt coextrusion to form nanofibers, but there are certain requirements when fabricating biomedical

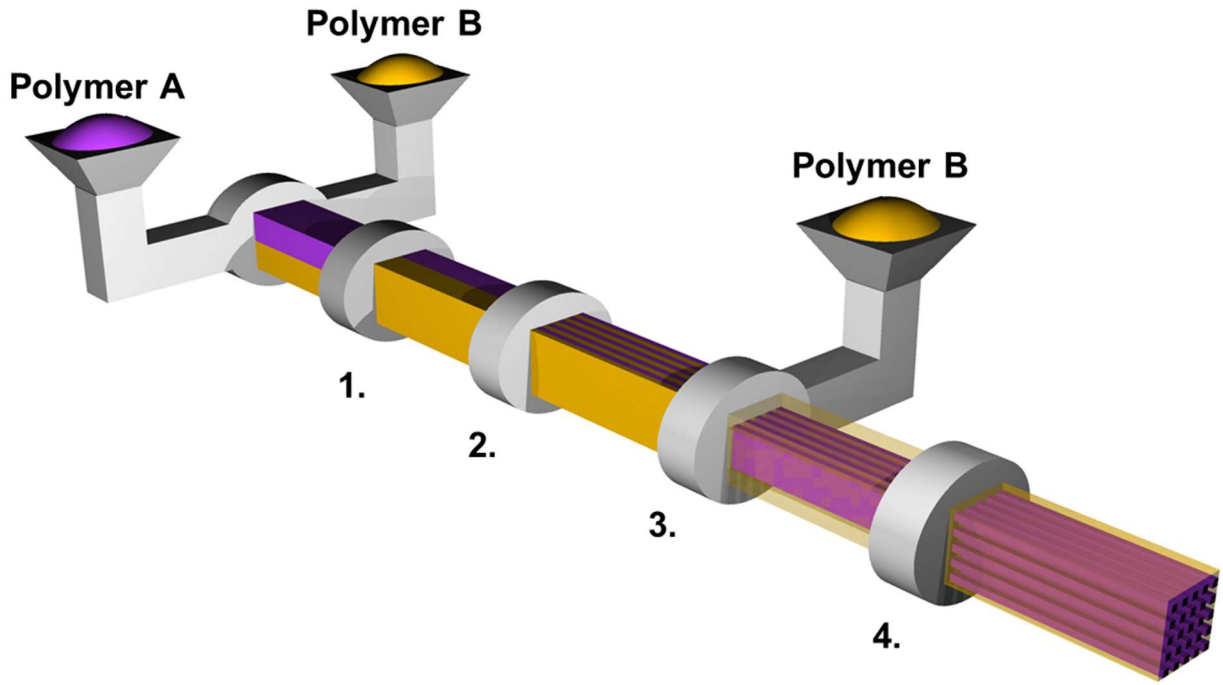

Figure 1.2: Schematic of melt coextrusion equipment and process featuring steps including (1) layer rotation, (2) vertical multiplication, (3) surface layering, and (4) horizontal multiplication steps

materials.[4,20] Firstly, nanofibers used in biomedical applications must have sufficient biocompatibility. Effective biomaterials cannot be cytotoxic nor induce or suppress the immune system in an undesirable manner.[21] Other useful characteristics considered include possessing favorable degradation kinetics, mechanicals properties, and the ability to chemically modify the materials.[4] A commonly used class of materials for biomedical applications include polyesters as they have been long-known to be non-cytotoxic and have long been used in FDA-approved devices.[22] Commonly used polyesters include poly(lactic acid) (PLA), poly(glycolic acid) (PGA), and poly(ε-caprolactone) (PCL). PCL in particular is known for its uncharacteristic flexibility, whereby it reaches more than 700% elongation at break, as well as its slow degradation rate of 2-3 years.[16,23,24]

1.3 Nanofiber Functionalization Methods: Polyester nanofibers do not inherently possess biologically active properties that would have sufficient utility in applications such as tissue engineering or wound treatment.[5,25] However, it is possible to improve the polyesters response in such instances by introducing biologically active moieties onto the surface of the nanofibers. There are numerous methods to functionalize nanofibers including end group modification (**Figure 1.3A**),[26] aminolysis (**Figure 1.3B**),[27] hydrolysis (**Figure 1.3C**),[28] and photochemical covalent

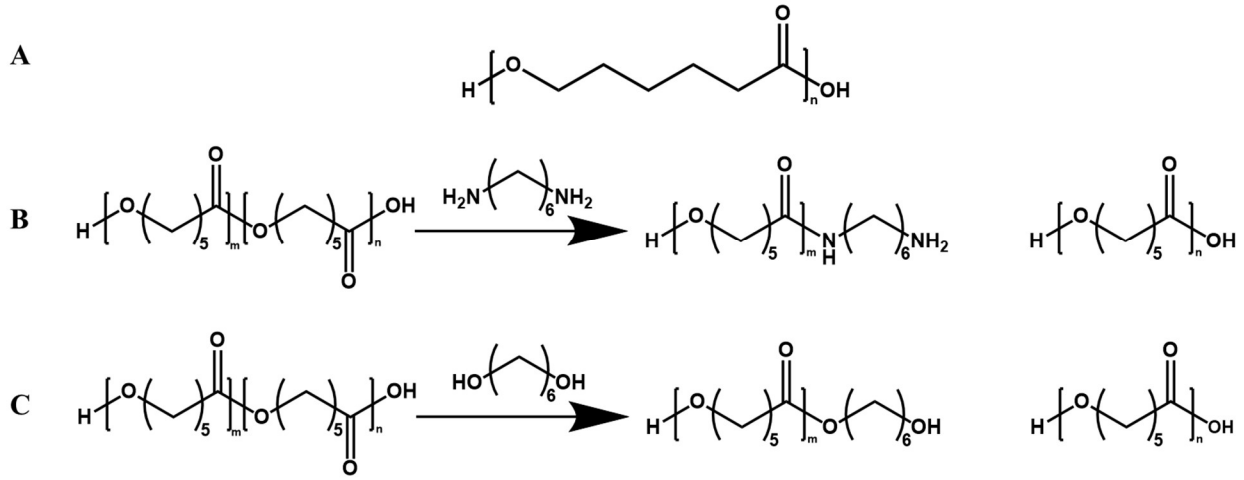

Figure 1.3: Examples of nanofiber functionalization techniques displaying active chain ends. (A) End group modification, (B) aminolysis, and (C) hydrolysis.

modification.[29] Chemical modifications of nanofibers allow for a much higher degree of functionalization as opposed to methods such as end group modification, aminolysis, and hydrolysis as it allows for functionality at every repeat unit in the polymer backbone. Have allowed for the development of various functional materials such as antifouling[30] and antibacterial nanofiber mats,[5] as well as the development of scaffolds for cellular adhesion, growth, proliferation, and differentiation mimicking the extracellular matrix (ECM).[7,17,20]

Chemically modifying nanofibers with polymers as opposed to small molecules can allow for a significant increase in available functional groups due to a large number of repeat units at the modified site. Two main approaches exist to covalently modify the surface of polymeric nanofibers with polymers. *Grafting-to* is a method where a polymer is first synthesized with a reactive chain end, then conjugated to an active group on the nanofiber surface (**Figure 1.4A**). This method allows explicit control over features such as the molecular weight and dispersity of the synthesized polymer, however steric interactions limit the grafting efficiency and in turn the number of functional units displayed on the material. To combat this low grafting efficiency, a *grafting-from* approach may be used (**Figure 1.4B**). Grafting polymers from a surface involves the conjugation

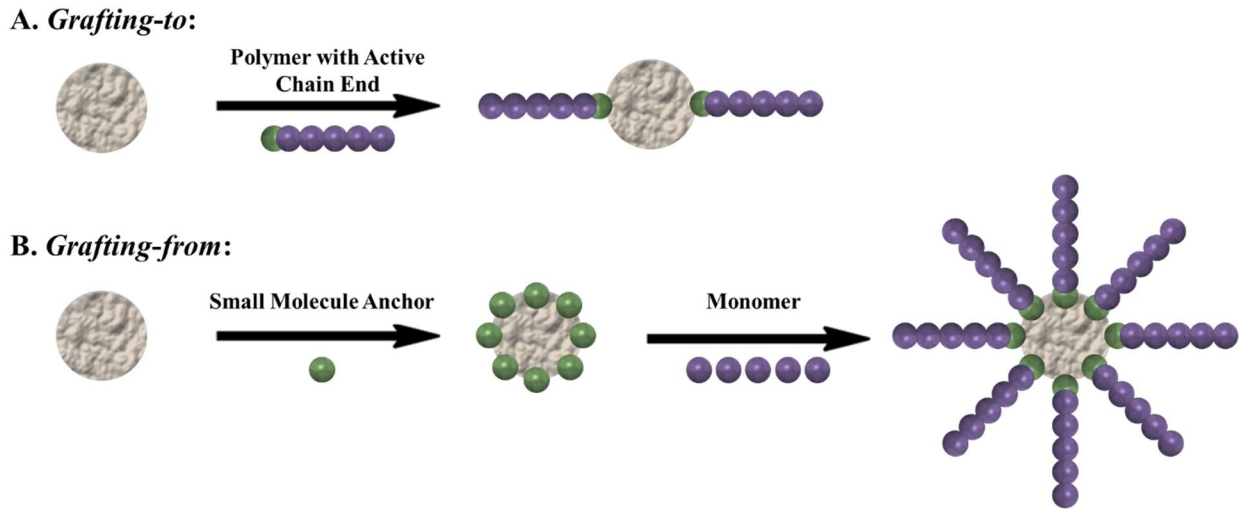

Figure 1.4: Process of grafting chemistries. (A) *grafting-to* and (B) *grafting-from*.

of a small molecule initiating group to said surface prior to polymerization. This allows for the polymerization to occur off of the material surface, negating the steric issues from the *grafting-to* method thus allowing for a higher modification density.[31]

1.4 Antibacterial Materials: The development of antibacterial materials is a promising direction for the future of nanofibers, as antibacterial materials are currently undergoing extensive research. Fibrous scaffolds could significantly progress the direction of this research and contribute to a major reduction in bacterial infections. According to the U.S. Centers for Disease Control and Prevention (CDC), more than 2.8 million infections and 35,000 deaths occur each year in the United States due to antibiotic resistant bacteria.[32] Preventing infections from occurring, whether from normal or antibiotic-resistant strains, is an important step in preventing unnecessary disease and death. Additionally, skin and soft tissue infections (SSTI) are a common type of bacterial infection that causes approximately 10% of hospitalizations in the United States.[33,34] Bacterial skin infections are commonly caused by bacteria including *Streptococcus pyogenes* (*S. pyogenes*) or *Staphylococcus aureus* (*S. aureus*), including antibiotic-resistant strains such as methicillin-resistant *Staphylococcus aureus* (*MRSA*).[35]

Antibacterial materials can prevent infections by killing skin-borne bacteria prior to the onset of a SSTI, thus avoiding systemic infection. There are three main mechanisms that antibacterial materials utilize to eliminate bacterial: (1) biocide-releasing materials, (2) materials that damage bacterial upon physical contact, and (3) materials decorated with cations.[36]

Biocide-releasing materials kill bacteria due to the release of antibacterial agents including silver,[37] chitosan,[38,39] or triclosan and cyclodextrin;[40] all of which are able to kill both Gram-positive and Gram-negative bacteria. Silver nanoparticles have been shown to kill bacteria from the leeching of silver ions off the nanoparticle surface, which interrupts ATP production and DNA

replication. Silver nanoparticles have been encapsulated in poly(vinyl alcohol)[41] and attached to the surface of nanofibers,[42] and have been shown to kill *S. aureus*, *Escherichia coli* (*E. coli*), and *Bacillus anthracis* (*B. anthracis*) in the latter. However, silver delays wound healing similarly by causing irritation and binding to DNA, inhibiting replication in mammalian cells in addition to bacterial cells.[36,37]

Contact killing kills bacteria by delivering a lethal mechanical force to the cells.[43] Single-walled carbon nanotubes (SWCNT) have been shown to kill bacteria in this approach. SWCNTs have been embedded into polysulfone nanofibers, and as the weight percent of the SWCNTs increased from 0.1% to 1.0%, the amount of dead *E. coli* increased from 18% to 76%. Bacterial toxicity levels however level out after 15 minutes, thus not killing all the bacteria present.[44]

The final method of introducing antibacterial properties onto materials involves decorating surfaces with cationic amphiphiles. Commonly used cationic amphiphiles include positively charged proteins/polypeptides and quaternary ammoniums. Antimicrobial peptides (AMPs) are a type of cationic amphiphile effectively used to kill antibiotic-resistant bacteria. AMPs are small biopolymers 20 −50 amino acids in length that selectively bind to and kill bacteria without harming eukaryotic cells when administered within a therapeutic limit.[45–48] AMPs normally display a net cationic charge at a physiological pH. Electrostatic interactions attract the positively charged AMPs to the negative charged bacteria, allowing hydrophobic units on the AMPs to compromise the integrity of the membrane of bacterial cells and leading to cell death.[46,48,49] AMPs have been widely used in a variety of applications such as incorporation into graphene−silver nanocomposites to disturb biofilms,[50] as well as being used to prevent the growth and biofilm formation of anaerobes commonly associated with orals diseases.[51] AMPs show exceptional antibacterial activity, but they are naturally produced in small amounts and are difficult and expensive to

synthesize. These challenges lead to the widespread development of synthetic polymers utilizing similar amphiphilic structures to AMPs.[48,52–55] These polymers have shown to be very effective, killing more than 99% of various bacteria including *S. aureus*, *E. coli*, Pseudomonas *aeruginosa* (*P. aeruginosa*), and *Vibrio cholerae* (*V. cholerae*).[52] Many of these synthetic polymers are also nontoxic to mammalian cells.[48]

1.5 Blood Clotting Materials: In addition to antibacterial properties, there are other useful wound healing properties available to implement upon polymeric nanofiber materials including blood clot enhancing effects, allowing for the development of hemostatic materials as a simple solution to hemorrhagic traumas. Hemorrhagic shock causes excessive blood loss causing insufficient oxygen delivery to organs and tissues. 60,000 deaths in the United States and 1.9 million deaths worldwide occur each year due to hemorrhaging.[56,57] After a vascular injury resulting in bleeding, the body's primary goal is to prevent further blood loss by "plugging the hole." This plug is accomplished via a gelation of the blood by the activation of a thrombin-mediated coagulation cascade. A series of enzyme-mediated reactions leads to the formation of a fibrin mesh at an injury site, leading to a stable blood clot. During a coagulation event, the formation of a blood clot occurs when fibrinogen is converted into fibrin, which is catalyzed with an enzyme known as thrombin. Fibrinogen is a 340 kDa homodimeric glycoprotein which circulates in the plasma of healthy individuals at high concentrations of 2-5 mg/mL. This concentration can exceed 7 mg/mL during acute inflammation. Fibrinogen is converted into the insoluble form polymerized form fibrin via a thrombin-mediated proteolytic cleavage and removal of N-terminal fibrinopeptides. These cleaved fibrin monomers then insert into another fibrin monomer to form protofibrils, which in turn aggregate into fibers forming a fibrin mesh that is necessary for the stability of a blood clot.[58–64]

Two primary mechanisms are available to induce that coagulation cascade. The first mechanism is the extrinsic, or tissue factor (TF) pathway. This pathway occurs in traditional hemostasis when cells that express a specific tissue factor protein encounter blood plasma, which triggers to onset of the coagulation cascade. The second mechanism of initiating this coagulation cascade is knowns as the intrinsic or contact pathway. This pathway occurs when blood plasma encounters certain types of artificial surfaces including diatomaceous earth, glass, or clay to name a few. When blood plasma comes into contact with one of these surfaces, a plasma protein known as factor XII changes conformation which in turn activates the coagulation cascade. The contact pathway does not promote natural hemostasis but does participate in thrombotic diseases.[65,66] Making use of the contact pathway allows for the chemical modification of a material that can trigger a desired coagulation event.

1.6 Multifunctional Nanofibers: As wound healing and biomedicine is multifaceted, there is a need to develop materials that can display multiple functionalities utilizing a variety of chemistries. This requirement ensures that the chemistries available can incorporate all possible needs of the material in question. Expanding the scope of chemistries available in the library of functionalization methods allows for the development of multifunctional nanofiber mats to cover all possible needs.

1.7 Conclusion: This dissertation describes the fabrication of functional PCL nanofiber mats via *grafting-from* polymerization techniques. The premise behind these modifications is the photochemical insertion of a functionalized benzophenone moiety into the PCL backbone of the nanofiber mats. Upon irradiation with ultraviolet light, the carbonyl pi bond between the phenyl rings splits into two active radicals. The oxygen centered radical abstracts a hydrogen from the PCL backbone leaving behind a radical cation. The benzophenone then inserts into the PCL via

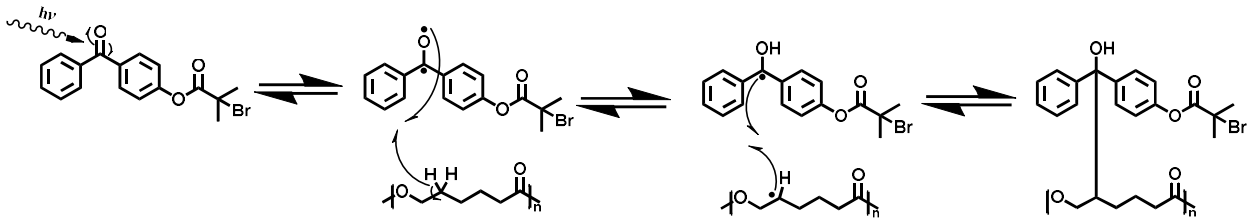

Figure 1.5: Mechanism of benzophenone-ATRP initiator insertion into the PCL backbone.

the benzophenone radical then combining radical cation of the PCL.[29,67,68] ^{1}H-NMR studies have determined that the ester directs benzophenone insertion into the δ-carbon.[69]

Figure 1.5 depicts the photochemical insertion of a benzophenone functionalized atom transfer radical polymerization (ATRP) initiator, which is the basis of much of the chemistry used herein. **Chapter 2** describes the fabrication of antibacterial nanofiber mats via both *grafting-from* and *grafting-to* ATRP techniques to demonstrate the superiority of *grafting-from* chemistries with functional biomaterials. These materials are tested against Gram-negative *E. coli* and Gram-positive *MRSA* to show the utility of overcoming a wide range of pathogenic bacteria, including antibiotic resistant strains while also maintaining biocompatibility.

Chapter 3 builds on these antibacterial devices to show that blood clotting functionalities can also be introduced to the nanofiber mats. Blood clotting functionalities are introduced via surface initiated ATRP and used to show the functional materials help create better blood clots by creating thicker fibrin clot strands, decreasing the time it takes for the onset of a blood clot, and increasing the concentration of thrombin.

Chapter 4 looks to expand the chemistries and capabilities of this technology by introducing photoinduced electron transfer reversible addition-fragmentation chain transfer (PET-RAFT) polymerization as the basis for the functional materials. PET-RAFT is a light-initiated controlled radical polymerization method that also allows for a simple method of functionalizing nanofiber. This method allows for the fabrication of nanofibers with a wide range of chemical

functionalities and once again yields a high grafting efficiency.[70–72] This technique can be conducted under metal-free conditions and in an oxygen containing environment. PET-RAFT has the added benefit of utilizing spatial patterning due to polymerization occurring only where light reaches. This utility also allows PET-RAFT to be used in conjunction with other polymerization chemistries, such as the previously described ATRP. First, a library of functionalities was polymerized off the surface to show the breadth of chemistry possible. Following these initial polymerizations, more complex experiments were done to showcase the use of these materials. These experiments include the functionalization of the nanofiber mats with block copolymers, utilizing ATRP and RAFT in an orthogonal manner, photopatterning, and lastly patterning cells as an initial dive into the tissue engineering capabilities of these materials. These experiments demonstrate the vast use and the future possibilities of the materials as wound healing devices and biomedical scaffolds.

Chapter 5 builds the foundation for future directions of these nanofiber materials. Correlating traditional polymer characterization techniques with polarized light-based experiments to model molecular alignment, utilizing a method more biocompatible than traditional methods will make fabricating and utilizing biomaterials much simpler, particularly in biosystems.

CHAPTER 2: High Throughput Manufacturing of Antibacterial Nanofibers by Melt Coextrusion and Post-Processing SI-ATRP

2.1 Abstract: Polymeric nanofiber scaffolds are widely used for drug delivery, tissue engineering, and as advanced bandages. A high-throughput melt-processing method to fabricate polyester nanofibers was recently developed, as well as subsequent photochemical modification to generate functional fibers for use in tissue engineering and filtration. This work builds on those processes and details methods to develop anti-bacterial nanofiber mats. Melt coextrusion was used to fabricate poly *(*ε-caprolactone*)* (PCL) nanofibers. The isolated fibers could then be modified using grafting-from or grafting-to strategies to install antimicrobial polymers on their surface. The antimicrobial mats derived from the grating-from strategy demonstrated superior antimicrobial activity against gram-positive and gram-negative bacteria, while maintaining biocompatibility. The work developed herein provides a scalable method to fabricate advanced, functional, nonwoven mats which show potential for use as advanced bandages.

Keywords: Nanofibers, Melt Coextrusion, SI-ATRP, Antibacterial, Biocompatibility

2.2 Introduction: Polymeric nanofibers have recently gained significant attention due to their use as scaffolds in biomedicine, particularly in the areas of tissue engineering, drug delivery, and wound healing.[1–4] Nanofibers have been fabricated by a variety of methods including electrospinning,[7] melt electrospinning,[11] melt blowing,[14] rotary jet spinning,[12,13] and melt coextrusion.[15] The diversity of methods employed implies that there are both advantages and drawbacks with each approach. The most commonly used fabrication technique, however, is electrospinning due to its simplistic design and its ability to control fiber dimension down to the nanoscale.[7] The quality of electrospun fibers significantly depends on the processing parameters

of the system[8,9] and the manufacturing method displays a relatively low throughput.[10] Less common fiber fabrication techniques, such as melt electrospinning, need high voltage while providing low throughput, melt blowing does not easily produce nanoscale fibers, and rotary jet spinning produces fibers with poor mechanical properties.[4,16]

Melt coextrusion has recently emerged as a nanofiber fabrication method that yields fibers with tunable mechanical properties and cross-sectional dimensions and is a continuous, solvent-free process that can produce mechanically robust nanofibers at a rate of 2 kg hr^{-1} when using a laboratory-scale extruder.[15–17] Melt coextrusion therefore offers a ten-fold increase in production rates as opposed to electrospinning nanofibers, which can only reach maximum production rates of 200 g hr^{-1}, without the need of organic solvents.[10] Nanofibers from melt coextrusion have been used in a variety of applications including as a scaffold for filtration media[30] and as a platform for neural growth and differentiation.[20] These nanofibers can be made from most extrudable thermoplastic polymers, however there are important considerations when designing biomedical materials. The primary focus for a biomaterial is its inherent biocompatibility, while secondary considerations may include mechanical properties or degradation kinetics, among others.[4] Polyesters such as poly(glycolic acid) (PGA), poly(lactic acid) (PLA), and poly (ε-caprolactone) (PCL) are non-cytotoxic and can even enhance cellular proliferation and differentiation upon chemical modification.[22,73,74] PCL specifically has a slow hydrolytic degradation rate of 2-3 years, is non-toxic, and is extremely flexible, being able to reach >700% elongation at breakage.[23,24]

A promising area for future nanofiber use is antibacterial materials. These materials are a tool currently undergoing intensive research and fibrous scaffolds could contribute significantly to a reduction in bacterial infections. According to the United States' Center for Disease Control and Prevention (CDC), more than 2.8 million infections and 35,000 deaths occur each year in the

United States due to antibiotic resistance.[32] An important step to prevent unnecessary disease and untimely death is to prevent infections, traditional and antibiotic resistant alike, from occurring in the first place. Furthermore, skin and soft tissue infections (SSTI) are one of the most common types of bacterial infections, where approximately 10% of hospitalizations in the United States of America are due to an SSTI.[33,34] Bacterial skin infections are commonly caused by *Streptococcus pyogenes* (*S. pyogenes*) or *Staphylococcus aureus* (*S. aureus*), including antibiotic resistant strains such as methicillin-resistant *Staphylococcus aureus* (*MRSA*).[35]

Antibacterial materials have the potential to mitigate the risk of infection by killing sufficient skin borne bacteria prior to SSTIs, which would ultimately reduce systemic infection. Three main methods exist in fabricating effective antibacterial materials: (1) biocide releasing materials, (2) materials that cause physical damage to bacteria on contact, and (3) materials decorated with cations.[36]

Biocide releasing materials are an effective method of killing bacteria due to their release of agents such as silver, triclosan and cyclodextrin,[40] or chitosan[38,39] which are effective at killing both gram-positive and gram-negative bacteria. Silver nanoparticles have been both encapsulated within (poly(vinyl alcohol))[41] and attached to the surface (polysulfone) of nanofibers,[42] the latter of which was shown to kill *Bacillus anthracis* (*B. anthracis*), *S. aureus*, and *Escherichia coli* (*E. coli*). Silver nanoparticles kill bacteria via the leeching of silver ions from the nanoparticle surface, which interrupts ATP production and DNA replication. Silver however delays wound healing by similarly causing irritation and binding to DNA, inhibiting replication in mammalian cells as well.[36,37]

Contact killing is a method of delivering a lethal mechanical force to bacteria.[43] Single walled carbon nanotubes (SWCNT) have been used to kill bacteria in this manner. One such

example is embedding SWCNTs into polysulfone nanofibers. As the weight percent of the CNTs increase from 0.1% to 1.0%, the amount of *E. coli* killed increased from 18% to 76%. However, bacterial toxicity levels out after about 15 minutes and does not completely eradicate the bacteria.[44]

The final common method to fabricate bactericidal surfaces is to decorate them with cationic amphiphiles such as positively-charged proteins/polypeptides and quaternary ammonium functionalities. Antimicrobial peptides (AMPs) are one class of these agents and have been used as an effective means of killing antibiotic resistant bacteria. They are small biopolymers consisting of 20-50 amino acids that selectively bind and kill pathogenic bacteria without harming eukaryotic cells when administered within a therapeutic limit.[45–48] AMPs typically exhibit a net cationic charge at physiological pH. Electrostatic interactions attract AMPs to bacteria[46,49] while hydrophobic units on the AMPs disrupt the integrity of the bacterial membrane leading to cell death.[48] AMPs have been used in a wide variety of applications including being incorporated in graphene-silver nanocomposites to disrupt biofilms[50] and to prevent growth and biofilm formation of anaerobes typically associated with oral diseases.[51] While AMPs show excellent antimicrobial activity, they are naturally produced in low amounts and expensive to synthesize. To combat these challenges, many groups have synthesized polymers with similar amphiphilic properties to the AMPs.[48,52–55] These polymers are extremely effective, often killing greater than 99% of bacteria, including *P. aeruginosa*, *E. coli*, *V. cholerae*, and *S. aureus*.[52] Many of these polymers are also non-toxic to mammalian cells.[48]

This manuscript describes the fabrication of antibacterial nanofiber mats via co-extrusion and post-processing chemical functionalization. Mats were initially fabricated using PCL, followed by two surface modification strategies to generate materials with antibacterial properties. The first strategy used surface-initiated atom transfer radical polymerization (SI-ATRP) to

decorate the nanofiber surface with two different AMP-like antimicrobial polymers[48,52] that are known to kill both gram-negative and gram-positive bacteria. SI-ATRP has been shown recently to have a variety of applications that include grafting hydrophobic polymer brushes on both organic and inorganic substrates via a water accelerated "paint-on" method[75] and fabricating zwitterionic polymer brushes with a controlled density and thickness on a polyacrylonitrile ultrafiltration membrane surface.[76] We then demonstrated that this *grafting-from* functionalization technique enhanced antibacterial activity when compared to a *grafting-to* method using the same polymers with varying molecular weights. While *grafting-to* allows for more control over polymer properties, *grafting-from* typically allows for a higher grafting efficiency,[31] thus allowing a higher degree of antimicrobial activity per unit area of the nanofiber mats. Lastly, we demonstrated high cytocompatibility of polymer modified fiber mats.

2.3 Materials and Methods:

2.3.1 Materials: Poly(ethylene oxide) (PEO) – POLYOX N80 - 200 kDa and POLYOX N10 - 100 kDa – were purchased from Dow Chemical. CAPA 6800 PCL – 80 kDa was purchased from The Perstorp Group. 4-hydroxybenzophenone was purchased from Acros Organics. 1-bromohexane and tris(2-dimethylaminoethyl)amine (Me_6TREN) were purchased from Alfa Aesar. 2-(dimethylamino)ethylmethacrylate (DEAEMA) and N-(3-dimethylaminopropyl)methacrylamide (DMAPMA) were purchased from Tokyo Chemical Industry (TCI). N-(3-aminopropyl)methacrylamide hydrochloride (APMA) was purchased from Chemscene. α-bromoisobutyryl bromide and copper (I) bromide were purchased from Aldrich Chemistry. Triethylamine (TEA) was purchased from VWR Life Science. OP50-1 *E.* coli were purchased from University of Minnesota Caenorhabditis Genetics Center. CA-MRSA USA 300 was obtained from the Zhang lab in the Nanoengineering Department at UCSD. Luria-Bertani

(LB) broth was purchased from Fisher BioReagents. Todd-Hewitt (TH) Broth was purchased from BD Biosciences. Yeast extract powder was purchased from MP Biomedicals. Viability/cytotoxicity assay kit for bacteria live and dead cells (containing DMAO and Ethidium Homodimer III (EthD-III)) was purchased from Biotium. In vitro mouse fibroblasts NIH/3T3, Dulbecco's Modified Eagle Medium (DMEM), penicillin/streptomycin solution, Calf Bovine Serum (CBS), Iron Fortified, and L-Glutamine solution were acquired from ATCC. Cytotoxicity Detection Kit for Lactate dehydrogenase (Catalyst, Diaphorase/NAD+ mixture, and Dye Solution INT and sodium lactate) were obtained from Sigma-Aldrich. Gibco™ Trypsin-EDTA (0.25%), phenol red and 4',6-Diamidino-2-Phenylindole, Dihydrochloride (DAPI) were acquired from ThermoFisher Scientific. TGF-beta1 DuoSet ELISA kit and Recombinant Mouse interferon-γ (IFN-γ) were both purchased from R&D Systems, Inc.

2.3.2 Instrumentation and Equipment: PEO was blended in a Haake Rheodrive 5000 twin screw extruder. Multilayer coextrusion was conducted on a custom-built, two-component system with a series of horizontal and vertical multipliers at Case Western Reserve University. A SereneLife SLPRWAS26 Compact Pressure Washer was used to remove excess PEO and entangle nanofibers to form mats. A CellScale Univert uniaxial testing apparatus was used for tensile tests. Nanofiber mats were shaped into a circular patch shape with Anytime Tools sharp 7/16” hollow punch. Illumination for benzophenone photo-insertion was conducted with an Omnicure Model S1500 Standard Filter 320-500 nm UV light source. Scanning electron microscopy (SEM) images were collected with a FEI Apreo LoVac FE-SEM while energy dispersive spectroscopy (EDS) data was collected with an Oxford Instruments X-Max 80 EDS detector. Water contact angle (WCA) measurements were taken with a ramé-hart Model 200 goniometer. X-ray photoelectron spectroscopy (XPS) data was collected with a Kratos Analytical AXIS Supra surface analysis

instrument. Nuclear magnetic resonance (NMR) data was collected with either a 300 or 600 MHz Bruker Avance III spectrometer. Optical density (OD) measurements were taken using a BioTek Synergy HT microplate reader. Confocal microscopy images were taken with Leica SP8 and Zeiss LSM 710 meta confocal microscopes. The absorbances of lactate dehydrogenase (LDH) and TGF-beta1 DuoSet ELISA assays were measured with a Bio-Rad Plate reader. Cells were counted using an EVE automated cell counter.

2.3.3 Methods

2.3.3.1 Melt Coextrusion of PCL/PEO fiber tapes: As previously described, two different molecular weights (200 kDa/100 kDa) of PEO in a 30/70 w/w% ratio were compounded to provide a rheological match to PCL at the coextrusion temperature.[16] PEO was dried prior to use at 40 °C for 48 hours. Compounding was performed in a twin screw extruder set to 140 °C , and the extrudate was then pelletized.[20] PEO and PCL pellets were then dried for an additional 48 hours at 40 °C. PCL fibers were then coextruded into a PEO matrix at 180 °C. The extrusion line consisted of 16 vertical and 4 horizontal multipliers and an encasement in a 33% PEO skin layer and exited through a 3" tape die. The extruded tape was then collected on a chill role at room temperature rotating at roughly 15 rpm.[30]

2.3.3.2 Removal of PEO to form Nonwoven PCL Mats: PEO/PCL tapes were secured in a beaker of stirring water. Water was replaced every hour for six hours. Fibers were then left overnight in a 70% MeOH/30% H_2O solution to remove PEO. Fibers were fixed to a fiberglass plate and covered with a wire mesh. Fibers were then washed with a pressure washer at its widest spray setting to remove the remaining PEO and entangle fibers. Fibers were punched into an 11 mm diameter circular shape with a hollow punching apparatus for subsequent chemical modification.

2.3.3.3 Fiber Photochemistry: Fiber mats (11 mm diameter, approximately 8 mg) were dipped into a 10 mg/mL solution of the benzophenone-ATRP initiator in methanol (*grafting-from*) or a 5 mg/mL solution of polymer in methanol (*grafting*-to) and dried overnight in a vacuum desiccator. Fibers were then subjected to a broadband 320-500 nm UV light with an intensity of 548 $\frac{mW}{cm^2}$ for 45 minutes per side. Following UV exposure, mats were washed with methanol and dried again overnight in a vacuum desiccator. Successful fiber functionalization was confirmed via XPS and SEM-EDS. Both initiator functionalized and *grafting-to* fibers were characterized via WCA.

2.3.3.4 *Grafting-from* ATRP: Monomer (1.39 mmol), Me_6TREN (4.8 mg, 0.027 mmol), dimethylformamide (1 mL), and 8 modified mats from **2.3.3.3** were added to a flame dried three-neck round bottom flask and purged with N_2. After 45 minutes, Cu(I)Br (2.0 mg, 0.014 mmol) is added under positive pressure and the reaction is left to proceed overnight at room temperature. Fibers were then removed and placed in an Erlenmeyer flask with MeOH and stirred for 1 hour followed by vacuum drying in a desiccator. Successful polymerization was confirmed via XPS and WCA.

2.3.3.5 Synthesis of Photoreactive QA Polymer for *Grafting-to*: QA monomer (225 mg, 0.695 mmol), Me_6TREN (2.4 mg, 0.014 mmol), dimethylformamide (0.45 mL), and benzophenone initiator (QA-small: 4.8 mg, 0.014 mmol; QA-medium: 2.4 mg, 0.007 mmol, QA-large: 1.2 mg, 0.03 mmol) were added to a flame dried three-neck round bottom flask and purged with N_2. After 45 minutes, Cu(I)Br (1.0 mg, 0.007 mmol) was added under positive pressure. Polymerization was left overnight at room temperature. Polymers were dialyzed in deionized water for 2 days followed by lyophilization.

2.3.3.6 Synthesis of Photolabile M30 Polymer for *Grafting-to*: APMA (50 mg, 0.280 mmol), DMAPMPA (28.0 mg, 0.164 mmol), Me_6TREN (1.5 mg, 0.009 mmol), dimethylformamide (0.45

mL), and benzophenone initiator (M30-small: 3.1 mg, 0.009 mmol; M30-medium: 1.5 mg, 0.004 mmol, M30-large: 0.8 mg, 0.002 mmol) are added to a flame dried three-neck round bottom flask and purged with N_2. After 45 minutes, Cu(I)Br (0.6 mg, 0.004 mmol) is added under positive pressure. Polymerization was left overnight at room temperature. Polymers were dialyzed in deionized water for 2 days followed by lyophilization. Fibers were then vacuum dried in a desiccator.

2.3.3.7 Bacterial Growth Measurements: *E. coli* and *MRSA* were cultured in LB broth and TH (TH) broth, respectively. *E. coli* with an optical density at 600 nm (OD600) of 0.01 were incubated for 24 hours at 37 °C with an 11 mm diameter polymer modified mat cut in half in 500 µL of LB broth in a 48 well plate. *MRSA* were similarly prepared with an OD600 of 0.025 and incubated for 24 hours at 37 °C with two 11 mm diameter polymer modified mats in 750 µL of TH broth supplemented with yeast extract in a 48 well plate. OD readings were taking at 1, 3, 6, 12, and 24 hours to show bacterial growth.

2.3.3.8 Bacterial Live/Dead Assay: Mats were incubated with bacteria as previously described in 2.3.10. After 24 hours, mats were removed from bacteria and treated with 70 µL of viability/cytotoxicity assay solution consisting of 9.1% DMAO, 18.2% EthD-III, and 72.7% 150 mM NaCl in sterile, deionized water for 15 minutes. Mats were then placed on glass microscope slides and imaged via confocal laser scanning microscopy scanning emissions at 530 nm (live cells) and 625 nm (dead cells).

2.3.3.9 Fibroblast culture on antimicrobial mats: Mouse fibroblasts (NIH/3T3) were cultivated in DMEM supplemented with 10 vol% CBS, 1 vol% penicillin/streptomycin and 1 vol% of L-Glutamine (cDMEM). NIH/3T3 were grown in T75 flasks maintained at 37 °C, with a relative humidity of 95 % and 5 % of CO_2, until reaching 80% confluency. Cells were then washed with

PBS (10 mL) and trypsinized with 1.5 mL Trypsin for 5 minutes. 3 mL of cDMEM were added to the cells, which were counted using automatic cell counter. Punctured mats of 32 mm^2 in surface area were placed in 96 well plates and covered with approximately 20.000 cells (625 cells/mm^2) in 0.3 mL of cDMEM. Control experiments without mats were also performed by growing cells in 96 well plates.

2.3.3.10 Lactate dehydrogenase (LDH) assay: Cellular viability was assessed by measuring the release of LDH into the supernatant as a result of cell membrane rupture using an LDH cytotoxicity detection kit at 24 and 48 hours of cell cultivation. At these time points, 100 µL supernatants were collected from NIH/3T3 cultured on antimicrobial mats as previously described in 2.3.12. Control cell cultures treated with 0.3 mL of 0.2 v/v % Triton X-100 in PBS served as a positive control for the LDH assay. 100 µL aliquots of each sample and 100 µL of the LDH assay kit were placed in a new 96 well plate. The absorbance at 630 nm of each sample was measured. The data of each measurement was normalized by the mean of the positive control's values.

2.3.3.11 Profibrotic response: Transforming growth factor-β1 (TGF-β1) released into the supernatants by cells was quantified by using the ELISA DuoSet Development diagnostic kit, following the manufacturer's protocol at 24 and 48 hours of cultivation. 1 µg/mL of interferon gamma in cDMEM was used as a positive control.

2.3.3.12 Cellular proliferation: Following 24 and 48 hours of cell growth, the cells were trypsinized with 100 µL Trypsin for 5 minutes and counted using an automatic cell counter. To confirm the effectiveness of the trypsinization procedure, mats were visualized by confocal microscopy to confirm 100% cell detachment. Samples were then washed 3 times with PBS and

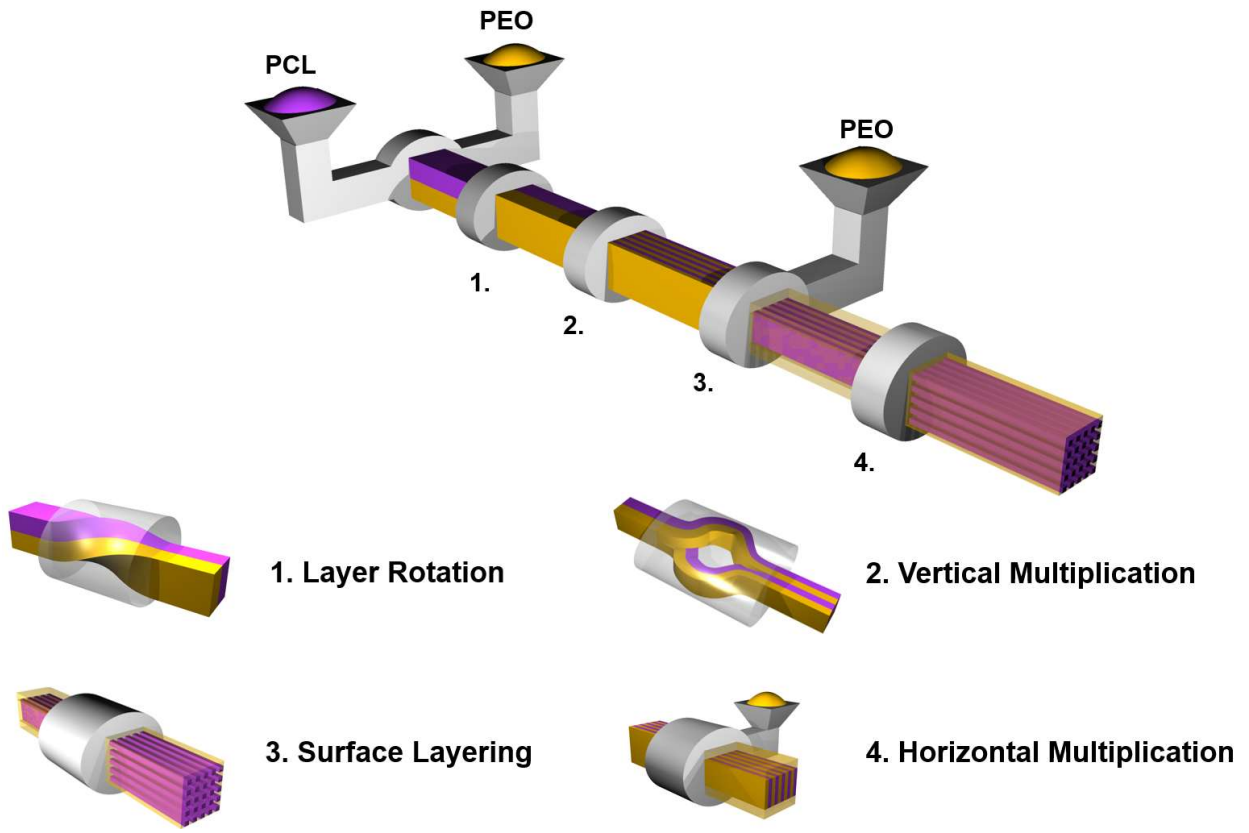

Figure 2.1: Schematic of melt coextrusion equipment and process featuring (1.1) layer rotation, (1.2) vertical multiplication, (1.3) surface layering, and (1.4) horizontal multiplication steps

fixed with a 4 vol% solution of paraformaldehyde for 15 minutes. After 3 additional washes, mats were immersed in DAPI (1:100 dilution in PBS) for 5 minutes to detect still adherent fibroblasts.

2.3.3.13 Statistical analysis: For the ELISA, LDH and cell proliferation analyses, three independent experiments were performed (three biological replicates). Statistical analysis was performed using GraphPad Prism 6 (GraphPad Software Inc., La Jolla, Ca) software. A parametric one-way analysis of variance (ANOVA) was performed. Results were considered significant if $p < 0.05$.

2.4 Results and Discussion

2.4.1 Melt Coextrusion and Fiber Mat Formation: PCL was chosen as the nanofiber material due to its biocompatibility, ductility, and ease of post-extrusion chemical modification. Melt coextrusion proceeded as previously described[20] and will be briefly described here. Coextrusion

begins by stacking PEO and PCL melts in layers oriented vertically to one another. This is followed by a 90° rotation that forces the melt flows side-by-side (**Figure 2.1.1**). The flow then feeds into a series of vertical multipliers; each multiplier doubles the number of layers; thus "n" number of multipliers results in 2^{n+1} total vertical layers (**Figure 2.1.2**). Following vertical layer multiplication, a 33% skin layer of PEO is pumped on the top and bottom of the melt (**Figure 2.1.3**), which is finally followed by a series of horizontal multipliers (**Figure 2.1.4**). This horizontal multiplication creates nanoscopic separated do mains of PCL embedded within the PEO matrix, yielding 2^{m} horizontal layers and 2^{n-m} vertical layers. This study used 16 vertical and 4 horizontal multipliers, producing 4096 x 16 PCL domains, results that were previously verified to be in the nanoscale regime.[77]

The resulting composite tapes were washed in a water bath for 6 hours, with the bath being replaced every hour, followed by a 70% MeOH bath overnight to remove PEO. Fiber preparation was completed by using a high-pressure water jet treatment, yielding a 98% removal of PEO (**Figure 2.S1**). This step also served to entangle the fibers to create a non-woven mat. These fiber mats were then stamped into circular mats with a diameter of 11 mm. Scanning electron microscopy (SEM) studies of fiber dimensions indicate a thickness of 0.78 ± 0.20 µm and a width

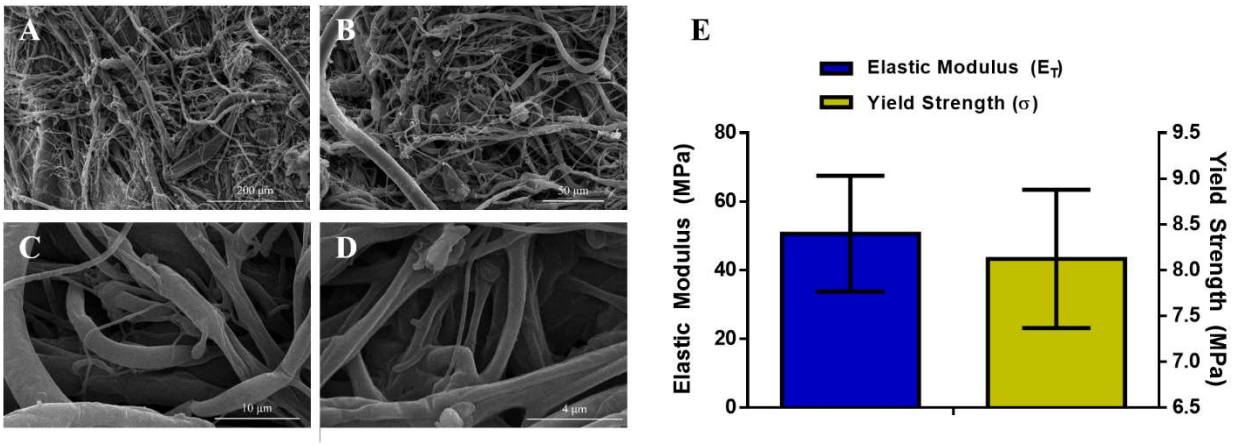

Figure 2.2: (A-D) Scanning electron micrograph of PCL nanofiber mat at various magnifications. Scale bar indicates (A) 200 µm, (B) 50 µm, (C) 10 µm, and (D) 4 µm (E) Elastic Modulus and Yield Strength of nanofiber mats.

of 0.38 ± 0.07 µm, averaged over 50 locations (**Figure 2.2A-D**). Uniaxial tensile testing of fiber mats demonstrated mechanical properties that were similar to our previously reported values,[16] displaying an elastic modulus (E_T) of 50.6 ± 16.9 MPa and a yield strength (σ) of 8.1 ± 0.8 MPa (**Figure 2.2E**). Archimedes' principle of buoyancy was used to determine the porosity of the nanofiber mats was 76.2 ± 3.9%, which is comparable to similar PCL nanofiber mats made via coextrusion.[30] The high porosity of our materials would be critical if applied for wound-healing because a highly porous system would allow for nutrient and gas exchange.[30]

2.4.2 Functionalization of Nanofibers via SI-ATRP: To functional polymers onto the nanofiber surface, we pursued two strategies, a *grafting-from* and a *grafting-to* approach (**Figure 2.3A and B**). A benzophenone-modified atom transfer radical polymerization (ATRP) initiator was synthesized for *grafting-from* modification (**Figures 2.S2 and 2.S3**). The benzophenone moiety is known to undergo a photoinitiated insertion into the PCL backbone for covalent

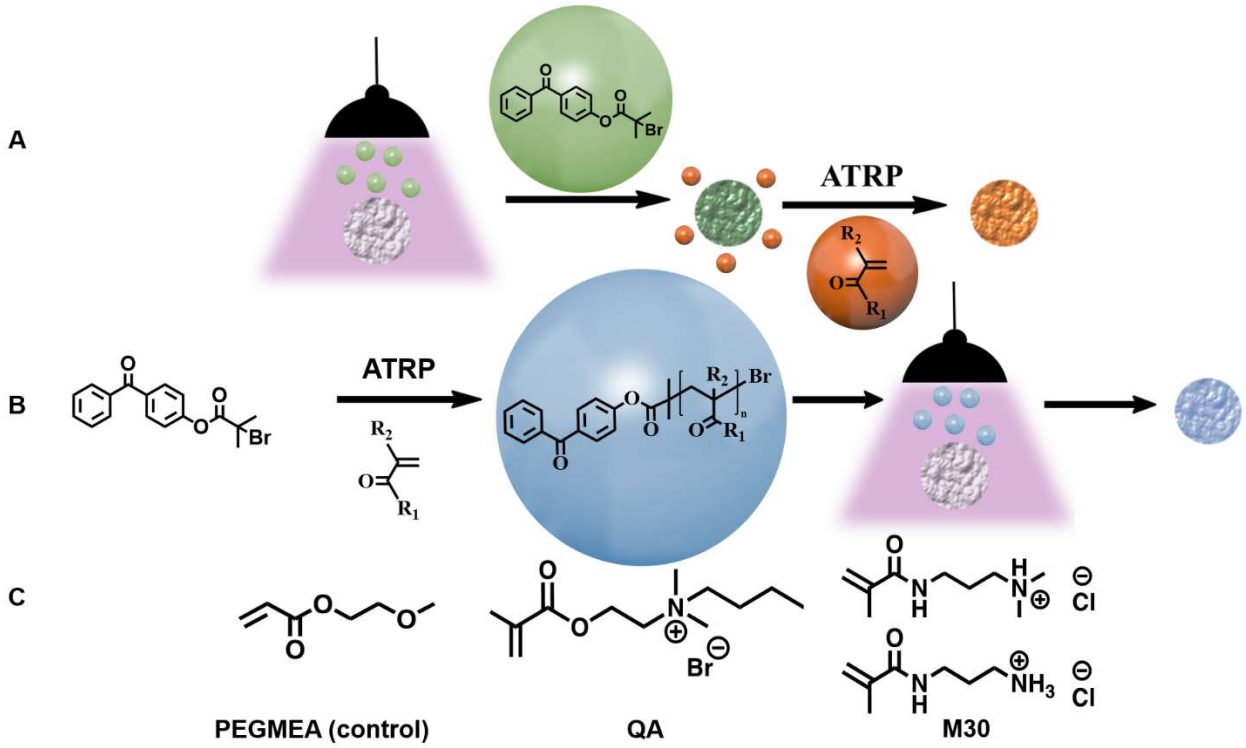

Figure 2.3: (A) Schematic diagram of *grafting-from* nanofiber mat functionalization. Mats are first exposed to initiator under UV light. Mats then undergo ATRP to functionalize them with polymers. (B) Schematic diagram of *grafting-to* nanofiber mat functionalization. Polymers are first synthesized via ATRP. Mats are then exposed to reactive polymer under UV light. (C) Chemical structures of monomers used mat functionalization.

modification of the fiber surface (**Figure 2.3A**).[29] Upon photochemical modification, an ATRP initiator remains exposed on the fiber surface. Surface-initiated ATRP (SI-ATRP) can then be used as a means of *grafting-from* the fiber with antimicrobial polymers.[78] The distinct incorporation of bromine from the initiator allows for confirmation of this attachment using a variety of methods including SEM-EDS (**Figure 2.S4**) and XPS, also a change in water-contact angle is seen from the unmodified nanofiber.

The modified fiber mats were used to initiate ATRP with a selection of cationic amphiphilic antibacterial (QA)[52] and (M30)[48] monomers, as well as a control monomer (PEGMEA) (**Figures 2.3C and 2.S5**). QA and M30 are both cationic amphiphiles with AMP-like properties. QA is methacrylate based and contains a positively charged quaternary amine, while M30 is a methacrylamide based copolymer containing units with both positively charged primary and tertiary amines. The rationale for the M30 copolymer is the increased bactericidal activity of a primary amine while the more hydrophobic tertiary amine decreases eukaryotic cytotoxicity. Both polymers have been shown to have bactericidal effectiveness against gram-positive and gram-negative bacteria. We chose these polymers due to their antibacterial efficacy and chemical compatibility with our desired synthetic methods.

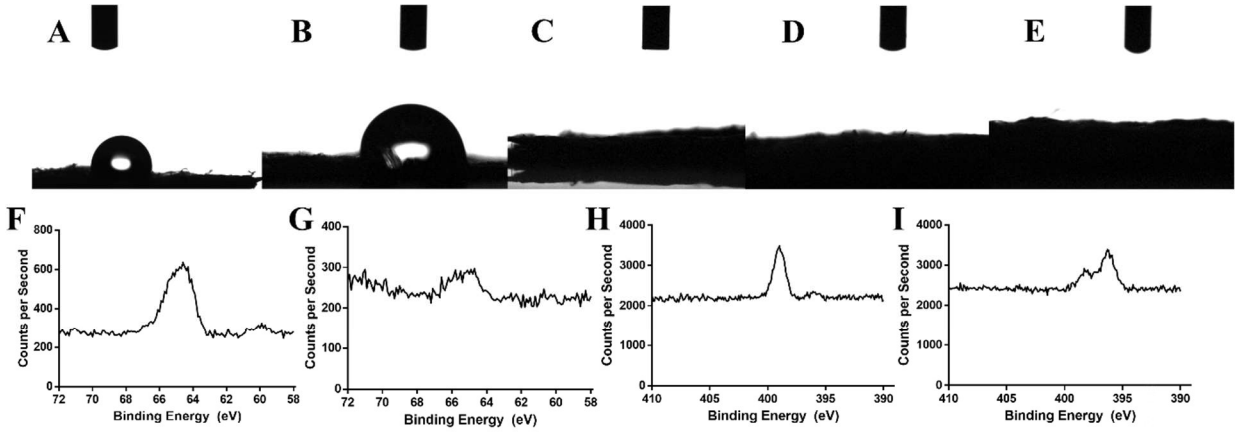

J

Fiber Sample	Percent Composition					WCA
	C	O	N	Br	Cl	
Unmodified PCL	61.1	38.9	0.0	0.0	0.0	83.7 ± 0.56°
Initiator	65.4	33.8	0.0	0.8	0.0	73.4 ± 1.55°
PEGMEA	49.1	50.8	0.0	0.1	0.0	0.0°
QA	59.3	35.0	2.1	3.6	0.0	0.0°
M30	55.1	39.8	1.9	1.9	1.3	0.0°

Figure 2.4: Surface characterization of functionalized nanofiber mats. Water contact angle measurements of (A) PCL, (B) initiator-functionalized, (C) PEGMEA, (D) QA, and (E) M30 nanofiber mats. High resolution XPS spectra of Br3d on (F) initiator functionalized and (G) PEGMEA nanofiber mats. High resolution XPS spectra of N1s on (H) QA and (I) M30 functionalized nanofiber mats. (J) Table of elemental composition from XPS and water contact angles of nanofiber mats.

Following ATRP, the mats were characterized using water contact angle, a simple method to determine surface energy between samples with differing chemistry. A slight decrease in water contact an gle, 83.7 ± 0.56° to 73.4 ± 1.55°, was observed upon functionalization of the PCL mat with the ATRP initiator (**Figure 2.4A-B**). The decrease in contact angle is due to an increased hydrophilicity of the fibers upon covalent attachment of the ATRP initiator. Following polymerizations, all fibers showed complete and immediate wetting (0°) (**Figure 2.4C-E**), attributed to the hydrophilicity of the PEG groups in the PEGMEA functionalized mats and the charged moieties in both the QA and M30 polymer-modified mats.

XPS was further used to characterize all fibrous samples to give information regarding the chemical makeup of the surface pre- and post-functionalization. XPS further demonstrated incorporation of bromine into the initiator-modified mats (**Figure 2.4F**) as evidenced by the presence of a bromine peak at 65 eV, characteristic of an electron being ejected from the 3d electron shell of a bromine atom. PEGMEA (**Figure 2.4G**) also shows a bromine peak that is

correlated to the end group of the polymer, but with a lower intensity than in **Figure 2.4F** due to the significantly increased proportion of carbon and oxygen atoms introduced upon functionalization with a PEG containing monomer. QA and M30 polymers both contain nitrogen in their monomer units, making this a unique signal for functionalization. QA functionalized mats demonstrate a single nitrogen peak at 399 eV and M30 mats have two unique peaks between 395-399 eV (**Figure 2.4H, 2.4I**). QA functionalized mats contain a single nitrogen peak since one distinct nitrogen appears in its chemical structure. M30 functionalized mats contain two separate nitrogen peaks, due to its composition of two chemically unique nitrogen atoms. The M30 cationic nitrogen is at a higher binding energy than its amide nitrogen. QA functionalized mats also feature a higher percentage of bromine as compared to the other mats, since bromine is a counterion. Likewise, M30 mats have a lower bromine content due to their chlorine counterion. All surface characterization is summarized in **Figure 2.4J**.

Thermogravimetric analysis (TGA) also confirms functionalization of the nanofiber mats via a slight mass loss in the QA and M30 mats upon heating. QA mats observe a 4.5% mass loss while M30 mats observe a 4.8% mass loss prior to the complete degradation of PCL as compared to the control PCL mats.

SEM studies were also conducted on the QA and M30 mats to determine if there are morphological changes upon chemical functionalization. According to the images acquired, there are no noticeable morphological changes to the PCL figures when functionalized with either QA and M30 polymers (**Figure 2.S7**).

2.4.3 Grafting-to Chemistry: As a comparison to the *grafting-from* method, antibacterial activity was compared with QA and M30 polymers conjugated to the PCL nanofiber mats via a *grafting-to* approach. *Grafting-to* chemistries are typically associated with a lower grafting

efficiency than *grafting-from* chemistries. As such, we were interested in investigating how this would affect the bactericidal capabilities of our nanofiber mats. QA and M30 polymers were synthesized under standard solution-based ATRP conditions using our benzophenone-based initiator in solution. Polymers were synthesized with varying theoretical degrees of polymerization (DP) (50 (small), 100 (medium), and 150 (large)) to evaluate potential effects of polymer length in addition to grafting density. Experimental DP values were obtained via NMR end-group analysis (**Figure S8**). QA values were 61, 144, and 208 for small, medium, and large, respectively. M30 values were 81, 141, and 188 for small, medium, and large, respectively. These polymers underwent the same photochemical insertion reaction (**Figure 2.3B**) and were inserted onto the surface of the PCL nanofiber mats. The *grafting-to* polymers mats were prepared in a 5 mg/mL solution of polymer in MeOH as opposed to a 10 mg/mL solution used in the *grafting-from* experiments because polymers were insoluble at that concentration.

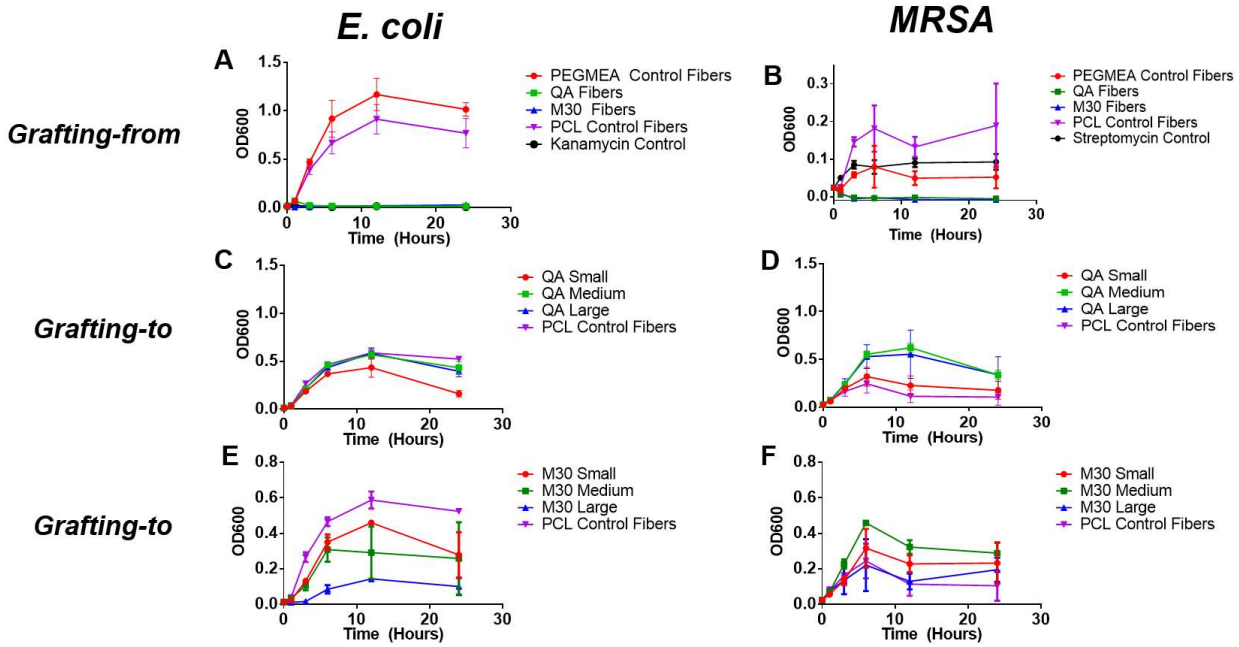

Figure 2.5: Optical density measurements at λ = 600 nm of incubations of (A), (C), and (E) with *E. coli* and (B), (D) and (F) with *MRSA*. (A) and (B) contain *grafting-from* mats while (C)-(F) contain *grafting-to* mats.

The mats were once again characterized using WCA and XPS (**Figures 2.S9 and 2.S10**). All QA and M30 mats showed the same 0° contact angle as the *grafting-from* mats, however it was observed that complete wetting was noticeably slower than it was for the *grafting-from* derived mats. XPS confirmed functionalization of all mats, although intensities were much lower than the *grafting-from* mats; too low on most to gather meaningful quantitative data. This lower intensity further confirms the lower efficiency of *grafting-to* versus *grafting-from* chemistries.

2.4.4 Antibacterial Activity: Antibacterial activity of the functionalized nanofiber mats was first studied by investigating the growth of bacterial cultures that were incubated with free polymers in solution to determine efficacy (**Figure 2.S11**). QA slows bacterial growth against *E. coli* at concentrations of 0.1 mg/mL and *MRSA* at concentrations of 0.5 mg/mL. M30 showed a decrease in bacterial growth against *E. coli* at concentrations of 1 mg/mL and *MRSA* at concentrations of 1 mg/mL. Solution experiments indicated that both polymers displayed antibacterial activity, with QA providing significantly enhanced efficacy against both gram-positive and gram-negative bacteria.

Following solution confirmation of antimicrobial activity, mats were evaluated for antibacterial activity. Mats were suspended in liquid cultures of *E. coli* and *MRSA* and were incubated for 24 hours; optical density measurements were taken at 600 nm (OD_{600}) at timepoints of 1, 3, 6, 12, and 24 hours. Throughout the 24-hour time course, both *E. coli* (**Figure 2.5A**) and *MRSA* (**Figure 2.5B**) showed no increase in optical density with *grafting-from* antibacterial mats, indicating that these mats successfully inhibited 100% of bacterial growth. Mats incubated with *E. coli* showed a significant difference between the antibacterial (QA and M30) mats as opposed to control mats (non-functionalized and PEGMEA functionalized mats), which experienced a significant amount of bacterial growth.

Mats incubated with *MRSA* showed less of a distinction between control and antibacterial mats. This is not surprising since the solution-based polymers were less potent antibacterial agents. As such, we used higher quantities of mats to elicit sufficient antibacterial activity (two 11 mm in diameter mats for *MRSA* versus one-half of a mat for *E. coli*). Using more material created an increase in bacterial fouling of the mats, therefore as the technology develops it may be warranted to include anti-fouling monomers in our coating as well. It is important to note that the antibacterial mats are more effective than using a common antibiotic with MRSA, indicating that these materials may overcome antibacterial resistance.

The *grafting-to* prepared fibers exhibited a modest degree of inhibition of *E. coli* growth but were significantly less efficacious than the SI-ATRP prepared mats (**Figure 2.5C-F**). The *grafting-to* PCL mats displayed an interesting phenomenon when incubated with *MRSA*, demonstrating less bacterial growth than the antibacterial mats. The PCL control mats fouled bacteria significantly more than the antibacterial mats, where the antibacterial mats seem to act in an antifouling manner. This is further amplified by the lower activity of the materials against

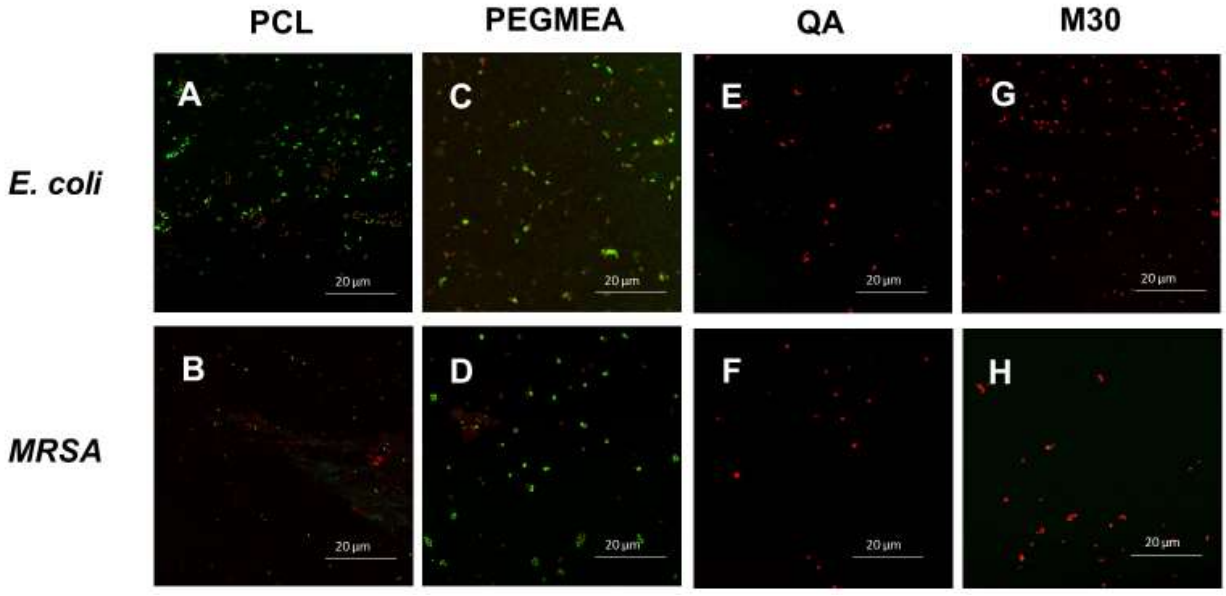

Figure 2.6: Antibacterial *grafting-from* fiber testing with E. coli (A,C,E,G) and MRSA (B,D,F,H) with live(green) and dead(red) stains after 24 hours of bacterial incubation. Imaged with confocal microscopy. (A,B) PCL, (C,D) PEGMEA, (E,F) QA, (G,H) M30.

MRSA, whereby two full mats were used in *MRSA* incubations as opposed to one-half of a mat for *E. coli*.

To confirm lack of bacterial growth was due to the mats being bactericidal and not just bacteriostatic, live/dead assays were performed on *grafting-from* mats to determine whether the antibacterial fibers were cytotoxic. Only the *grafting-from* mats were chosen due to their superior antibacterial efficacy. DMAO is a green fluorescent nucleic acid dye used to stain both live and dead bacteria, EthD-III is a red fluorescent nucleic acid dye that selectively stains dead bacteria. All control mats showed a roughly equivalent ratio of living to dead bacteria. Unmodified PCL mats showed 58.7% of *E. coli* survived (**Figure 2.6A**) while 50.4% of *MRSA* survived (**Figure 2.6B**). Comparatively, 60.0% of *E. coli* survived when incubated with the PEGMEA functionalized mats (**Figure 6C**) while 66.9% of *MRSA* survived (**Figure 2.6D**). Antibacterial nanofibers (QA and M30) showed 100% cytotoxicity after a 24-hour incubation with both *E. coli* and *MRSA* bacteria (**Figure 6E-H**).

2.4.5 Biocompatibility: To assess the biocompatibility of antibacterial mats, NIH3T3 fibroblasts were grown for 24 and 48 hours, followed by collection of the supernatant for an LDH

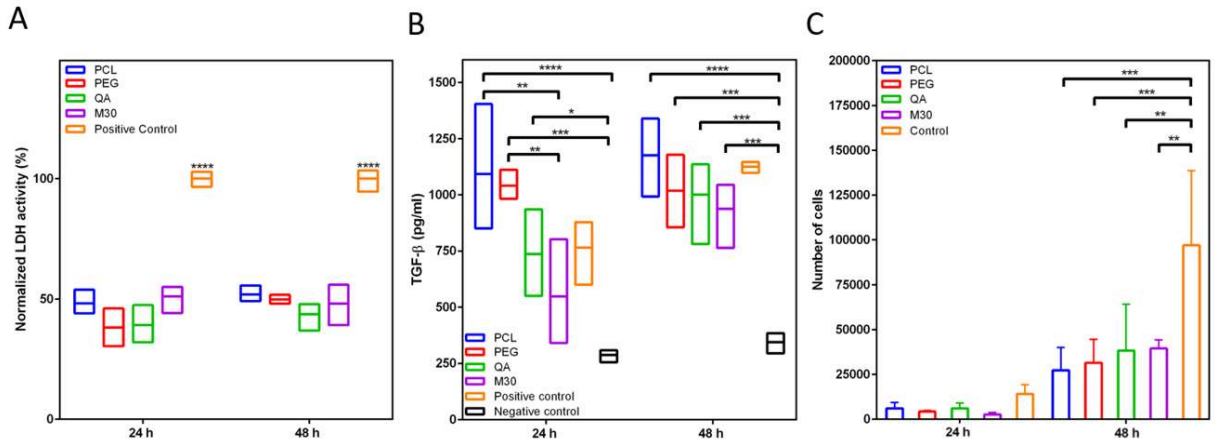

Figure 2.7: Biocompatibility study of antimicrobial mats (n = 3, 625 cells/mm^2). (A) Cell viability determined by LDH assay. (B) TGF-β secretion measurements. (C) Cell proliferation on mats.

assay. The data is represented relative to the positive control (cell cultures with Triton X-100 in PBS) Cytotoxicity tests show no significant differences among the LDH release of cells cultured on antimicrobial versus control mats (**Figure 2.7A**). This confirms that the PCL based substrates fabricated by extrusion were not cytotoxic to mammalian cells regardless of chemical modification.

2.4.6 Profibrotic Response and Cellular Proliferation: Studies have shown that TGF-β1 released by fibroblasts contributes to various cellular processes including differentiation, proliferation, migration and extracellular matrix remodeling. In particular, TGF-β1 influences the activation of fibroblasts into myofibroblasts, a cell phenotype with increased contractility and higher synthetic and secretory capabilities (e.g. collagens Type I, III, IV and V, fibronectins, proteoglycans and elastins). These responses are actively involved in tissues repair after injury.[79] Therefore, the secretion of TGF-β1 levels by fibroblasts in the supernatant was assessed together with the proliferation of cells on functionalized and non-functionalized mats after 24 and 48 hours of cultivation (**Figure 2.S12**). IFN-γ was used as positive control due to its involvement in the upregulation of TGF-β in dermal and corneal fibroblasts.[80] As shown in (**Figure 2.7B**), no statistically significant difference in TGF-β1 secretion by fibroblasts cultured on functionalized and non-functionalized mats was observed at both time points compared to the positive control, thus, confirming that all investigated samples stimulated cellular activation into myofibroblasts and their suitability as antimicrobial bandages.[81]

It is noteworthy to highlight that cells proliferated with a slower pace on non-functionalized mats (i.e; PCL and PEGMEA) compared to QA and M30 grafted substrates, by analyzing the number of trypsinized cells and having assessed the detachment efficacy (**Figures 2.7C and 2.S13**). This is in accordance with measured TGF-β1 secretion since it was reported how

myofibroblastic phenotype is correlated with major collagen synthesis but a reduction in cell proliferation.[82]

2.5 Conclusion: This study successfully demonstrated the fabrication of antibacterial nanofiber mats from a high-throughput melt coextrusion process. Following the photochemical insertion of an ATRP initiator, *grafting-from* polymerizations were shown to be significantly more effective than their *grafting-to* counterparts at successfully killing more than 99.9% of both gram-negative *E. coli* and gram-positive *MRSA*. Of importance is the fact that these materials are effective against antibiotic resistant bacteria. The mats still retained their biocompatibility and enhance the myofibrotic response by cultured fibroblasts. This *grafting-from* method was therefore more bactericidal and less toxic than other antibacterial materials, such as biocide releasing or those that use a contact killing mechanism. Future work will entail creating multifunctional fiber mats including antiviral, antifungal, and blood clotting agents to create multifaceted antimicrobial materials that are low-cost, simple to manufacture, and are a competitor to traditional first aid measures.

2.6 Acknowledgements: J. K. P., J. D. H., and D.M.W acknowledge NSF Partnerships for International Research and Education (PIRE) for financial support (OISE 1844463). The Zhang Group and Steinmetz Group are acknowledged for supplying bacterial stocks, the S. Chen Group is acknowledged for allowing access to the uniaxial testing apparatus. The Baer Group (Cong Zhang and Xiting Wang) is acknowledged for assisting with and providing access to melt coextrusion equipment. The Maia Group (Dana Klein) is acknowledged for assisting with and providing access to a twin-screw extruder. The authors acknowledge the use of facilities and instrumentation supported by NSF through the UC San Diego Materials Research Science and

Engineering Center (UCSD MRSEC) (Ricardo De-Luna), grant # DMR-2011924." The UCSD Microscopy Core (NS04701) is acknowledged for providing access to confocal microscopes.

Chapter 2, in full, is a reprint of the material as it appears in Applied Polymer Materials 2022. Hochberg, J.D.; Wirth, D.M.; Spiaggia, G.; Shah, P.; Rothen-Rutishauser, B.; Fink, A.; Pokorski, J.K., American Chemical Society, 2022. The dissertation author was the primary researcher and author of this paper.

2.7 Supporting Information

2.7.1 Mechanical Testing: Tensile tests were conducted with a 100 N load cell at a strain rate of 10 $\frac{mm}{min}$ to record the stress response to an applied strain on non-woven mats. Elastic modulus (E_T) and yield strength (σ) were measured. To account for void volume in the measured samples, an effective cross-sectional area was determined (σ_{CS}).

$$\boldsymbol{\rho = \frac{m}{V}} \ \mathbf{(1)}$$

$$\mathbf{V = lwt} \ \mathbf{(2)}$$

$$\boldsymbol{\sigma_{cs} = wt} \ \mathbf{(3)}$$

$$\mathbf{V = l(\sigma_{cs})} \ \mathbf{(4)}$$

$$\boldsymbol{\rho = \frac{m}{l(\sigma_{cs})}} \ \mathbf{(5)}$$

$$\boldsymbol{(\sigma_{cs}) = \frac{m}{(l)(p)}} \ \mathbf{(6)}$$

This effective cross-sectional area was compared with the density (ρ) of a solid PCL film (ρ = 1.145 g cm^{-3}) (**Equation 1**) and the volume of a rectangular prism (V) (**Equation 2**) to make the effective cross-sectional area equal to the mass of the sample divided by the sample length (l) and density of a solid PCL film (**Equations 3-6**).

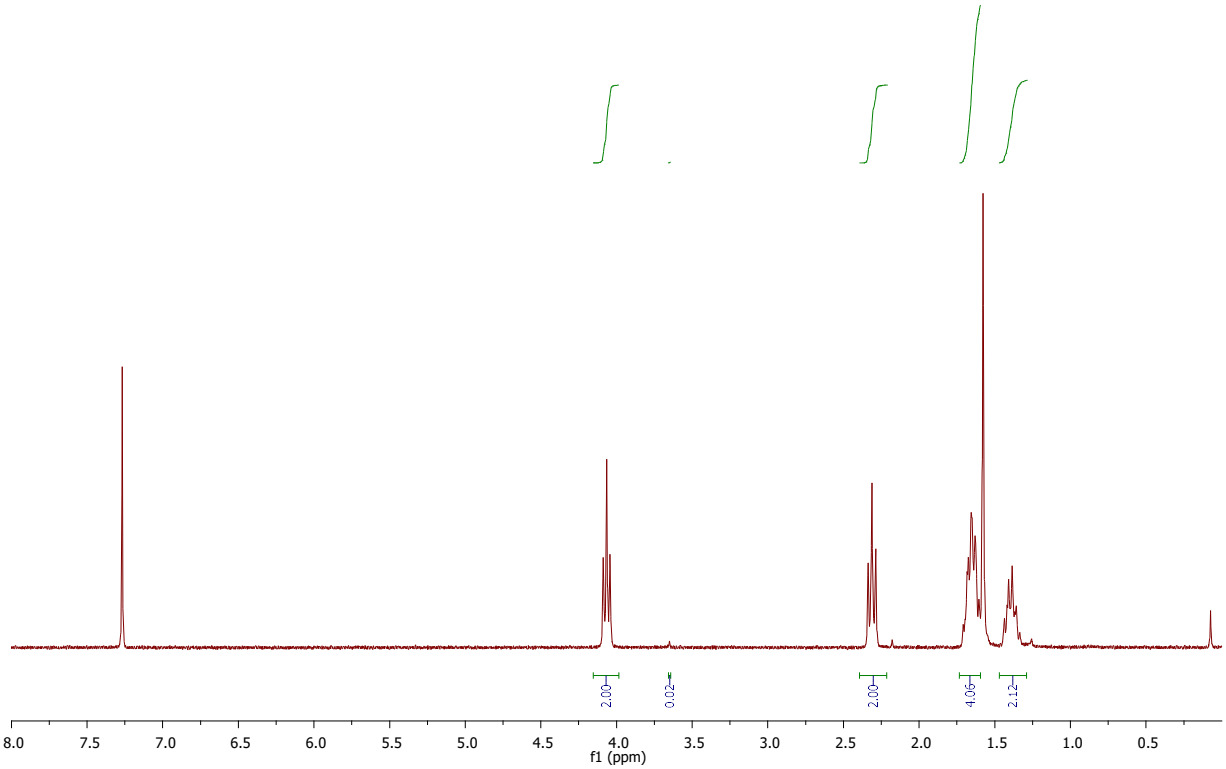

Figure 2.S1: NMR of washed PCL nanofiber. PCL: ^{1}H NMR (300 MHz, $CDCl_3$), δ(ppm): 4.06 (2H, t), 2.31 (2H, t), 1.66 (4H, quint), 1.38 (2H, quint). PEO: ^{1}H NMR (300 MHz, $CDCl_3$), δ(ppm): 3.65 (0.02H, s).

2.8.2 Porosity: Porosity was determined using a setup based on Archimedes' principle of buoyancy, where the masses (m) of mats were first collected. Mats were then submerged into water on a tared balance, while fixed to a glass pipette on one end to determine the mass of water displaced by the buoyant force. This displaced mass is equivalent to the volume (V_o) displaced due to the density of water being 1.0 g mL^{-1}. The density of the mats (ρ_{mat}) is then calculated from the mat mass and volume displaced (Equation 7). Porosity (ϕ) was then calculated by determining the density ratio of the mat as compared to a solid PCL film (ρ_{PCL} = 1.145 g cm^{-3}) and subtracting it from Equation 7 (Equation 8).

$$\boldsymbol{\rho_{mat} = \frac{m}{V_o}} \quad \textbf{(7)}$$

$$\boldsymbol{\phi = \left(1 - \frac{\rho_{mat}}{\rho_{PCL}}\right) X\ 100\ (8)}$$

2.8.3 Initiator Synthesis: 4-hydroxybenzophenone (1.0 g, 5.04 mmol) was dissolved in 15 mL tetrahydrofuran (THF) and cooled to 0 °C. Triethylamine (TEA) (0.51 g, 5.04 mmol) was added to the solution and allowed to stir for 10 minutes. α-bromoisobutyrylbromide (1.39 g, 6.03 mmol) was dissolved in 10 mL THF, then added to the reaction mixture by addition funnel over an approximate 10-minute period. The reaction was allowed to reach room temperature and stirred overnight. The TEA salt was filtered off and crude product was concentrated *in vacuo.* The crude product was then dissolved in dichloromethane (DCM) and washed three times with sodium bicarbonate and three times with water. The organic layer was dried over anhydrous sodium sulfate and concentrated *in vacuo*. The crude product was purified via column chromatography with a 3:1 ratio of hexane:ethyl acetate. Once isolated, the product was concentrated *in vacuo* to yield an off-white solid.[83] Yield: (1.2 g, 3.45 mmol, 68.4%). ^{1}H NMR (600 MHz, $CDCl_3$), δ(ppm): 7.90 (2H, d), 7.81 (2H, d), 7.61 (1H, t), 7.50 (2H, t), 7.28 (2H, d), 2.10 (6H, s) (Figure S-3).

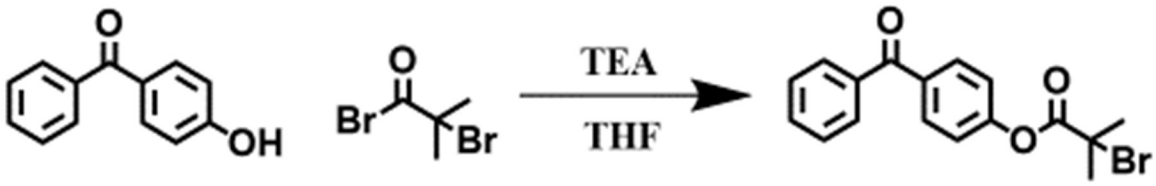

Figure 2.S2: Synthetic Scheme of benzophenone-ATRP initiator synthesis.

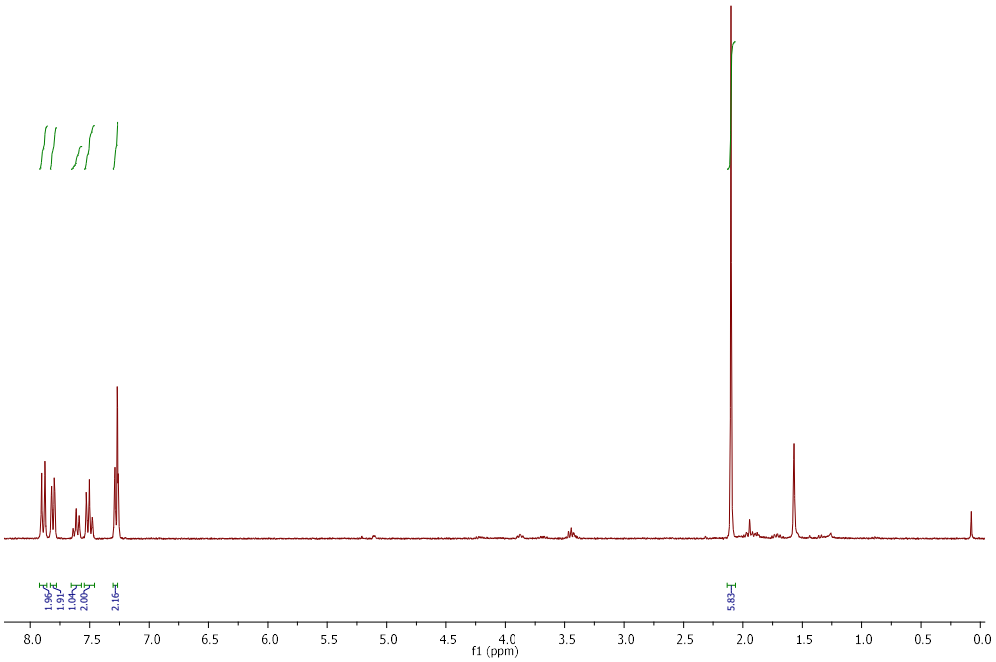

Figure 2.S3: NMR of benzophenone-ATRP initiator.

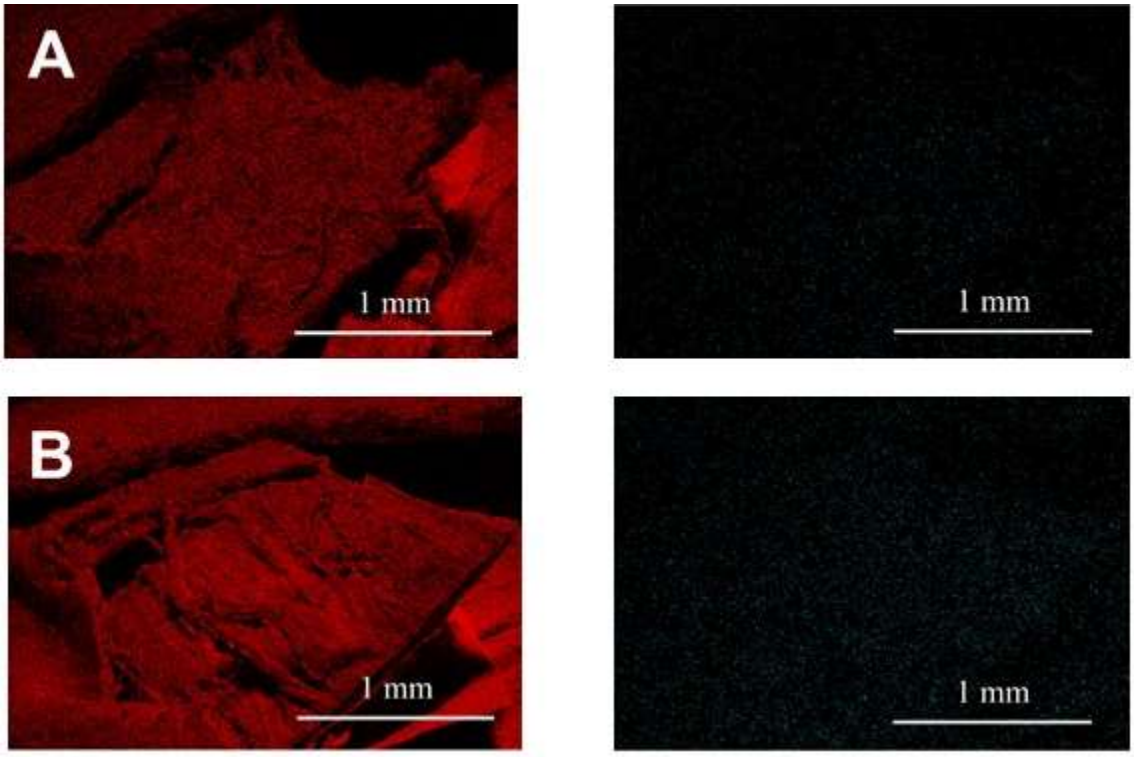

Figure 2.S4. Scanning electron microscopy micrograph overlaid with energy dispersive X-ray characterization with detecting copper(red, left) and bromine(blue, right). (A) PCL, (B) Initiator-functionalized PCL.

2.8.4 Synthesis of QA Monomer: 1-bromohexane (25.3 g, 0.064 mol) and DMAEMA (10.0 g, 0.153 mol) were added to a 50 mL of acetonitrile and 25 mL of chloroform at 40 °C and left overnight. Reaction mixture was then precipitated into cold ether and filtered. Product was washed with more ether, then dried under vacuum overnight to yield product as a white solid. Yield: (10.3 g 0.048 mol, 75%). 1H NMR (300 MHz, CDCl3): δ [ppm] 6.15 (s, 1H), 5.78 (s, 1H), 4.62 (t, 2H), 3.79−3.73 (m, 2H), 3.43−3.35 (m, 2H), 3.15 (s, 6H), 2.78 (s, 3H), 1.78 (quint, 2H), 1.32 (m, 6H), 0.86 (t, 3H).[52]

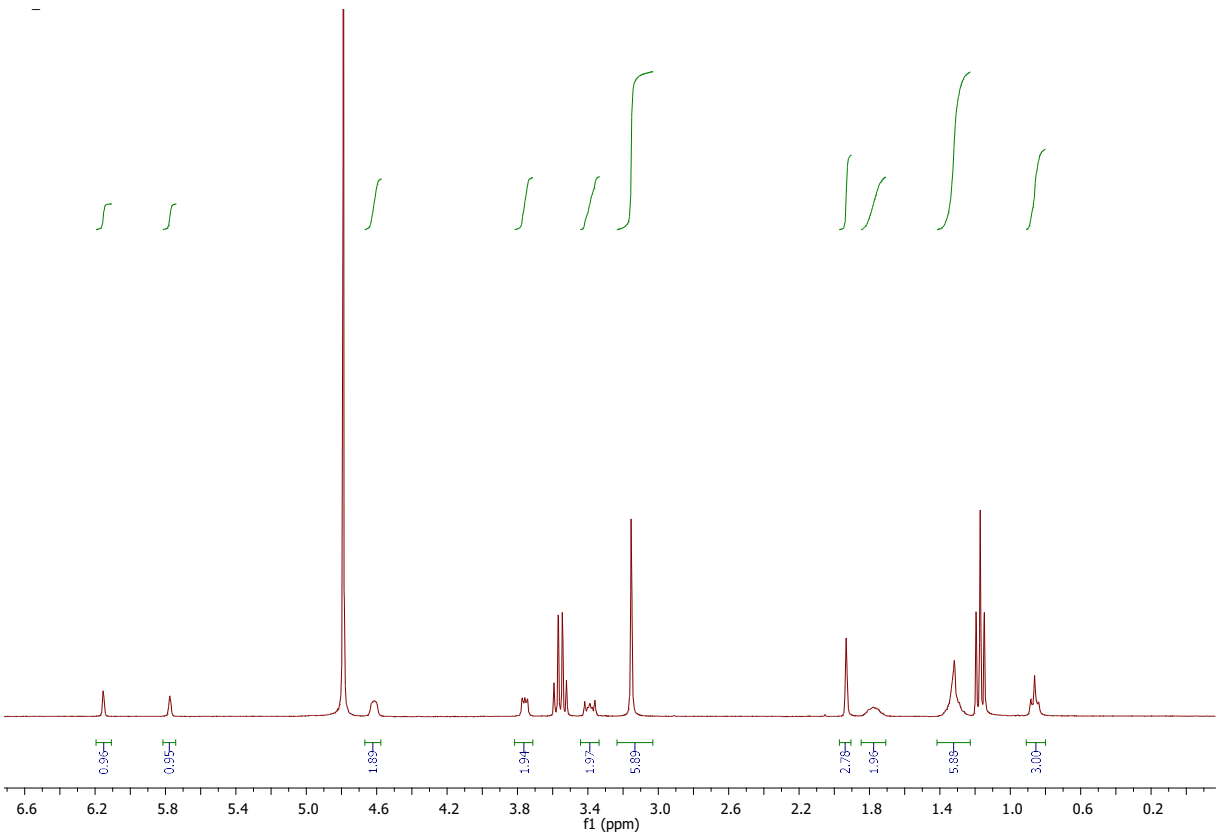

Figure 2.S5: NMR of QA monomer.

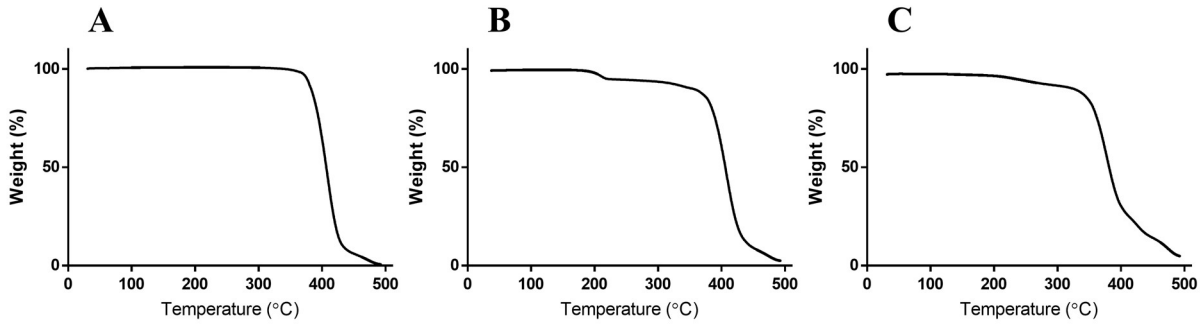

Figure 2.S6: Thermogravimetric analysis (TGA) plots of (A) unmodified PCL, (B) QA, and (C) M30 mats.

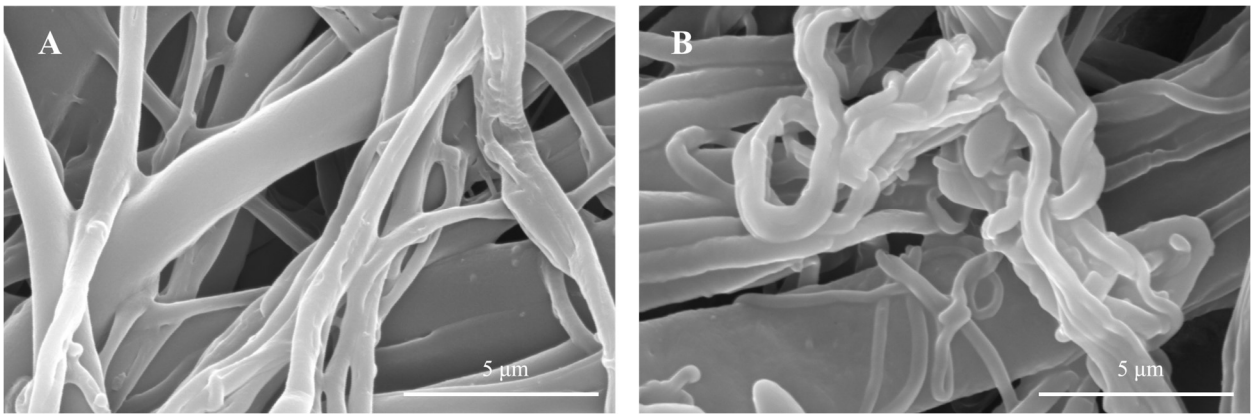

Figure 2.S7: Scanning electron micrographs of (A) QA and (B) M30 nanofiber mats. Scale bar indicates 5 µm.

2.8.5 Synthesis of Photolabile QA Polymers for *Grafting-to*: QA monomer (225 mg, 0.695 mmol), Me_6TREN (2.4 mg, 0.014 mmol), dimethylformamide (0.45 mL), and benzophenone initiator (QA-small: 4.8 mg, 0.014 mmol; QA-medium: 2.4 mg, 0.007 mmol, QA-large: 1.2 mg, 0.03 mmol) were added to a flame dried three-neck round bottom flask and purged with N_2. After 45 minutes, Cu(I)Br (1.0 mg, 0.007 mmol) was added under positive pressure. Polymerization was left overnight at room temperature. Polymers were dialyzed in deionized water for 2 days followed by lyophilization.

2.8.6 Synthesis of Photolabile M30 Polymers for *Grafting-to*: APMA (50 mg, 0.280 mmol), DMAPMPA (28.0 mg, 0.164 mmol), Me_6TREN (1.5 mg, 0.009 mmol), dimethylformamide (0.45 mL), and benzophenone initiator (M30-small: 3.1 mg, 0.009 mmol; M30-medium: 1.5 mg, 0.004 mmol, M30-large: 0.8 mg, 0.002 mmol) are added to a flame dried three-neck round bottom flask and purged with N_2. After 45 minutes, Cu(I)Br (0.6 mg, 0.004 mmol) is added under positive pressure. Polymerization was left overnight at room temperature. Polymers were dialyzed in deionized water for 2 days followed by lyophilization. Fibers were then vacuum dried in a desiccator.

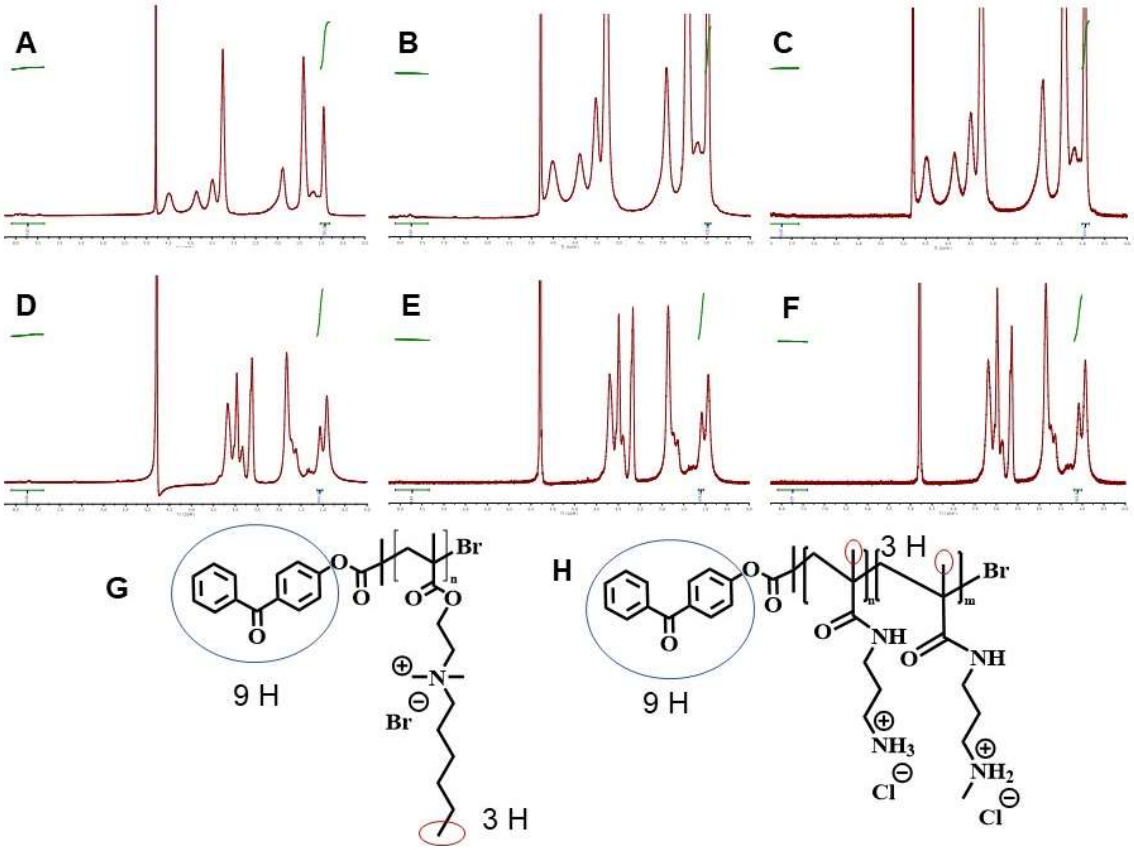

Figure 2.S8: (A-F) NMR's of QA and M30 Mn determination: (A) QA-Small, (B) QA-Medium, (C) QA-Large, (D) M30-Small. (E) M30-Medium, (F) M30-Large. (G) Structure of QA polymer showing hydrogen comparisons. (H) Structure of M30 polymer showing hydrogen comparisons.

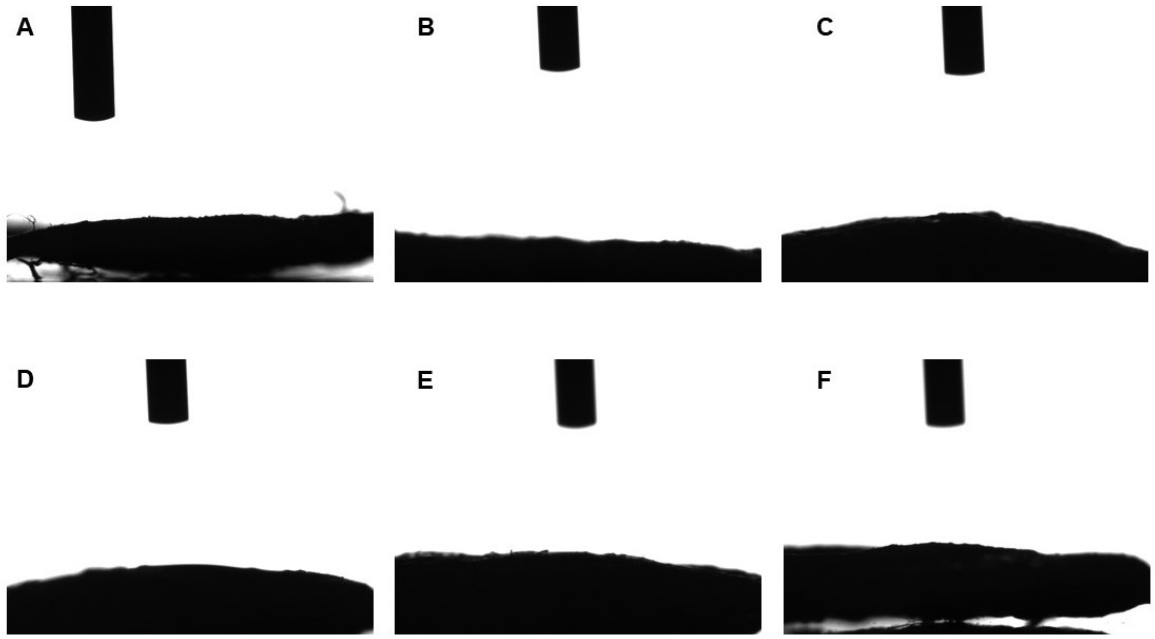

Figure 2.S9: Water contact angles of grafting-to fibers. (A) QA-Small, (B) QA-Medium, (C) QA-Large, (D) M30-Small, (E) M30-Medium, (F) M30-Large

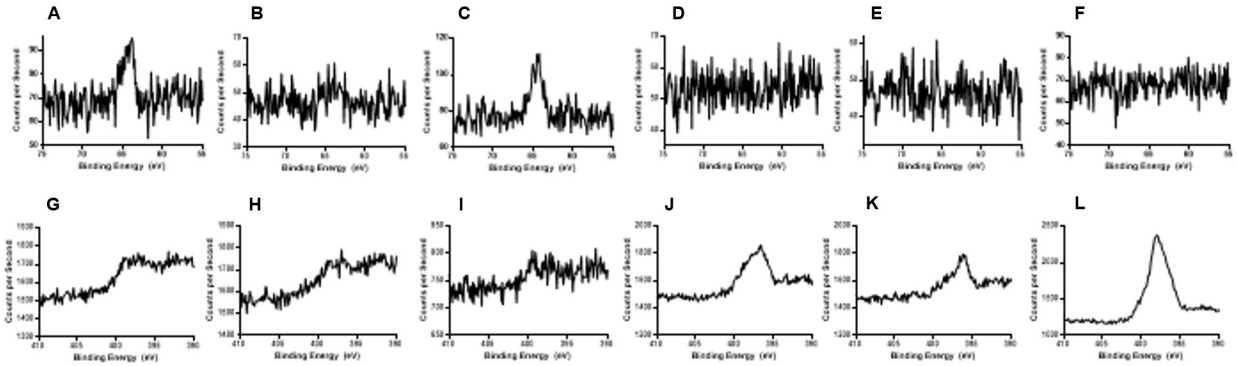

Figure 2.S10: High resolution XPS spectra of Br3d on (A) QA-Small, (B) QA-Medium, (C) QA-Large, (D) M30-Small, (E) M30-Medium, and (F) M30-Large. High resolution XPS spectra of N1s on (G) QA-Small, (H) QA-Medium, (I) QA-Large, (J) M30-Small, (K) M30-Medium, and (L) M30-Large nanofiber patches.

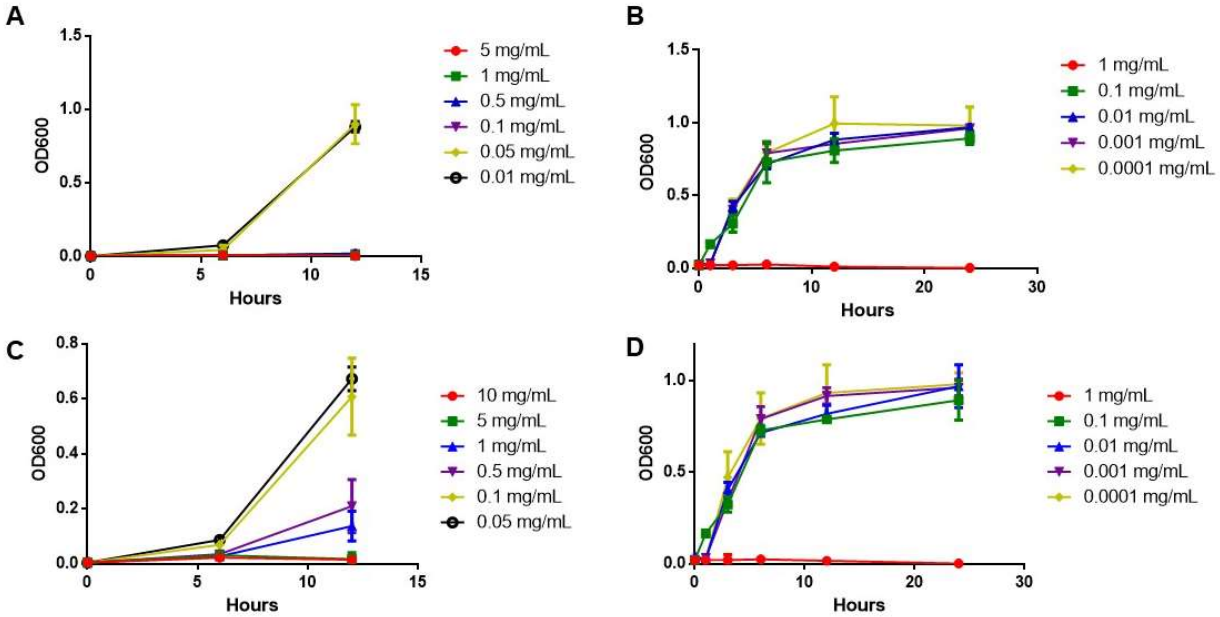

Figure 2.S11: Optical density measurements of bacteriawith antibacterial polymers at various concentrations. QA-medium and M30-Medium from Figure SI-3 were used. (A) QA with *E. coli*, (B) M30 with *E. coli*, (C) QA with *MRSA*, (D) M30 with *MRSA*.

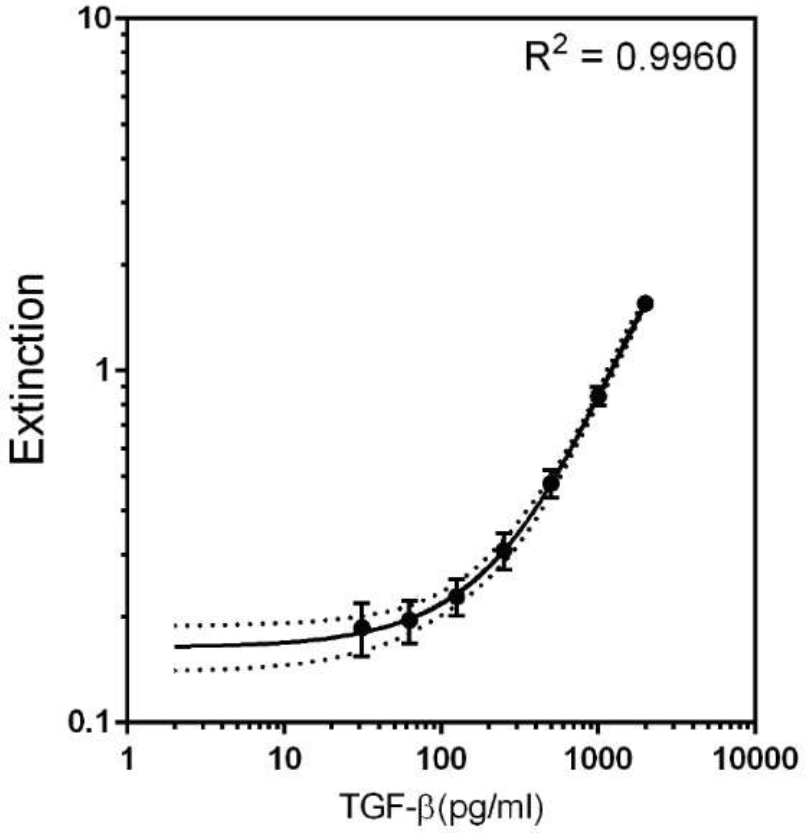

Figure 2.S12: Standard curve for detection of TGF-β1. The optical density of each standard (n=3) was determined using a microplate reader set to 450 nm wavelength. Data was fit using a four parameter logistic (4-PL) equation (R^2 = 0.9960).

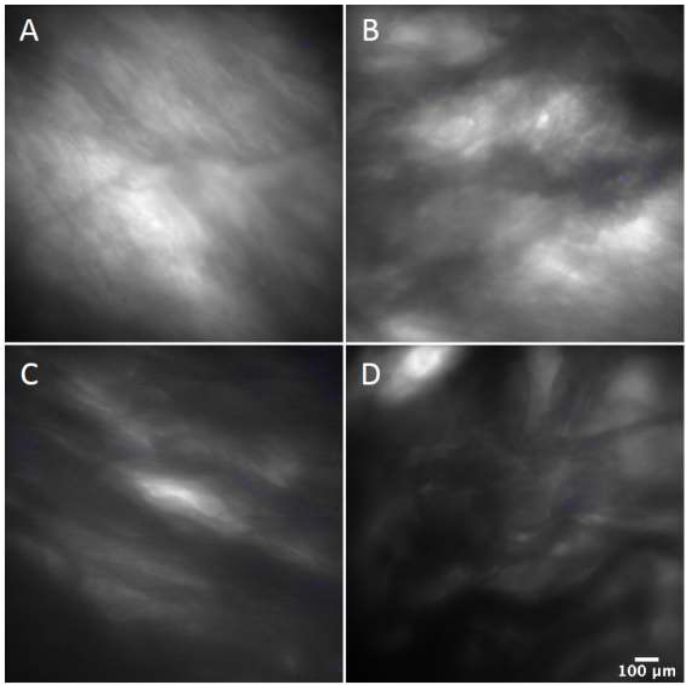

Figure 2.S13: Confocal laser scanning microscopy pictures of (A) PCL, (B) PEGMEA, (C) M30 and (D) QA antibacterial mats. No DAPI signals were detected among the mats confirming the efficacy of the trypsinization treatment.

CHAPTER 3: Surface-Modified Melt Coextruded Nanofibers Enhance Blood Clotting in Vitro

3.1 Abstract: Blood loss causes an estimated 1.9 million deaths per year globally, making new methods to stop bleeding and promote clot formation immediately following injury paramount. The fabrication of functional hemostatic materials has the potential to save countless lives by limiting bleeding and promoting clot formation following an injury. This manuscript describes the melt manufacturing of poly(ε-caprolactone) nanofibers and their chemical functionalization to produce highly scalable materials with enhanced blood clotting properties. The nanofibers are manufactured using a high throughput melt coextrusion method. Once isolated, the nanofibers are functionalized with polymers that promote blood clotting through surface-initiated atom transfer radical polymerization. The functional nanofibers described herein speed up the coagulation cascade and produce more robust blood clots, allowing for the potential use of these functional nonwoven mats as advanced bandages.

Keywords: Nanofibers, Melt Coextrusion, Photochemistry, SI-ATRP, Blood Clotting, Coagulation, Fibrin

3.2 Introduction: Functional polymeric nanofibers have attracted significant attention in recent years due to their vast applications in biomedicine. Some of these applications include drug delivery (where fibrous materials can provide low diffusion distances), tissue engineering (where the high surface area to volume ratio leads to high porosity and ample sites for cellular adhesion), and wound intervention (where altering the surface characteristics of nanofibers can lead to excellent antibacterial effectiveness without compromising biocompatibility).[1–6] The need for improving human health has been instrumental in leading advances in polymer processing

technology and surface modification chemistries, which have helped usher in a new generation of functional biomaterials.

The literature describes a multitude of nanofiber fabrication methods, each with associated advantages and challenges. The most common method for fiber fabrication is electrospinning due to its simple and inexpensive setup, and the ability to control the dimensions of the fabricated fibers down to the nanoscale.[4,7] Electrospinning is useful in a variety of research applications, however the quality and size of fibers produced is highly dependent on the processing parameters of the system.[8,9] Additionally, electrospinning has a low maximum throughput, 200 g h^{-1}, which may limit the commercial translation of this method.[10] Researchers have since developed new nanofiber manufacturing techniques, but these also present limitations: fibers made via rotary jet spinning exhibit weak mechanical properties,[12,13] melt blowing is a challenging method to produce fibers with dimensions in the nanoscale,[14] and melt electrospinning requires high voltages while providing a throughput that is lower than traditional electrospinning.[11] To combat these issues, melt coextrusion has recently emerged as a nanofiber fabrication method that is scalable, solvent-free, and yields nanoscale fibers.[15] Melt coextrusion provides the ability to create fibers with easily tunable cross-sectional dimensions and mechanical properties. The manufacturing process is solvent-free and continuous, producing material at a rate of 2 kg/hr, significantly outperforming comparable electrospinning methods.[15–17] Recent work has utilized these materials for various applications including for use as fuel filters,[18] biomedical scaffolds,[17,19] and as antibacterial materials to name a few.[5]

Fibers fabricated via melt coextrusion can be produced from most extrudable thermoplastic polymers, but have certain requirements when used in the biomedical arena.[4,20] First and foremost: nanofibers intended for biomedical applications must be biocompatible. Other advantageous

characteristics include having favorable degradation kinetics, mechanical properties, and the ability to introduce chemical or biochemical modifications.[4] Effective biomaterial scaffolds cannot be cytotoxic nor should they induce or suppress the immune system in an undesirable manner.[21] A common class of materials used in biomedical applications are polyesters as they are well established to be non-cytotoxic and have a long history of use in FDA-approved devices.[22] Commonly utilized polyesters include poly(lactic acid) (PLA), poly(glycolic acid) (PGA), and poly(ε-caprolactone) (PCL). PCL in particular is known for its flexibility (reaching more than 700% elongation at break)[16] and its slow hydrolytic degradation rate (2-3 years).[23,24]

Unmodified polyester nanofibers do not possess functional biologically active properties that would improve their utility in most biomedical applications, such as tissue engineering or wound treatment.[5,25] Properties that may improve biomedical outcomes can be enhanced by introducing bio-active moieties onto the surface of the nanofiber. There are many potential functionalization methods of polyesters including end group modification,[26] hydrolysis,[28] aminolysis,[27] and photochemical covalent modification.[29] Chemical modification of nanofiber scaffolds has allowed for the fabrication of antifouling[30] and antibacterial mats,[5] as well as the creation of platforms for cellular adhesion, growth, proliferation, and differentiation mimicking the extracellular matrix (ECM).[7,17,20]

Functional nanofibers offer unique solutions for wound treatment due to their high porosity and large surface area. Their use as hemostatic materials provides a simple solution to hemorrhagic trauma. Hemorrhagic shock is a condition of extreme blood loss which leads to inadequate oxygen delivery to organs and tissues. Each year, 60,000 deaths in the United States and 1.9 million deaths worldwide occur from hemorrhaging.[56,57] Following any vascular injury resulting in escaping blood, the body's aim is to prevent further blood loss by "plugging the hole." This is done via the

gelation of blood by activating a thrombin-mediated coagulation cascade. Through a series of enzyme-mediated reactions, a fibrin mesh is formed at the site of injury, resulting in a stable clot.[58–64] There are two main mechanisms that induce the coagulation cascade, first is the extrinsic or tissue factor (TF) pathway, which occurs in traditional hemostasis when cells that are expressing a tissue factor protein encounter blood plasma, triggering the clotting cascade. The second method of initiating the coagulation cascade is via the intrinsic or contact pathway. The contact pathway occurs when plasma encounters specific types of artificial surfaces such as diatomaceous earth, glass, or clay amongst others. Blood contact with one of these surfaces causes a plasma protein, factor XII, to change conformation, thus activating the coagulation cascade. This pathway does not contribute to natural hemostasis, but does participate in thrombotic diseases.[65,66]

Utilizing the contact pathway unlocks the potential to modify the surface of a material to trigger a desired clotting event. Sperling and colleagues studied the effects of varying hydrophobicity and its impact on blood clotting. Experiments with varying ratios of alkyl ($–CH_3$) and carboxylic acid (–COOH) groups on glass surfaces were tested and it was concluded that neither solely alkyl nor carboxylic acid were the ideal surface to promote blood clotting. Alkyl surfaces displayed the largest numbers of adherent platelets, while carboxylic acid surfaces had the greatest contact activation. However, neither showed superior clotting abilities when compared with a surface comprised of both functional groups. Superior clotting required a balancing act between contact activation and platelet adhesion, and that balance had a strong synergistic effect on the successfulness and degree of blood clotting.[84] Further studies have expanded on this, varying the length of alkyl chains present, showing that the most effective surface coating was a random co-polymer with a ratio of 65% acrylic acid (AA) to 35% butyl methacrylate (BMA).[85]

This manuscript describes the fabrication of functional nanofiber mats that improve blood clotting to quickly form more robust clots. Current hemostatic wound treatment devices typically feature either an artificially formed blood clot[86] or materials made specifically of a hemostatic agent such as chitosan.[87] Therefore, the materials are limited in the properties that can be bestowed on the devices. Creating functional nanofiber mats allows for the use of a wide variety of materials with varying properties, as well as the ability to incorporate other relevant functionalities. Melt-extruded nanofibers are ideal hemostatic surfaces due to their ability to be fabricated at large scale and their intrinsic high surface area which would put even large wounds in contact with high surface functionality for contact-based hemostasis. We anticipate that this would be preferrable to the tissue factor mediated coagulation scheme due to high costs associated with producing large amounts of clotting factors, difficulty in long-term storage at sites that would be in need of large scale wound dressings (e.g. the military arena), and challenges in integrating tissue factors into materials.[84,85,88] We describe the fabrication of melt coextruded PCL nanofiber mats and their subsequent functionalization utilizing a *grafting-from* surface-initiated atom transfer radical polymerization (SI-ATRP), due to its high grafting efficiency and ease of fiber modification. The surfaces are modified to control their hydrophobic/hydrophilic balances, leading to an enhancement of the rate and robustness of blood clotting.[85]

3.3 Materials and Methods

3.3.1 Materials: CAPA 6800 PCL-80 kDa was purchased from The Perstorp Group. POLYOX N80-200 kDa and POLYOX N10-100 kDa poly(ethylene oxide) (PEO) were purchased from Dow Chemical. Triethylamine (TEA) was purchased from VWR Life Science. Tris(2-dimethylaminoethyl)amine (Me_6TREN) and 1-bromohexane were purchased from Alfa Aesar. Copper (I) bromide, α-bromoisobutyryl bromide, acrylic acid, calcium chloride, butyl

methacrylate, HEPES, 25% glutaraldehyde solution in H_2O, L-A-phosphatidylcholine type XVI-E, L-A-phosphatidylserine, and bovine serum albumin (BSA) were purchased from MilliporeSigma. Sodium chloride, dimethylsulfoxide (DMSO), sodium phosphate monobasic monohydrate, and sodium phosphate dibasic heptahydrate were purchased from Fisher Chemical. Platelet poor plasma was purchased from Technoclone. Phosphate buffered saline (PBS) pH 7.4 1X was purchased from Gibco. Recombinant tissue factor (rTF) was purchased from BioLegend. Human α-thrombin was purchased from Haematologic Technologies. Ethyl alcohol, anhydrous was purchased from Electron Microscopy Sciences.

3.3.2 Instrumentation and Equipment: A Haake Rheodrive 5000 twin-screw extruder was used to compound PEO. A custom, two-component melt coextrusion system with a series of vertical and horizontal multipliers was used to fabricate composite tapes. Nanofibers were subjected to a SereneLife SLPRWAS26 Compact Pressure Washer (maximum pressure 1500 psi, 3 mm length by 11 mm width) to remove excess PEO and entangle nanofibers into mats. An Anytime Tools sharp 1/4″ hollow punch was used to stamp nonwoven nanofiber mats into a circular shape. An Omnicure Model S1500 standard filter 320−500 nm UV light source system was used for photochemistry. A FEI Apreo LoVac FESEM was used to obtain electron micrographs. A ramé hart Model 200 goniometer was used to obtain water contact angle measurements. A Kratos Analytical AXIS Supra surface analysis instrument was used for X-ray photoelectron spectroscopy data. A Tecan Infinite M PLEX Monochromator was used to obtain fluorescence data. A Tousimis Autosamdri-815, Series A Automatic Critical Point Drier was used to dry prepared blood clots.

3.3.3 Methods

3.3.3.1 Melt Coextrusion of Compound Tapes: 200 kDa and 100 kDa PEO were first mixed

in a 30%/70% w/w% ratio (to achieve a rheological match to PCL at extrusion temperatures)[16] and dried for 48 hours at 40 °C. The PEO was then compounded in a twin-screw extruder at 140 °C followed by pelletization.[20] PCL and the compounded PEO pellets were then dried for 48 hours at 40 °C before being coextruded at 180 °C to provide PCL nanofibers embedded in a PEO matrix. The extrusion line was comprised of 16 vertical and 4 horizontal multipliers. Between the horizontal and vertical multipliers, the extrudate was encased in a 33% by volume PEO skin layer. Completed compound tapes exited the system through a 3" tape die and were collected on a chill roll at room temperature that rotated at 15 rpm.[30]

3.3.3.2 Removal of PEO and Preparation of PCL Mats: Composite tapes were secured inside of a beaker of stirring water for 6 hours with the water being changed hourly. The tapes were then left overnight in a 70% MeOH: 30% H_2O solution to remove the PEO, revealing PCL fibers. Fibers were then attached to a fiberglass plate in a single layer and covered with a wire mesh to be washed with a pressure washer, varying the spray size. This high-pressure wash serves two purposes: (1) to remove any remaining PEO and (2) to entangle the nanofibers to form nonwoven mats. Nonwoven mats were then dried in a desiccator overnight and 6 mm circular patches were punched out of them with a hollow punching apparatus to be used for further preparation and experimentation.

3.3.3.3 Nanofiber Functionalization with Photochemistry: Nonwoven mats (6 mm diameter, ~4.5 mg) were placed into a 10 mg/mL solution of a benzophenone-ATRP initiator in MeOH, whose synthesis was previously described.[5] Saturated nonwoven mats are placed in a vacuum desiccator and dried overnight, then subjected to a broadband UV lamp (320 – 500 nm) with an intensity of 548 mW/cm^2 for 35 minutes per side. The mats were then washed three times with

methanol and dried again overnight in a vacuum desiccator. Successful functionalization was confirmed with X-ray photoelectron spectroscopy (XPS) and water contact angle (WCA).

3.3.3.4 *Grafting-from* ATRP: Monomer (2.13 mmol) (e.g. blood clotting copolymer utilizes 65 mol% acrylic acid and 35 mol% butyl methacrylate), Me_6TREN (7.4 mg, 0.043 mmol), dimethylformamide (2 mL), and 21 initiator-modified nonwoven mats were added to a three-neck round bottom flash and bubbled with N_2 gas for 50 minutes. Cu(I)Br (3.1 mg, 0.021 mmol) was then added quickly under positive N_2 pressure. The polymerization was left overnight at room temperature. The following morning, mats were removed and washed three times with MeOH then dried in a vacuum desiccator. Successful functionalization was confirmed with XPS and WCA.

3.3.3.5 Plasma Recalcification Time: Nanofiber mats (6 mm diameter circles) were placed in individual wells of a tissue culture treated 96 well plate that was first warmed in a 37 °C incubator for 5 minutes. 100 µL of 0.025 M $CaCl_2$ and 100 µL of reconstituted platelet-poor plasma (PPP) were added to the wells, quickly mixed with a micropipette, then placed in a 37 °C hot water bath for the duration of the experiment. Gelation was determined when the plasma solution became visibly cloudy and stiff. Triplicate data points were obtained; however, each sample was incubated individually to allow accurate observations and measurements. [88]

3.3.3.6 Thrombin Generation Assay: Sample nonwoven mats were placed in the wells of a black, flat-bottom 96 well plate (5 replicates per sample). 1 µL of a 1 mM fluorogenic substrate [1 mM Z-Gly-Gly-Arg-AMC.HCL, 15 mM $CaCl_2$ in HNa buffer (25 mM HEPES and 175 mM NaCl at pH 7.35), containing 2% by volume DMSO and 0.4% by volume BSA] with 15 mM $CaCl_2$, 20 µL phospholipid/tissue factor mixture [3.2 µM 80%/20% by mol phosphatidylcholine/phosphatidylserine with 17.9 pM rTF in HNa buffer], and 80 µL of PPP were added to the wells, mixed, and immediately placed into a plate-reader; measuring the fluorescence

every minute for 45 minutes. A standard curve was generated by replacing the PPP with various thrombin dilutions without the presence of the sample mats. Maximum thrombin concentrations were calculated by comparing the slopes generated from the TGA to the standard curves. [89]

3.3.3.7 Fibrin Clot Architecture Analysis: Clots were prepared as described in section **2.3.5**, but were left for 2 hours to allow the coagulation process to complete. Clots were washed for 30 minutes three times with PBS (pH 7.4). Clots were fixed with glutaraldehyde in a phosphate buffer prepared with 68.4% by volume of 1M Na_2HPO_4 and 31.6% by volume of 0.1 M NaH_2PO_4, combined and diluted to give a 2% glutaraldehyde solution in 0.1 M of the combined phosphate buffer. The clots were dehydrated in absolute ethanol of varying grades (50%, 75%, 100%) for 1 hour each, then dried in a CO_2 critical point drier. Following drying, the clots were submerged in liquid nitrogen and broken in half using a pair of tweezers. The prepared clots were sputter coated with gold and imaged via scanning electron microscopy (SEM) at various points including the clot/nanofiber interface, a top view of the clots, and the clot cross-section. [85]

3.3.3.8 Statistical Analysis: Reported results are the mean with standard deviation. Unpaired t-tests were performed on plasma recalcification time, maximum thrombin concentration, and fibrin dimension analysis data. Results were considered significant if $p < 0.05$.

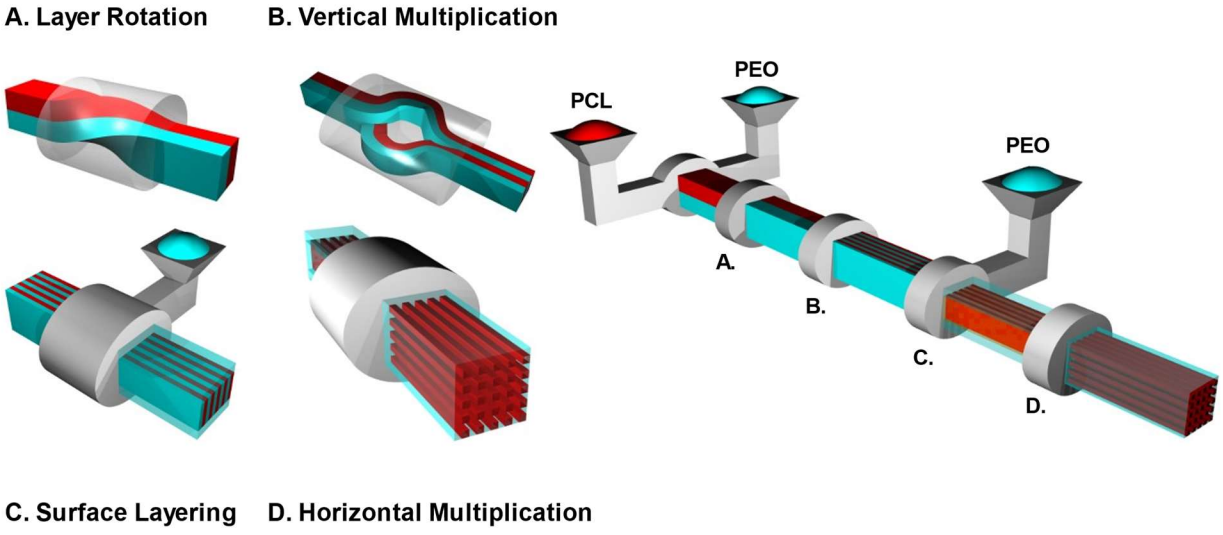

Figure 3.1: Schematic diagram of melt coextrusion utilizing (A) layer rotation, (B) vertical multiplication, (C) surface layering, and (D) horizontal multiplication procedures.

3.4 Results and Discussion

3.4.1 Fabrication of Melt Coextruded Nanofiber Mats: PCL nanofibers were prepared via a melt coextrusion process, as previously described. PEO was used as an coextrudate due to its immiscibility with PCL leading to well defined layer separation and easy delamination through aqueous dissolution.[5] Melt coextrusion proceeded by individually pumping PEO and PCL into the extrusion line, where each polymer was stacked on top of one another. A 90° rotation immediately followed this process wherein the two melt flows were oriented side by side (**Figure 3.1A**). The melt was then sent through a "n" number of vertical multipliers (n = 16), where each multiplier doubled the amount of vertical layers. This series of multiplication steps created 2^{n+1} vertical layers (**Figure 3.1B**). A 33% by volume PEO skin layer was then pumped on top and bottom of the melt flow (**Figure 3.1C**). Finally, the melt was passed through a series of "m" number of horizontal multipliers, establishing 2^m (m = 4) horizontal layers and 2^{n-m} vertical layers (**Figure 3.1D**), resulting in 4096 x 116 PCL domains embedded in a PEO matrix.

The resulting extrudate is a composite material with PCL fibers embedded within a sacrifical PEO matrix. PCL nanofiber scaffolds were obtained by removal of the hydrophillic PEO matrix. The composite tapes were washed in an agitated water bath to remove the bulk of the PEO phase. Following the initial washing, the water is replaced with a 70% MeOH bath and left overnight to remove the majority of the PEO. Finally, the nanofibers are treated with a high-pressure water jet to (1) entangle the nanofibers to create non-woven mats and to (2) remove any remaining PEO which is difficult to completely remove with just a water/MeOH bath. This process removes 97% of the PEO from the nanofibers (**Figure 3.S1**).[5] Circular segments were punched out of the resulting nanofiber sheets (6 mm) to facilitate well-plate assays.

3.4.2 Nanofiber Functionalization with Photochemistry and SI-ATRP: Grafting functional polymers off of the nanofiber surface first required the covalent conjugation of an atom transfer

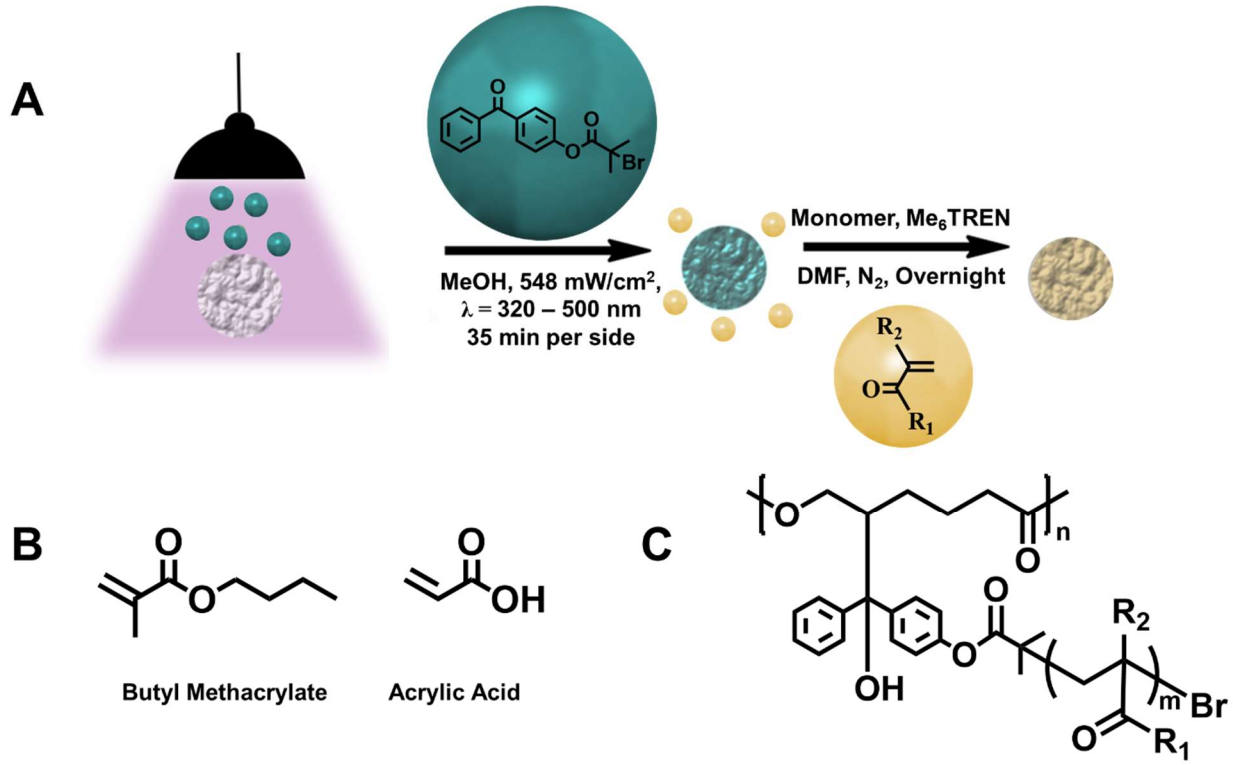

Figure 3.2: (A) Schematic diagram of SI-ATRP nanofiber mat functionalization. Mats are dip-coated with initiator, dried, and exposed to UV light. This is followed by standard ATRP conditions. (B) Chemical structure of monomers used in nanofiber mat functionalization. (C) Chemical structure of functionalized nanofibers.

radical polymerization (ATRP) initiator onto the fiber.[5] A benzophenone modified with a tertiary bromide was first synthesized to act as an ATRP initiator. This molecule is known to undergo photochemical hydrogen abstraction, followed by radical insertion into the PCL backbone, yielding a tertiary bromide functionalized nanofiber surface.[29,69] Nanofiber mats were dip-coated in a solution containing the benzophenone-ATRP initiator and allowed to dry to create a coating on the surface. Dried and coated mats were subsequently exposed to UV light to initiate the photochemical transformation, yielding bromide functionalized mats ready to undergo SI-ATRP.

Surface-initiated ATRP (SI-ATRP) was conducted from the modified nanofiber surface to alter the hydrophobic/hydrophilic balance (**Figure 3.2A**). Studies comparing the roles of carboxylic acid and alkyl functionalities have shown that differing ratios of the two have a significant impact on the formation and quality of blood clots. The ideal composition was a statistical copolymer of 65% acrylic acid (AA) and 35% butyl methacrylate (BMA) (**Figure 3.2B**), which significantly improved the rate and quality of fibrin blood clots as compared with other

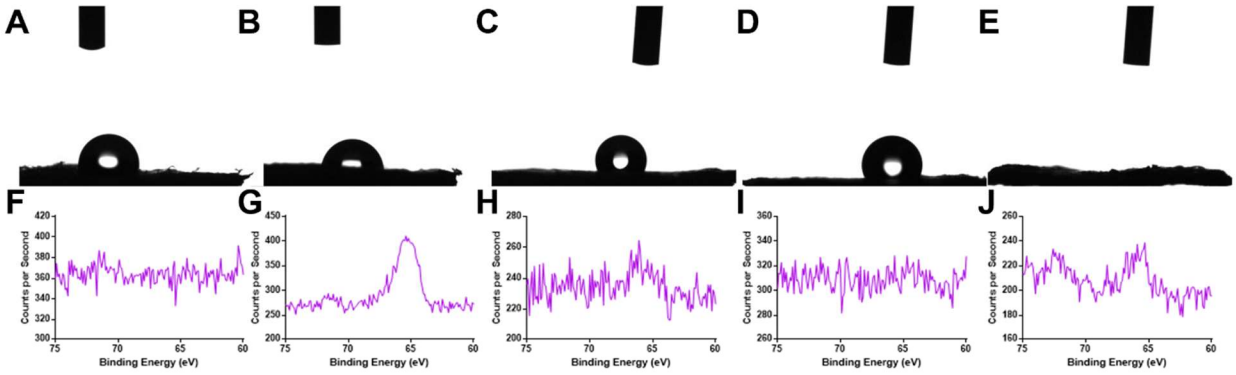

K

Fiber Sample	Percent Composition			Water Contact Angle
	C	O	Br	
Unmodified PCL	81.14	18.86	0.00	92.6 ± 9.7°
Initiator	81.70	18.20	0.09	82.8 ± 4.3°
BCCP	79.44	20.54	0.02	115.8 ± 2.3°
Butyl Methacrylate	84.08	15.88	0.04	124.3 ± 3.7°
Acrylic Acid	72.14	27.80	0.05	0°

Figure 3.3: Surface characterization of functionalized nanofiber mats. WCA measurements of (A) PCL, (B) initiator, (C) BCCP, (D) butyl methacrylate, and (E) acrylic acid functionalized nanofiber mats. High-resolution XPS spectra of Br3d on (F) PCL, (G) initiator, (H) BCCP, (I) butyl methacrylate, and (J) acrylic acid functionalized nanofiber mats.

variations and controls.[85] We compared this composition with surfaces functionalized with acrylic acid, butyl methacrylate, and unmodified PCL (**Figure 3.2C**). Functionalization was first confirmed with WCA, which is used to show differences in the surface energy of a material, allowing for the determination of chemically distinct surfaces. As the hydrophilicity of a material's surface increases, the contact angle approaches 0°; and as hydrophobicity increases the value of the contact angle trends oppositely. In general, a WCA greater than 90° is considered hydrophobic and less than 90° is considered hydrophilic.[90] Upon functionalization of the PCL fibers with the ATRP initiator, the WCA decreases slightly from 92.6 ± 9.7° (**Figure 3.3A**) to 82.8 ± 4.3° (**Figure 3.3B**), indicating the ATRP initiator may make the sample more hydrophilic. The water contact angle of the blood clotting copolymer (BCCP), increased to 115.8 ± 2.3° (**Figure 3.3C**) indicating the hydrophobic effects of the exposed hydrocarbon tail of BMA dominate the surface energy relative to the hydrophilic effects of the carboxylic acid from AA. Our control fiber mats used either a BMA homopolymer displaying a WCA of 124.3 ± 3.7° (**Figure 3.3D**), or an AA homopolymer showing a WCA of 0° (**Figure 3.3E**), indicating complete wetting.

XPS was used to further characterize the modified fiber mats by providing information about the chemical composition of the nanofiber surface. Quantifiable variations in atomic surface composition confirm the successful functionalization of the material. High-resolution spectra show the successful incorporation of bromine in the initiator and polymer functionalized nanofibers, due to the presence of bromine in the benzophenone ATRP initiator and end groups of the respective polymers (**Figure 3.3F-J**). Survey spectra confirm the lack of any unanticipated elements present in the samples (**Figure 3.S2A-E**). **Figure 3.3K** summarizes the quantitative data from the WCA and XPS plots and shows that incorporating solely butyl methacrylate increases the carbon:oxygen ratio while incorporating only acrylic acid significantly decreases the carbon:oxygen ratio. The

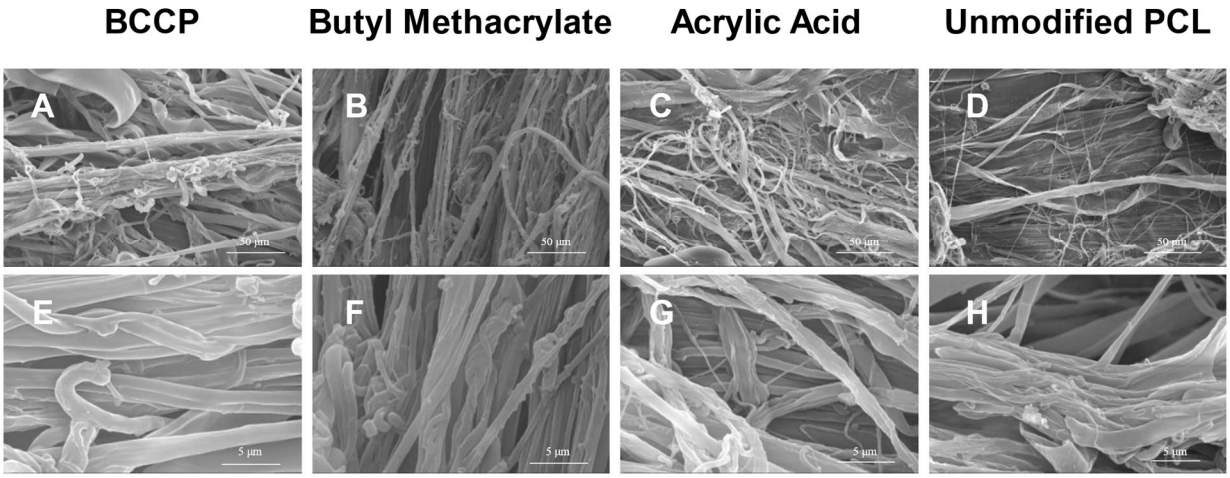

Figure 3.4: Scanning electron micrograph of nanofiber mats of BCCP (A,E), butyl methacrylate (B,F), acrylic acid (C,G), and unmodified PCL (D,H) nanofiber mats. Scale bars indicate 50 µm (A,B,C,D) and 5 µm (E,F,G,H).

ratio of BCCP-modified surfaces is between the carbon:oxygen ratios of the BMA and AA modified mats and verifies the copolymerization of both monomers and approximates that anticipated 65/35% ratio. Analysis of the XPS results utilizing peak integration reveals a composition of 61.0 ± 0.02% acrylic acid and 39.0 ± 0.02% butyl methacrylate, close to the desired ratio of 65%/35%. Scanning electron micrographs confirm that the functionalization does not have any meaningful impact on nanofiber morphology when comparing the functionalized nanofibers (**Figure 3.4A-C, E-G**) with unmodified PCL (**Figure 3.4D, H**).

3.4.3 In Vitro Blood Clotting Experiments:

3.4.3.1 Plasma Recalcification Time: Plasma recalcification time (PRT) is a qualitative study determining the length of time it takes a clot to form. Ca^{2+} ions have been known since the late 1800s to be an essential part of the blood coagulation cascade,[91] and is commonly inactivated with anticoagulants such as sodium citrate to stabilize and preserve blood and blood products.[92] PRT studies reintroduce a calcium source, and measure the time until a gel forms, indicating the formation of a fibrin clot (**Figure 3.5A-B**). Citrated plasma was incubated with $CaCl_2$ and nanofiber mats. The time was recorded once the plasma solution became cloudy and would adhere

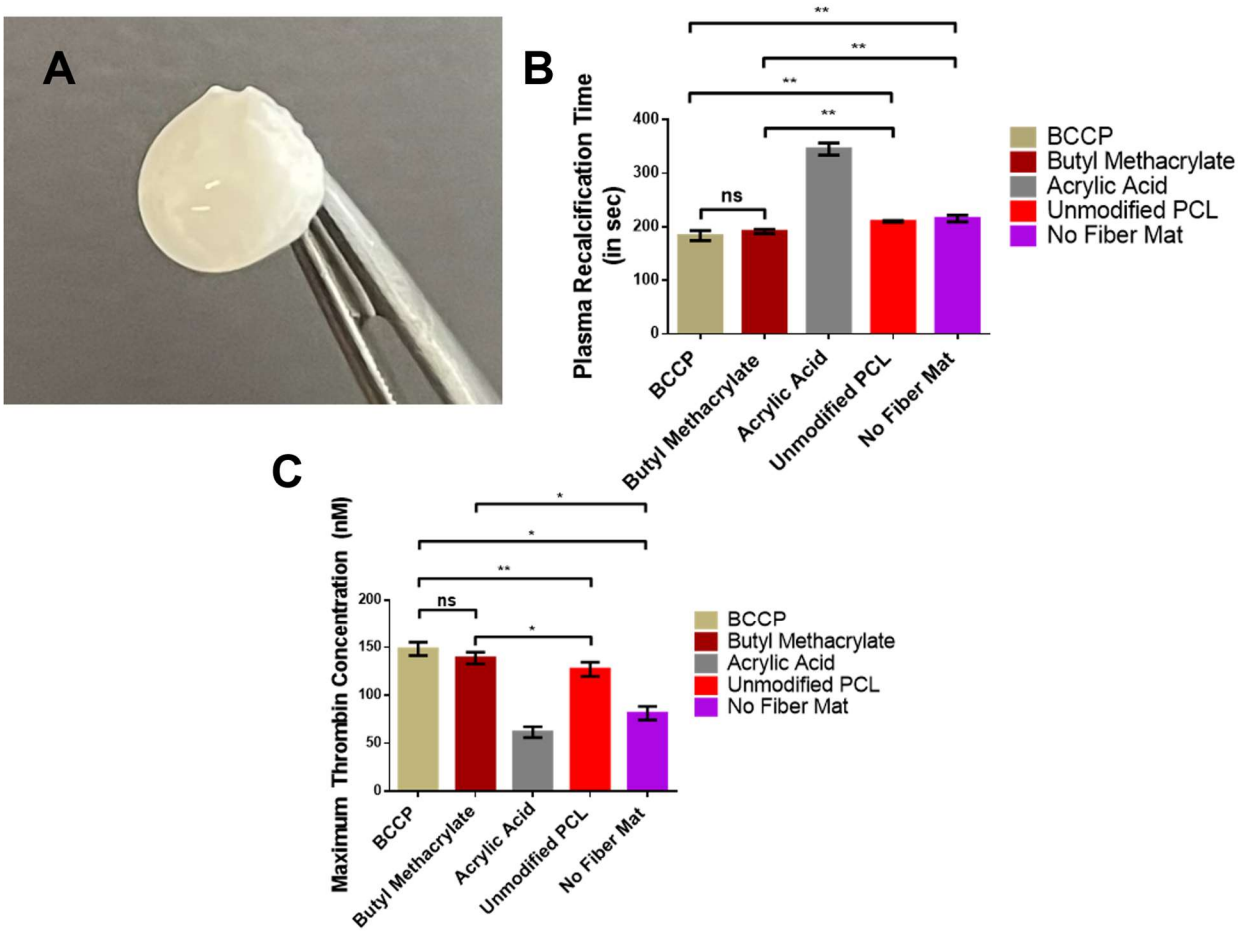

Figure 3.5: Blood clotting studies. (A) Macroscale image of clot covered nanofiber mat. (B) Plasma recalcification time and (C) maximum thrombin concentrations from thrombin generation assay plots of the various clots. *p ≤ 0.05 and **p ≤ 0.01.

to the mat indicating the transformation from a liquid to a solidified gel. Control samples included clots formed in well plates without a fiber mat and clots formed on unmodified PCL mats, which displayed similar PRTs of 215.5 ± 6.4 and 210.0 ± 1.4 seconds, respectively. BCCP and BMA modified fiber mats significantly decreased the PRT with values of 183.5 ± 9.2 and 191.4 ± 4.2 seconds, respectively, indicating both materials accelerated the blood clotting process. AA modified mats significantly increased the amount of time it took for plasma recalcification to 345.1 ± 11.3 seconds, indicating anticoagulation properties in mats modified with just acrylic acid.

3.4.3.2 Thrombin Generation Assay: A key step of the blood coagulation cascade and the formation of a blood clot is the thrombin-mediated conversion of fibrinogen to fibrin. Thrombin

concentrations are directly correlated with the strength and stability of fibrin fibers, with high concentrations producing thicker, more dense networks of highly branched fibrin fibers, which are resistant to fibrinolysis.[63,64,93] A thrombin generation assay (TGA) was conducted to determine the maximum thrombin concentrations (MTC) of the functional nanofiber mats and controls (**Figures 3.5C and 3.S3**). BCCP showed the highest MTC of 148.3 ± 7.0 nM and was closely followed by the BMA modified mats with a MTC of 138.7 ± 6.1 nM, indicating both produce a high concentration of thrombin. The unmodified PCL mats displayed a slightly lower MTC of 127.1 ±

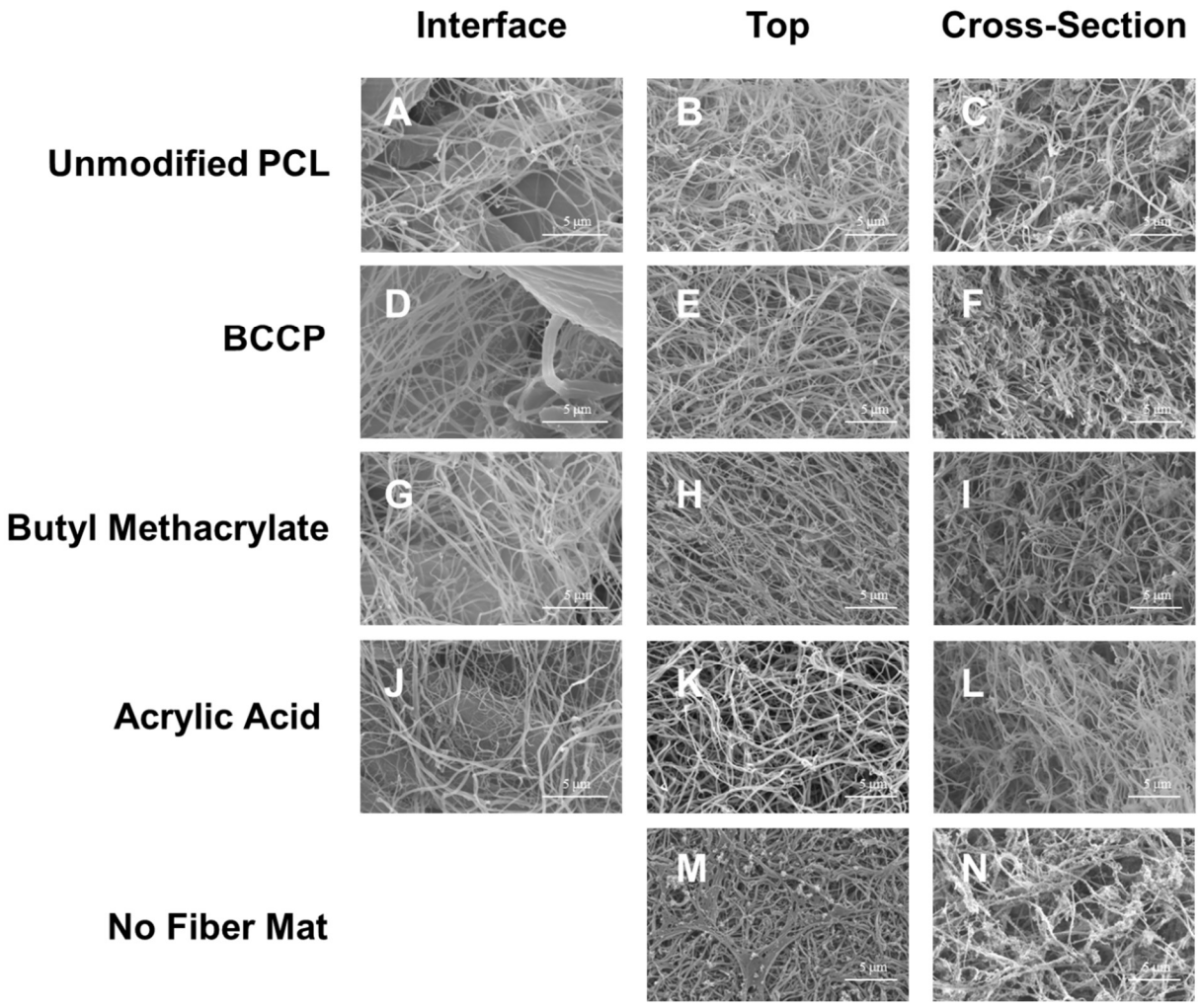

Figure 3.6: (A-N) Scanning electron micrograph of nanofiber mats of PCL (A-C), BCCP (D-F), butyl methacrylate (G-I), acrylic acid (J-L), and no nanofiber mat present (M,N). Images include clot-nanofiber interface (A,D,G,J), top of clots (B,E,H,K,M), and clot cross-sections (C,F,I,L,N) Scale bars indicate 5 µm.

7.3 nM, while the control clots without a fiber mat displayed a significantly lower MTC of 81.4 ± 7.0 nM. These values confirm that BCCP and BMA are improving the strength and stability of the fibrin clots due to increased thrombin levels when compared to controls. The AA modified mats show the lowest MTC value of 61.7 ± 5.5 nM. These results suggest that hydrophobicity of the surface is a major driving factor in blood clot development.

3.4.3.3 Fibrin Clot Analysis: Clots were analyzed by SEM to determine dimensions of the fibrin strands. Clots were imaged at the nanofiber/clot interface, the top of clots, and at a clot cross-section (**Figure 3.6**). Diameters of the fibrin strands were measured at 50 points per sample via ImageJ software and averaged (**Figure 3.7**). Thicker fibrin strands result in stronger clots that are more resistant to fibrinolysis.[63,64] The BCCP modified nanofiber mats displayed the largest fibrin

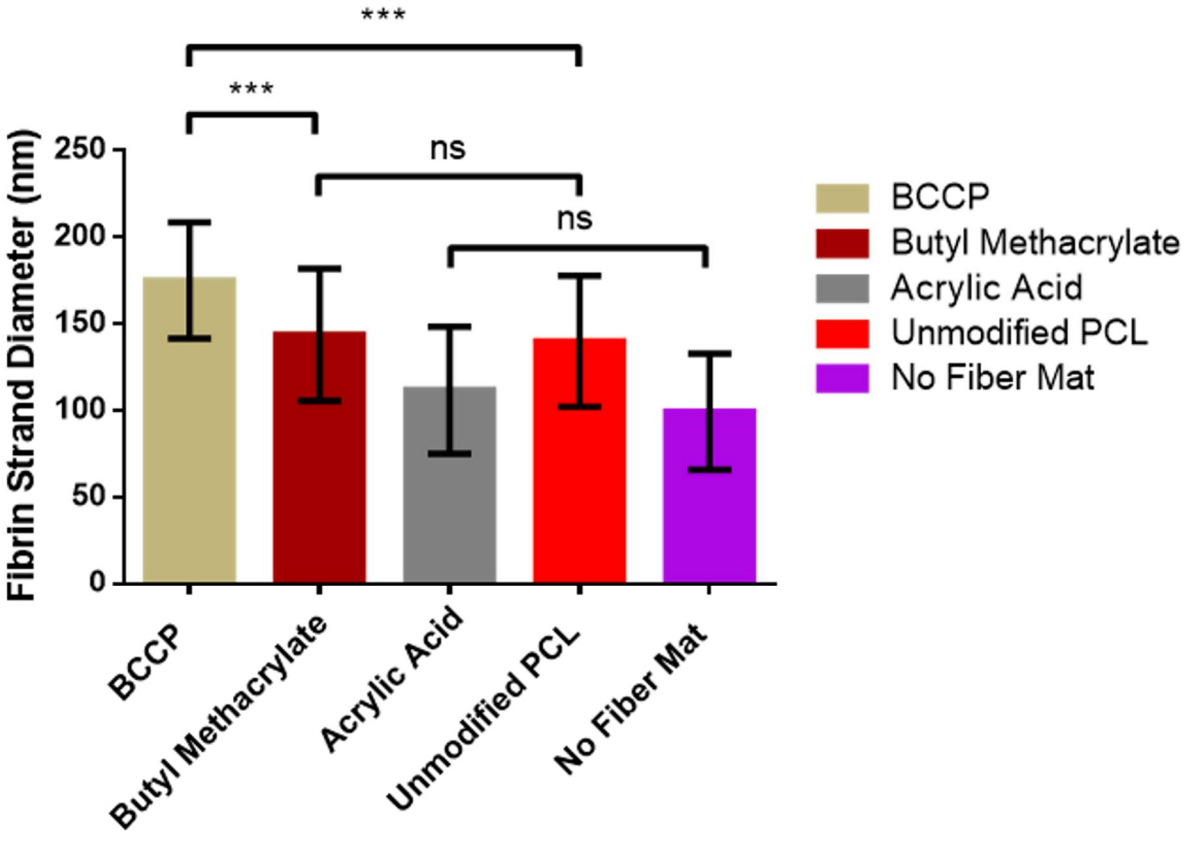

Figure 3.7: Plot of average fibrin strand diameters of *in vitro* blood clots. n = 50, ***p ≤ 0.001

strand diameter of 174.8 ± 33.4 nm, which is larger than the BMA mats with the next biggest diameter of 143.5 ± 38.1 nm. Unmodified PCL mats exhibit a diameter with no statistically significant difference from BMA of 139.7 ± 33.7 nm. Acrylic acid and clots without fiber mats have even lower diameters of 111.5 ± 36.6 nm and 99.1 ± 33.4 nm respectively. The clots formed from BCCP and BMA also appear to have the densest fibrin networks.

3.4.3.4 Discussion: PRT, MTC, and fibrin dimension model different attributes of the strength and stability of blood clots. As summarized in **Table 3.S1**, BCCP and BMA mats are consistently the top performing nanofiber mats with the lowest PRT and highest MTC while BCCP produces nanofibers with the largest fibrin diameters, outperforming BMA. BMA values are statistically equivalent to those of BCCP in PRT (191.4 ± 4.2 sec vs. 183.5 ± 9.2 sec) and MTC (138.7 ± 6.3 nM vs. 148.3 ± 7.1 nM), while the values of fibrin strand diameter show more distinct differences (143.5 ± 38.1 nm vs 174.8 ± 33.4 nm). This indicates that the addition of acrylic acid into the polymer chain in BCCP has a more significant impact on the physical dimensions of the material while the butyl methacrylate is more responsible for improving thrombin generation, which in turn speeds up clot formation. In all experiments, AA modified mats had a significantly lower performance than the BCCP and BMA mats, as well as the unmodified PCL. AA mats also performed worse than controls without a mat with respect to PRT and MTC, while extremely close in fibrin strand diameter. Hydrophobicity of the material appears to play a major role regarding clotting effectiveness, as the AA modified mats are significantly more hydrophilic than any other sample.

3.5 Conclusions: This work demonstrated the successful fabrication and in vitro demonstration of blood clot enhancing, nonwoven PCL nanofiber mats via a high-throughput melt coextrusion process followed by subsequent SI-ATRP. We demonstrated that the BCCP modified mats were

the most effective at accelerating time to clot, produced the most thrombin, and gave the thickest and most dense fibrin strands. Future work will entail the fabrication of multifunctional materials that combine this work with our previous antibacterial mats, along with other biomedically relevant uses such as antiviral and antifungal properties.

3.6 Acknowledgements: We gratefully acknowledge NSF Partnerships for International Research and Education (PIRE) (OISE 1844463) for their financial support. The Baer Group (Dr. Xinting Wang and Dr. Cong Zhang) is thanked for providing access and assistance with the melt coextrusion equipment. Dr. Erik Price is also acknowledged for his assistance with preparations for the melt coextrusion process. The Maia Group (Dr. Dana Klein) is thanked for providing access and assistance with the twin-screw extruder. We also acknowledge the use of facilities from the UC San Diego Materials Research Science and Engineering Center (UCSD MRSEC) (Ricardo De-Luna), grant DMR 2011924.

Chapter 3, in full, is a reprint of the material as it appears in Macromolecular Bioscience, Hochberg, J.D.; Wirth, D.M.; Pokorski, J.K., Wiley, 2022. The dissertation author was the primary researcher and author of this paper.

3.7 Supporting Information

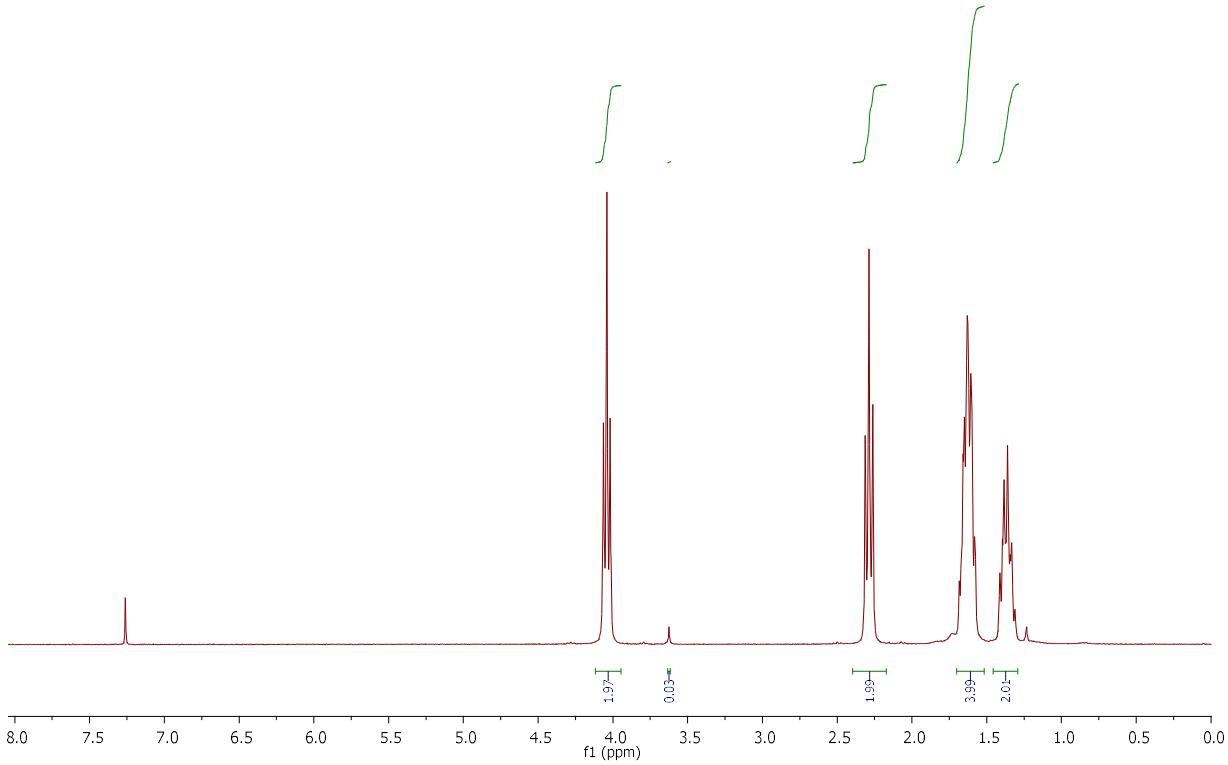

Figure 3.S1: NMR of washed PCL nanofiber. PCL: 1H NMR (300 MHz, CDCl3), δ(ppm): 4.06 (2H, t), 2.31 (2H, t), 1.66 (4H, quint), 1.38 (2H, quint). PEO: 1H NMR (300 MHz, CDCl3), δ(ppm): 3.65 (0.03H, s)

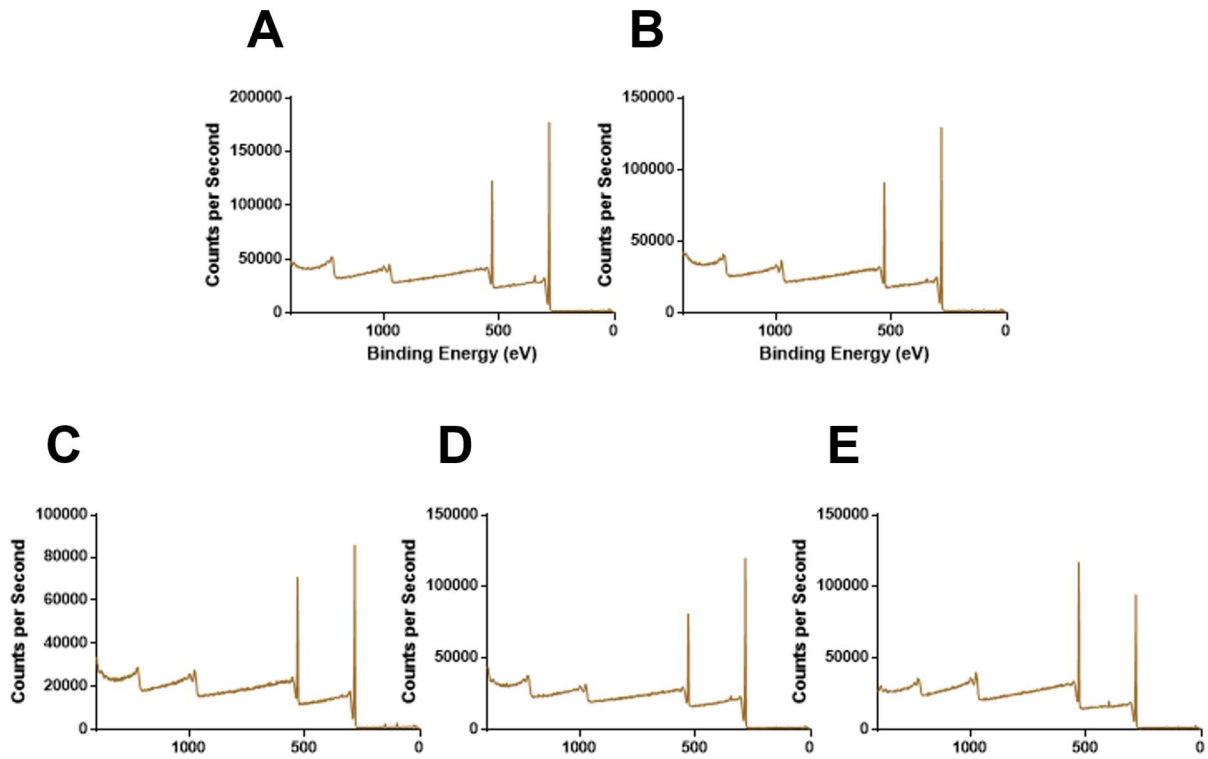

Figure 3.S2: High-resolution XPS survey spectra of (A) PCL, (B) initiator, (C) BCCP, (D) butyl methacrylate, and (E) acrylic acid functionalized nanofiber mats.

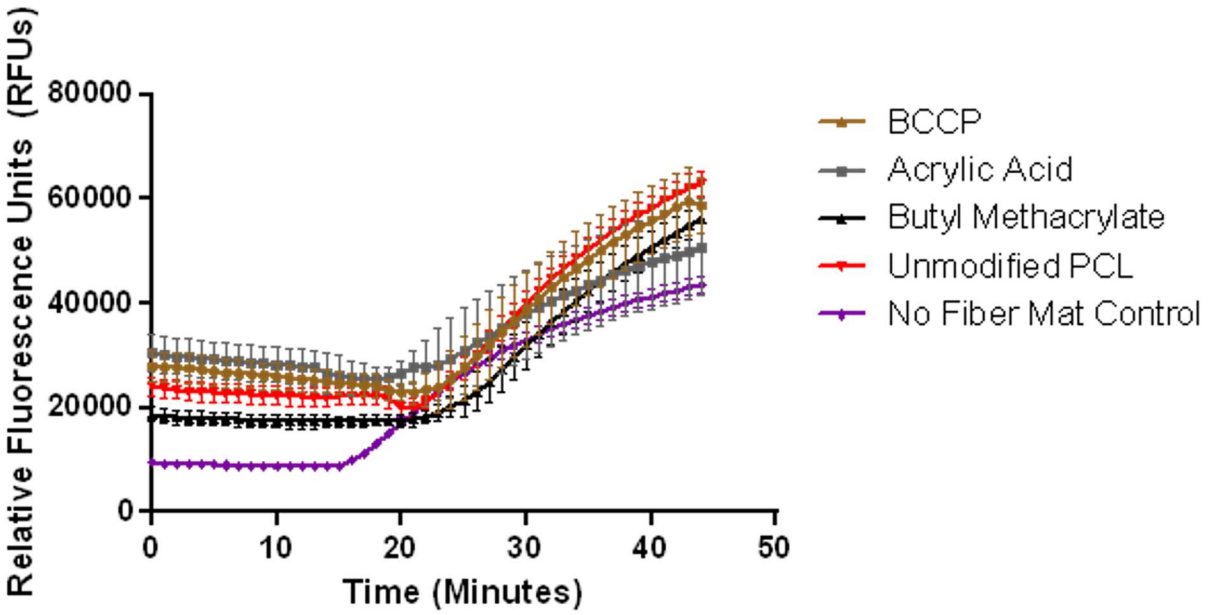

Figure 3.S3: Thrombin generation assay of clot from functionalized nanofibers

Table 3.S1: Table summarizing blood clotting data including plasma recalcification time, maximum thrombin concentration, and diameter of the fibrin strands.

Sample	Plasma Recalcification Time (in seconds)	Maximum Thrombin Concentration (nM)	Diameter of Fibrin Strands (nm)
BCCP	183.5 ± 9.2	148.3 ± 7.0	174.8 ± 33.4
Butyl Methacrylate	191.4 ± 4.2	138.7 ± 6.1	143.5 ± 38.1
Acrylic Acid	345.1 ± 11.3	61.7 ± 5.5	111.5 ± 36.6
Unmodified PCL	210.0 ± 1.4	127.1 ± 7.3	139.7 ± 37.7
No Fiber Mat	215.5 ± 6.4	81.4 ± 7.0	99.1 ± 33.4

CHAPTER 4: PET-RAFT TO EXPAND SURFACE-MODIFICATION CHEMISTRY OF MELT COEXTRUDED NANOFIBERS

4.1 Abstract: Polymeric nanofibers have been widely used as scaffolds for tissue engineering and drug delivery, as well as in filtration applications, among many others. A high-throughput melt coextrusion technique and post-processing functionalization chemistry was recently developed to fabricate functional fibers with nanoscale dimensions. This manuscript expands upon the development of nanofiber modification chemistry by functionalizing fiber mats via a surface-initiated photo-induced electron transfer reversible addition-fragmentation chain transfer (PET-RAFT) polymerization technique. PET-RAFT allows for the fabrication of chemically diverse nanofiber-based systems initiated with light, preventing the need for high temperature thermal initiators. This manuscript first describes the scope of monomers polymerizable via this technique. The PET-RAFT modification chemistry is further expanded upon to include block copolymers, an orthogonal RAFT-ATRP system, spatial photopatterning, and cell-adhesive capabilities. The development of surface-initiated PET-RAFT adds an additional tool to a growing strategy for nanofiber functionalization.

4.2 **Introduction:** Polymeric nanofiber materials have applications in a variety of fields including filtration,[18] energy storage,[94] and especially for use in various areas of biomedicine[4] including wound healing,[5] drug delivery,[95] and tissue engineering.[20,96] The most common method to fabricate nanofibers is electrospinning because it is inexpensive, simple to run, and can provide excellent control of nanofiber dimensions.[4,7] While electrospinning has been effectively used in a variety of research environments, it has a low maximum throughput of 200 g h^{-1},[10] and the size and quality of the fabricated nanofibers are heavily dependent on environmental conditions.[8,9] These downfalls significantly inhibit the commercial translation of the electrospinning technique.

Newer techniques exist as well, but many also feature innate limitations. Melt electrospinning is a similar technique that requires higher voltages while providing a lower throughput than normal electrospinning;[11] melt blowing has difficulty producing nanoscale fibers;[14] and rotary jet spinning produces fibers with weak mechanical properties.[12,13] Melt coextrusion has emerged recently for nanofiber fabrication that produces nanoscale fibers at scale, is solvent-free, and can fabricate nanofibers with robust mechanical properties at a rate of 2 kg $h^{-1}$when applied to a laboratory scale extruder.[15,17,77]

Polyesters are a common class of polymeric materials commonly used in extrusion processes. Polyesters are known to have useful mechanical properties, be easily modifiable, as well as use in a wide variety of applications. Examples of common polyesters include poly(glycolic acid) (PGA), poly(lactic acid (PLA), poly(lactic-co-glycolic acid) (PLGA), and poly(ε-caprolactone) (PCL). Specifically, PCL has a slow hydrolytic degradation rate of 2-3 years and is known for its flexibility, with PCL nanofibers being able to reach more than 700% elongation at break. [23,24]

Native PCL nanofibers have limited uses, particularly in biomedicine. While unmodified nanofibers have useful physical and mechanical properties, they must be chemically modified to exhibit functionally active properties to derive biomedical utility, including for applications in wound treatment[5] or tissue engineering.[25] To widen the breadth of applications of polymeric nanofibers, functional moieties can be introduced to the nanofiber surface. Various methods exist to introduce functionality onto polyesters include hydrolysis,[28] aminolysis,[27] end group modification,[26] and photochemical covalent insertion.[29] Chemical modification of polyester nanofibers has led to the formation of various useful materials including those promoting antibacterial properties,[5] antifouling properties,[30] and tissue engineering properties.[7,17,20]

This manuscript describes the fabrication of functional nanofiber mats via a surface initiated photoinduced electron transfer reversible addition−fragmentation chain transfer polymerization (PET-RAFT) mechanism via air tolerant conditions. PET-RAFT is a light-initiated controlled radical polymerization technique that is a simple method for nanofiber functionalization, which allows for the fabrication of nanofibers with a wide range of chemical functionalities and exhibits a high grafting efficiency.[70–72] Unlike similar techniques such as atom transfer radical polymerization (ATRP), this technique can be conducted under metal-free conditions and under ambient conditions without the need for rigorous degassing of the reaction solution. PET-RAFT has the added benefit of utilizing spatial patterning since polymerization occurs only in the presence of light. These attributes also allow PET-RAFT to be used in conjunction with other polymerization chemistries, such as ATRP to generate multifunctional materials.

4.3 Materials and Methods

4.3.1 Materials: Polyethylene Oxide (PEO) POLYOX N10 (100 kDa) and POLYOX N80 (200 kDa) were both purchased from Dow Chemical while CAPA 6800 PCL-80 kDa was purchased from The Perstorp Group. 4-Cyano-4-(dodecylsulfanylthiocarbonyl)sulfanylpentanoic acid was purchased from Strem Chemicals. 4-hydroxybenzophenone was purchased from Acros Organics. N,N'-Dicyclohexylcarbodiimide (DCC), Dimethylaminopyridine (DMAP), acrylic acid, poly(ethylene glycol) (PEG) methacrylate, fluorescein o-acrylate, 9-anthracenylmethyl acrylate, copper (I) bromide, and α-bromoisobutyryl bromide were purchased from Sigma-Aldrich. Methacrylic Acid was purchased from TCI America. Dimethylacrylamide (DMA), N-isopropylacrylamide (NIPAM), 9,10-dimethylanthracene zinc meso-tetraphenylporphine (ZnTPP), Dulbecco's Modified Eagle Medium (DMEM), and Detachin were purchased from

Fisher Scientific. Methacryloxyethyl thiocarbamoyl rhodamine B was purchased from Polysciences. GRGDS-acrylate was purchased from GenScript. 1-Bromohexane and tris(2-dimethylaminoethyl)amine (Me_6TREN) were purchased from Alfa Aesar. Phosphate buffered saline (PBS) pH 7.4 1X and penicillin-streptomycin (5,000 U/mL) were purchased from Gibco. Fetalgro Bovine Growth Serum was purchased from RMBio. NIH3T3 cell line was purchased from ATCC.

4.3.2 Instrumentation and Equipment: PEO was compounded in a Haake Rheodrive 5000 twin-screw extruder. Melt coextrusion was conducted on a custom, two-component system consisting of a series of vertical and horizontal multipliers. A SereneLifeSLPRWAS26 Compact Pressure Washer (1500 psi maximum pressure, 3 mm length by 11 mm width) was used to wash away excess PEO and entangle isolated nanofibers into mats. An Anytime Tools sharp 1/4″ hollow punch was used to shape nanofiber mats into circular patches. An Omnicure Model S1500 standard filter 320−500 nm UV light source was used for photo-chemical modification with benzophenone derivatives. A FEI Apreo LoVac FESEM was used for taking electron micrographs. Nuclear magnetic resonance data was obtained with a 300 MHz Bruker Avance III spectrometer. A custom-built light box (λ = 650 nm) was used for RAFT photochemistry. Water contact angle images were obtained with a ramé hart Model 200 goniometer. X-ray photoelectron spectroscopy data was obtained with a Kratos Analytical AXIS Supra surface analysis instrument. An Invitrogen EVOS FL Digital Inverted Fluorescence Microscope was used for fluorescent images. UV fluorescent mats were excited with a UVP UVGL-15 Compact UV Lamp (254/365 nm. 4 W, 0.16 A, 115 V, 60 Hz). Photographs of UV-patterned mats were taken with a Sony RX100 IV 20.1 MP Digital Camera. Confocal images were taken with a Leica SP8 Laser Confocal Microscope.

4.3.3 Methods

4.3.3.1 Melt Coextrusion of PCL/PEO Compound Tapes: Two different molecular weights of PEO (100 kDa and 200 kDa) were first dried in a vacuum oven at 40 °C for 48 hours, then compounded in a twin-screw extruder (140 °C) at a 70/30 w/w% ratio to provide a rheological match to PCL at the extrusion temperature.[97] Following compounding, the PEO and PCL pellets were dried for an addition 48 fours at 40 °C. PEO and PCL was then coextruded at 180 °C on an extrusion line consisting of 16 vertical and 4 horizontal multipliers with a 33% by volume PEO skin layer. The finished composite tape then existed through a 3" tape die and collected on a chill roll rotating at 15 rpm at room temperature.[30]

4.3.3.2 Nanofiber Isolation and Formation of PCL Mats: Composite PEO/PCL tapes were first secured in a beaker of stirring water for 6 hours; water was changed hourly. The tapes were then immersed in a 70% MeOH solution overnight, revealing PCL nanofibers. The nanofibers were subsequently secured to a fiberglass plate in a single layer and covered with a wire mesh to be washed with a pressure washer with varying spray sizes. The nonwoven nanofiber mats were then dried overnight in a vacuum desiccator before being punched out into 6 mm circular patches.

4.3.3.3 Synthesis of Nanofiber Inserting RAFT CTA (benz-CTA): 4-Cyano-4-(dodecylsulfanylthiocarbonyl)sulfanylpentanoic acid (0.810 g, 2.007 mmol), N, N′-dicyclohexylcarbodiimide (DCC) (0.497 g, 2.407 mmol), and 4-dimethylaminopyridine (DMAP) (0.078g, 0.030 mmol) were dissolved in 20 mL of dichloromethane (DCM) and stirred for 30 minutes at 0 °C to activate the carboxylic acid. 4-hydroxybenzophenone (0.398 g, 2.007 mmol) was dissolved in 10 mL of DCM and added dropwise to the reaction mixture. The ice bath was replaced, and the reaction was left to reach room temperature and proceed overnight. The reaction mixture was then placed at 4 °C for 20 minutes to allow dicyclohexylurea (DCU) to fully

precipitate before being filtered off and the crude product concentrated *in vacuo*. The crude product was then redissolved in a small amount of DCM and washed twice with sodium bicarbonate, and three times with water. The organic layer was dried over anhydrous sodium sulfate and concentrated *in vacuo*. The crude product was purified via column chromatography with 25% ethyl acetate and 75% hexane. Once the product was collected, it was once again concentrated *in vacuo* to yield a sticky yellow solid. Yield: (0.853g, 1.456 mmol, 72.8%) ^{1}H NMR (300 MHz, $CDCl_3$), δ(ppm): 7.86 (2H, dt), 7.79 (2H, dt), 7.60 (1H, tt), 7.50 (1H, tt), 7.24 (2H, dt), 3.35 (2H, t), 2.94 (2H, t), 2.59 (2H, m), 1.95 (3H, s), 1.71 (2H, quint), 1.40 (2H, quint) 1.26 (16H, s), 0.88 (3H, t).

4.3.3.4 Nanofiber Functionalization with RAFT benz-CTA: Nonwoven nanofiber mats (6 mm diameter, ~4.5 mg) were added to a 7.5 mg/mL solution of benz-CTA in MeOH and then placed in a vacuum desiccator and dried overnight. The mats were then placed underneath a broadband UV lamp (λ = 320 – 500 nm, 548 mW/cm^2) for 35 minutes per side. Functionalized mats were washed three times with MeOH and dried overnight in a vacuum desiccator. CTA functionalization was confirmed via water contact angle (WCA) and X-ray photoelectron spectroscopy (XPS).

4.3.3.5 Surface Initiated PET-RAFT: CTA-functionalized mats, monomer (1.388 mmol), ZnTPP (0.05 mg, 47 μL of 1 mg/mL solution, 0.069 μmol), 9,10-dimethylanthracene (1.57 mg, 0.008 mmol), and benz-CTA (4.05 mg, 0.007 mmol) were added to 2 mL of DMSO in a 20 mL scintillation vial and placed under red light (λ = 650 nm, 81 mW/cm^2) for 3 hours. Mats were then washed three times in MeOH and dried in a vacuum desiccator overnight. Polymer functionalization was confirmed via WCA and XPS.

4.3.3.6 Preparation of Fluorescently Labeled Nanofiber Mats

4.3.3.6.1 Preparation of Block Copolymer Mats: To graft block copolymers from the nanofiber surface, **4.3.3.5** was conducted twice. The first time utilizing 99% acrylic acid (99 mg,

1.374 mmol) and 1% fluorescein o-acrylate (5.3 mg, 0.014 mmol) as the monomers, and the second time utilizing 99% acrylic acid (99.0 mg, 1.374 mmol) and 1% methacryloxyethyl thiocarbamoyl rhodamine B (8.9 mg, 0.014 mmol) as the monomers. Polymer functionalized nanofiber mats were washed three times in MeOH and vacuum dried overnight. Polymer functionalization was confirmed via WCA and XPS and mats were then imaged under the FITC and Texas Red settings of a fluorescent microscope.

4.3.3.6.2 Preparation of Orthogonal RAFT/ATRP Mats: Following CTA functionalization in Section **4.3.3.4**, nanofiber mats were then incubated with a similar benz-ATRP initiator in 10 mg/mL in MeOH whose synthesis has been described previously.[5] Saturated mats were once again placed underneath a broadband UV lamp (λ = 320 – 500 nm, 548 mW/cm^2) for 35 minutes per side, washed three times with methanol, then dried overnight in a vacuum desiccator. PET-RAFT was then conducted as described in section **4.3.3.5**, with 99% acrylic acid (99 mg, 1.374 mmol) and 1% fluorescein o-acrylate (5.3 mg, 0.014 mmol) as the monomers. Polymer functionalized mats were then washed three times with MeOH and dried overnight in a vacuum desiccator. Surface initiated atom transfer radical polymerization (SI-ATRP) was then conducted off the nanofibers. Acrylic acid/fluorescein o-acrylate modified mats, 99% acrylic acid (99.0 mg, 1.374 mmol) and 1% methacryloxyethyl thiocarbamoyl rhodamine B (8.9 mg, 0.014 mmol) as the monomers, Me_6TREN, and dimethylformamide (2mL) were added to a three-neck round bottom flask and bubbled with N_2 gas for 50 minutes. Cu(I)Br (4.0 mg, 0.028 mmol) was then added under positive pressure. The reaction was allowed to proceed overnight at room temperature. The orthogonally modified mats were then washed three times with MeOH and dried in a vacuum desiccator. Polymer functionalization was confirmed via WCA and XPS and mats were then imaged under the FITC and Texas Red settings of a fluorescent microscope.

4.3.3.7 Preparation of Patterned, UV Fluorescent Nanofiber Mats: Unmodified PCL mats were functionalized as described in section **4.3.3.4** with a photomask displaying "UCSD" on top. PET-RAFT was conducted as described in section **4.3.3.5**, with 99% acrylic acid (99 mg, 1.374 mmol) and 1% 9-anthracenylmethyl acrylate (3.6 mg, 0.014 mmol) as the monomers. Polymer functionalized mats were then washed three times with MeOH and dried overnight in a vacuum desiccator. A handheld UV lamp (λ = 365 nm, 0.16 A) and a photograph was taken.

4.3.3.8 Preparation of Cell Adhesion Peptide Modified Nanofiber Mats: PET-RAFT was conducted as described in section **4.3.3.5**, with 99% PEG methacrylate (493 mg, 1.374 mmol) and 1% GRGDS acrylate (7.6 mg, 0.014 mmol). Polymer mats were also prepared with 100% PEG methacrylate (500 mg, 1.388 mmol) as a control. Polymer functionalized mats were then washed three times with MeOH and dried overnight in a vacuum desiccator. Polymer functionalization was confirmed via WCA and XPS.

4.3.3.9 Patterning of Cell Adhesion Peptide Modified Mats: Mouse fibroblasts (NIH3T3) were cultured in a T75 tissue culture flask in DMEM supplemented with 10% by volume FetalGro serum, 1% by volume L-glutamine, and 1% by volume 5,000 U/mL penicillin-streptomycin. Cells were grown to 85% confluence in an environment with 5% CO_2 and a relative humidity of 95%, then washed with 5 mL of PBS and trypsinized with 5 mL of Detachin for 5 minutes. Cells were then washed with PBS and centrifuged before being stained with 0.1 μg/mL Hoechst 33342 in media without serum. The cells were then washed and centrifuged three more times with PBS before being redissolved in 1 mL of media and counted with a hemocytometer. PEG methacrylate/GRGDS, 100% PEG methacrylate, and unmodified nanofiber mats were then placed in individual sections of a 4-section glass bottom petri dishes and covered with 0.5 mL of 625

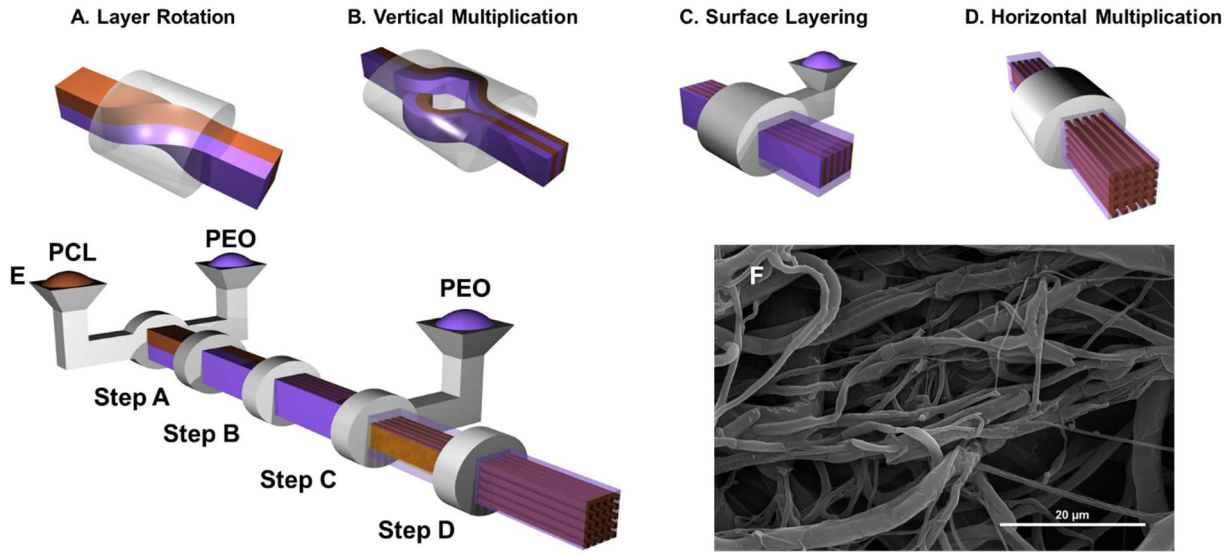

Figure 4.1: (A-E) Schematic diagram of melt coextrusion system describing steps within the extrusion line (A) layer rotation, (B) vertical multiplication, (C) surface layering, (D) horizontal multiplication procedures, and (E) overview of system. (F) Scanning electron micrograph of extruded and isolated nanofibers (scale bar = 20 µm).

cells/mm^2. Cells adhered to the nanofiber mats were then imaged with confocal microscopy using the DAPI setting.

4.4 Results and Discussion

4.4.1 Melt Coextrusion of PCL/PEO Compound Tapes: In this work we chose to fabricate composite tapes comprised of PCL nanofibers embedded within a sacrificial PEO matrix. PCL is chosen as the nanofiber material due to the ability for post-extrusion modification, biocompatibility, and ductility. PEO is used as a sacrificial coextrudate because blending of different molecular weights results in an immiscible rheological match to PCL, leading to distinct layering. In addition, PEO is water soluble allowing for a simple aqueous dissolution of the sacrificial material to reveal nanofibers. PCL and PEO are coextruded by individually melt-pumping the two polymers in vertically oriented layers in the extrusion line. The layers are then rotated 90° to orient the polymer melts to flow side-by-side (**Figure 4.1A**). The melt flow is then fed into a series of vertical multipliers, which effectively double the number of layers, thus creating a total of 2^{n+1} total vertical layers, where "n" is the number of vertical multipliers (**Figure 4.1B**).

A 33% skin layer of PEO then covers the top and bottom of the polymer melt (**Figure 4.1C**). Lastly, a series of horizontal multipliers yields the nanoscopic PCL domains embedded inside of the PEO matrix after the melt exits the set-up through a 3" tape die (**Figure 4.1D**). This entire process (**Figure 4.1E)** yields 2^m horizontal layers and 2^{n-m} vertical layers, where "m" is the number of horizontal multipliers. This work utilized 16 vertical and 4 horizontal layers, resulting in 4096 × 16 PCL nanofiber domains within the PEO matrix (**Figure 4.1F**).

4.4.2 Formation of PCL Nanofiber Mats: After extrusion, the PCL nanofibers are embedded in the PEO matrix of a composite tape. Composite tapes were washed in a stirring water bath for 6 hours, with the water being replaced every hour. This water bath is followed by a 70% MeOH bath overnight. Nanofibers are then sprayed with a high-pressure water jet to both remove any remaining PEO. This water jetting step yields nanofibers with a 97% PEO removal via NMR (**Figure 4.S1**). Nanofiber mats are then punched into a disc with a diameter of 6 mm.

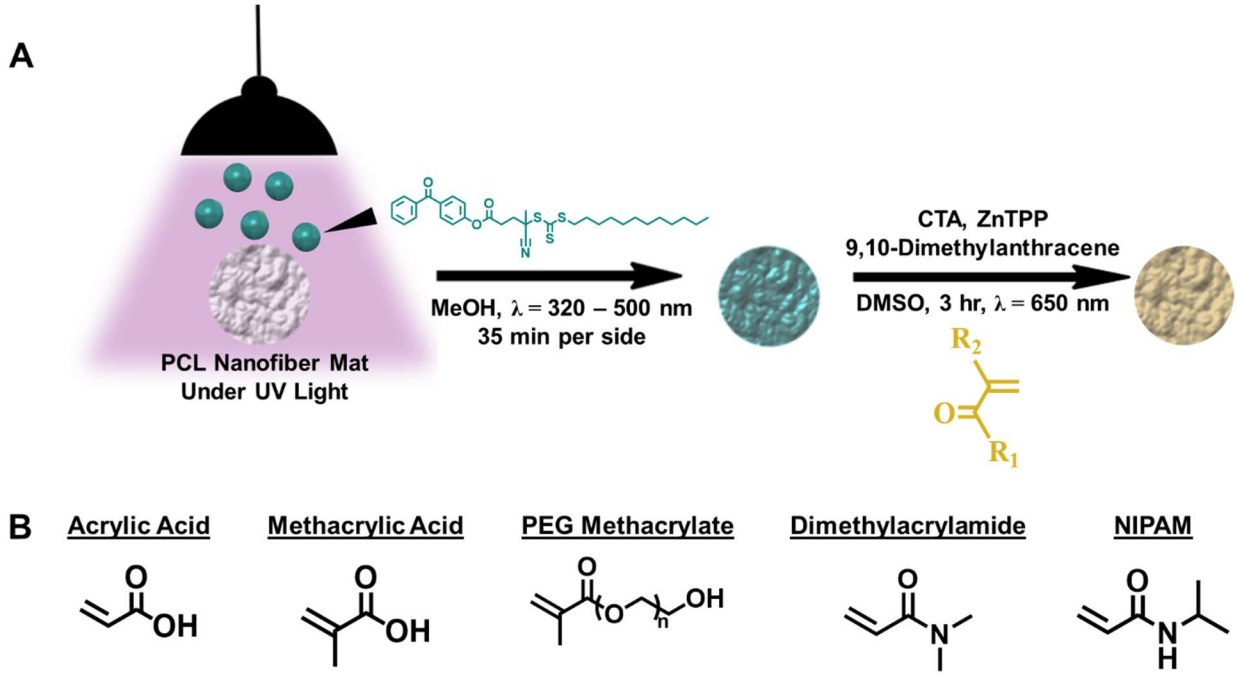

Figure 4.2: Overview of PET-RAFT nanofiber functionalization including (A) reaction schematic, (B) monomers used in main functionalizations

4.4.3 Functionalization of Nanofiber Mats with RAFT CTA: A RAFT (reversible addition-fragmentation chain transfer) CTA (chain transfer agent) needed to be conjugated to the PCL backbone of the nanofibers to graft polymers off the surface of the nanofiber mats (**Figure 4.2A**). A CTA-modified benzophenone was first synthesized (**Figure 4.S2**) via a Steglich Esterification[98] prior to nanofiber insertion. Under UV light, benzophenone is known to undergo a hydrogen abstraction which allows insertion of the molecule into the PCL backbone.[29] We aimed to take advantage of this mechanism for the insertion of our CTA-modified benzophenone molecule into the PCL chains of our nanofiber mats. The mats were first dip-coated in a solution containing the benzophenone-CTA, subsequently dried under vacuum, then illuminated under UV light to initiate the photochemical insertion. This process yielded nanofibers functionalized with a RAFT CTA ready to undergo further functionalization and characterized via WCA and XPS (**Figure 4.3**).

4.4.4 *Grafting-from* PET-RAFT: Photoinduced electron transfer RAFT (PET-RAFT) was conducted from the CTA anchored on the nanofiber mats using red light to initiate the

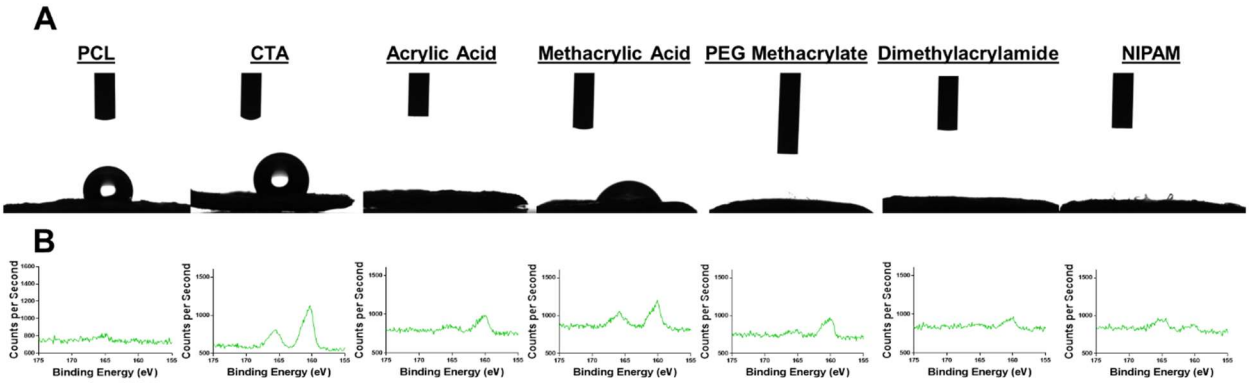

C

Fiber Sample	Percent Composition				Water Contact Angle
	C	O	N	S	
Unmodified PCL	80.5	19.5	0.0	0.0	83.7 ± 0.6°
CTA	79.6	19.7	0.3	0.4	111.0 ± 14.0°
Acrylic Acid	79.0	20.7	0.2	0.1	0.0°
Methacrylic Acid	78.8	20.5	0.5	0.2	73.4 ± 1.6°
PEG Methacrylate	77.4	22.4	0.1	0.1	0.0°
Dimethylacrylamide	80.5	18.0	1.4	0.1	0.0°
NIPAM	78.4	20.6	0.9	0.1	0.0°

Figure 4.3: Characterizations of functionalized nanofiber mats including (A) water contact angles, (B) High resolution X-ray photoelectron spectroscopy of S2p of the various nanofiber mats, and (C) an overview of the characterization data.

polymerization (**Figure 4.2A**). The main purpose of this project was to further develop and expand on the chemistries used to create functional nanofiber materials. One main aim with these materials is to improve their biocompatibility even during preparations. PET-RAFT helps this aim for many reasons. Firstly, utilizing a visible light-based initiator instead of a thermal-based initiator allows materials to be formed at a wide range of temperatures. While this is useful in biosystems, it is also necessary to perform these reactions at lower temperatures due to PCL's low melting point of ~60 °C.[99,100] Compared to similar ATRP methods, RAFT chemistries do not require a transition metal catalyst, instead obtaining their living characteristics from the CTA. This negates the need to use potentially cytotoxic heavy metals in the polymerization system.[101] Another benefit of both simplicity and biocompatibility is the oxygen tolerant nature of this technique due to the addition of 9,10-dimethylanthracene, which acts as an oxygen scavenger.[72]

A library of monomers (**Figure 4.2B**) was used to explore the breadth of chemistries possible with this technology and included acrylic acid, methacrylic acid, PEG methacrylate, dimethylacrylamide, and NIPAM. WCA and XPS (**Figure 4.3**) were used to characterize the polymer modified nanofiber mats.

WCA results showed a significant increase in the hydrophobicity of the PCL nanofiber mats upon modification with the benzophenone-CTA, from a contact angle of 83.7 ± 0.6° to 111.0 ± 14.0°. This large increase is mostly due to the long hydrocarbon tale of the CTA. Upon modification was the selected polymers however, the nanofiber mats become extremely hydrophilic. Mats modified with acrylic acid, PEG methacrylate, dimethylacrylamide, and NIPAM fully wet with a contact angle of 0° as expected. While methacrylic acid mats increased in hydrophilicity reaching a contact angle of 73.4 ± 1.6°, the mats did not fully wet due to the additional methyl group in the polymer backbone.

Upon modification with the CTA, XPS integrations show that the nanofiber mats contain a small percentage of nitrogen and sulfur, 0.3% and 0.4% respectively, and continue to show evidence of CTA presence throughout the polymerizations. Polymerized nanofiber mats show evidence of polymer modification via there shifting of ratios between carbon and oxygen contribution. PEG methacrylate modified mats specifically show a noticeable increase in oxygen presence as compared with the other nanofiber mats. These results show the ability of this technique to decorate the nanofiber surface with a wide variety of different functionalities.

4.4.5 Preparation of Fluorescently Labeled Nanofiber Mats

4.4.5.1 Block Copolymer Mats: The unique nature of the CTA modified nanofiber mats allows for the implementation of more complex chemistries since PET-RAFT is very functional group compatible, such as block copolymer (**Figure 4.4A**) and orthogonally functionalized (**Figure 4.4B**) mats. Of particular use is the ability to graft block copolymers from the nanofiber mats due to the lack of termination events in RAFT chemistry. This lack of termination events allowed for "living" chain ends to exist after polymerizations have reached completion and the materials have been cleaned and stored.

To illustrate the living nature of the modified nanofiber mats, a diblock was grafted from the nanofiber surface via PET-RAFT using fluorescent monomers. Both blocks contained 99% acrylic acid with a small amount of fluorescent dopant. The first block was functionalized with 1% fluorescein acrylate (green) while the second block was functionalized with rhodamine B (red).

A. Block Copolymers:

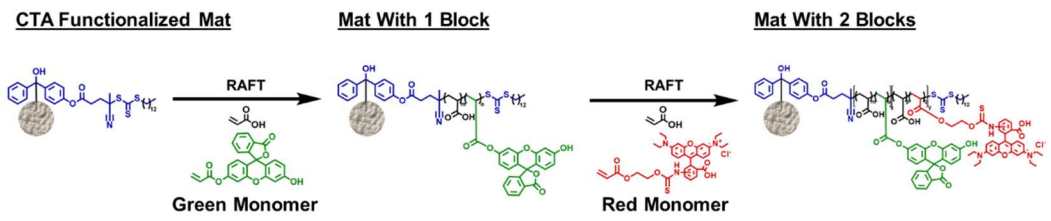

B. Orthogonal Chemistry:

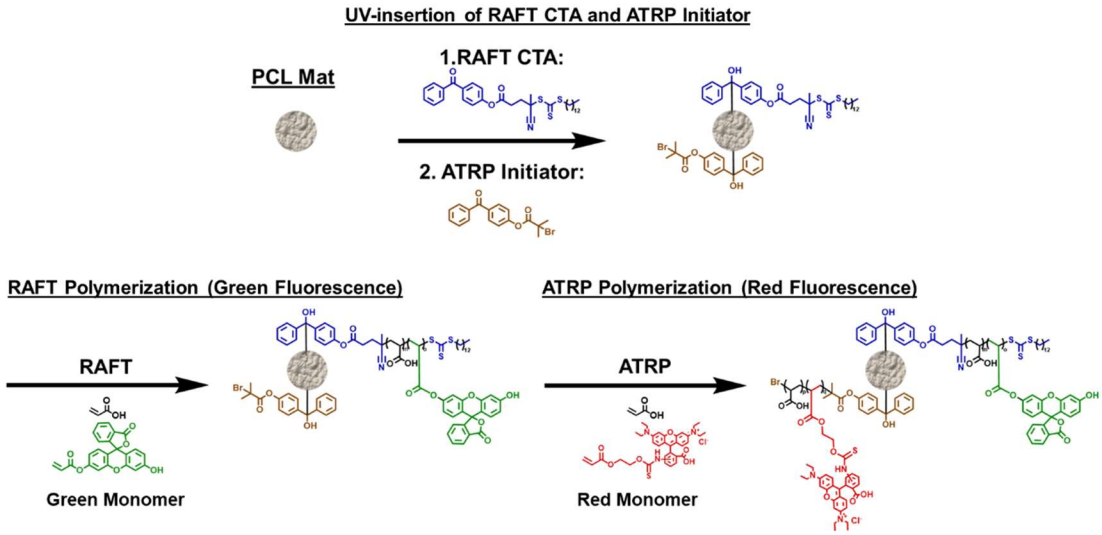

Figure 4.4: Reaction scheme of (A) block copolymer modified nanofiber mats and (B) RAFT/ATRP orthogonally modified nanofiber mats.

When compared with unmodified PCL mats (**Figure 4.5A, E, and I**) that showed no fluorescence and mats modified only with fluorescein acrylate via PET-RAFT, which showed only green fluorescence, the RAFT block copolymer modified mats (**Figure 4.5C, G, and K**) showed strong green and red fluorescence. This strong fluorescence in both regions indicated the successful functionalization via two subsequent polymerization reactions.

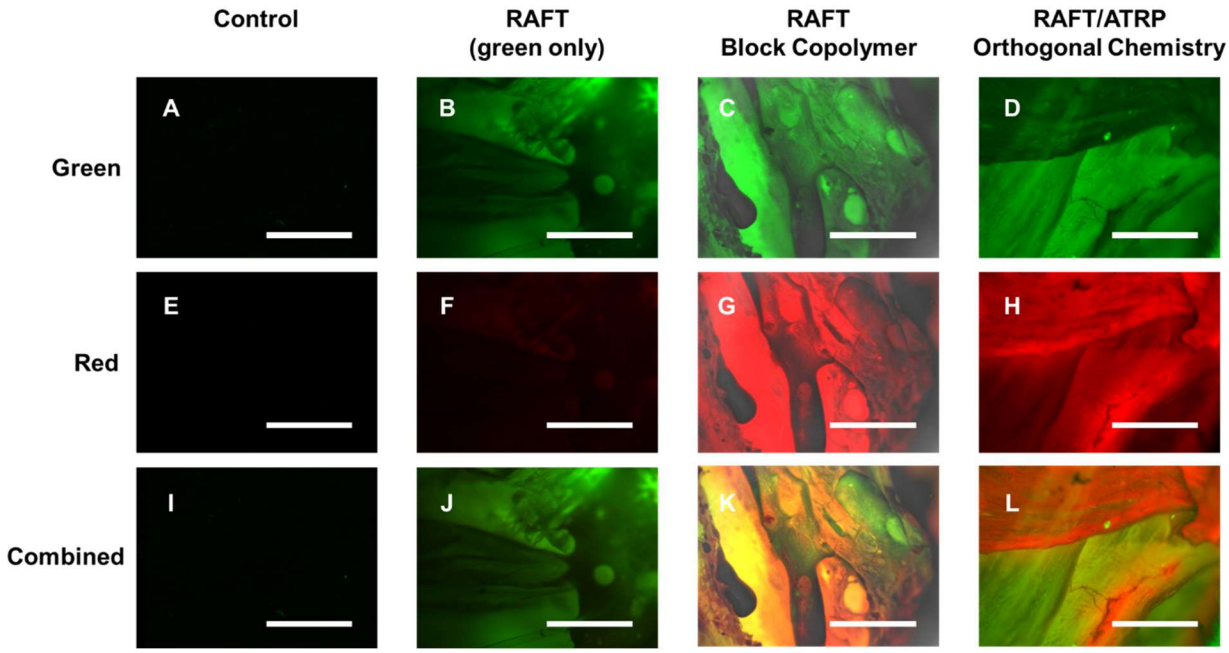

Figure 4.5: Fluorescent images of nanofibers showing (A-D) green fluorescence, (E-H) red fluorescence, and (I-L) combined green and red fluorescent channels. Samples include (A,E,I) unmodified PCL nanofibers, (B,F,J) nanofibers mats only modified with the green fluorescent monomer via a single PET-RAFT reaction, (C,G,K) RAFT block copolymer modified nanofiber mats, and RAFT/ATRP orthogonally modified nanofiber mats (scale bar = 1 mm).

4.4.5.2 Orthogonal Chemistry Mats: An analogous method to modify the nanofibers with separate colors was developed utilizing two different chemistries orthogonally. In addition to the RAFT CTA modifying the nanofiber mats, an atom transfer radical polymerization (ATRP) initiator was also conjugated to a benzophenone unit and radically inserted into the PCL backbone. PET-RAFT was then conducted with 99% acrylic acid and 1% fluorescein acrylate once again for green fluorescence, however this time for the red fluorescence, 99% acrylic acid and 1% rhodamine B was polymerized off the nanofiber via ATRP. This once again provides nanofibers displaying green and red fluorescence as with the block copolymer modified mats, but via an orthogonal chemical technique.

As with the block copolymer modified mats, the RAFT/ATRP orthogonally modified mats (**Figure 4.5D, H, and L**) showed strong green and red fluorescence, once again indicating the successful functionalization of the nanofiber mats with two subsequent reactions. It is important to note the difference in the chemical structure of the grafted polymers between methods. While

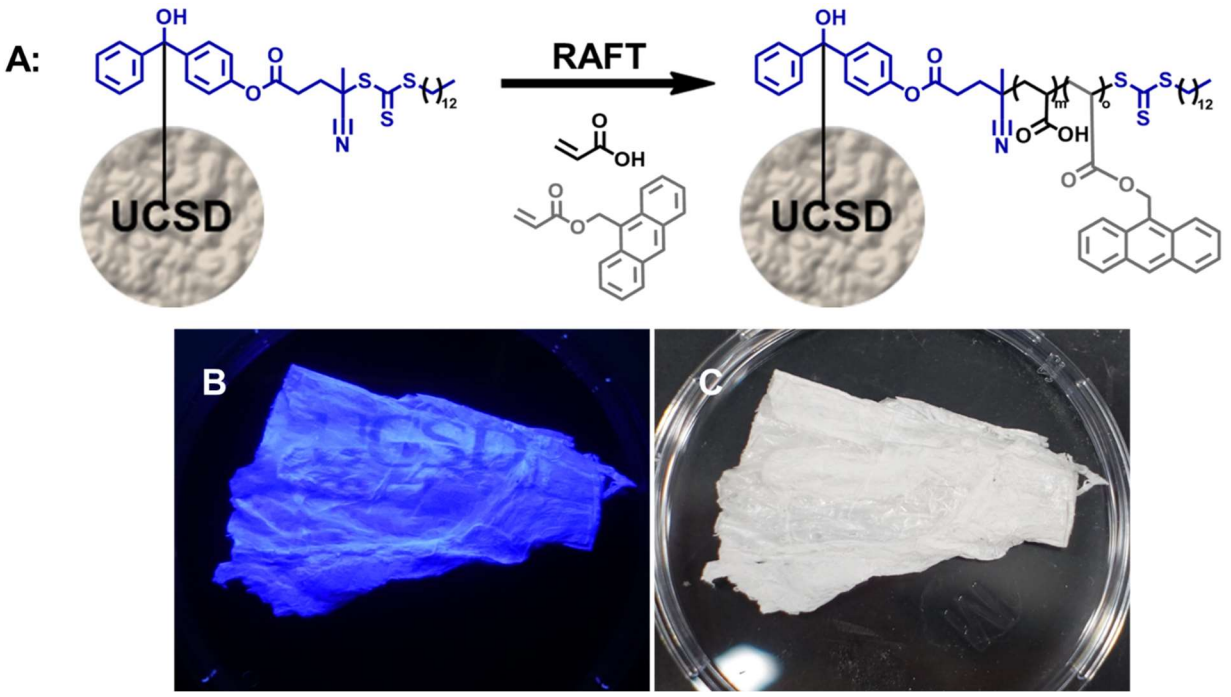

Figure 4.6: (A) Chemical scheme of nanofiber mat functionalization with acrylic acid and UV active monomer. Photograph of nanofiber mat patterned with "UCSD" (B) illuminated with UV light and (C) under regular overhead lights.

the block copolymer modified mats will consist of single chains containing both the green and red blocks, the orthogonally modified mats will only have green chains grafted from the CTA and only red chains grafted from the ATRP initiator due to the differences in polymerization mechanisms mediated by the CTA or ATRP initiator. However, both methods are effective at functionalizing the nanofiber mats with two distinct chemical functionalities.

4.4.6 Preparation of UV Patterned Nanofiber Mats: Photopatterning was conducted to further demonstrate the versatility of RAFT nanofiber mat technology. A photomask with the letters UCSD (representing University of California, San Diego) was placed on a larger nanofiber mat during photoinsertion of the benzophenone-CTA into the PCL backbone. Due to this photomask placement, CTA was only inserted where the letters UCSD were situated. PET-RAFT was then conducted with 99% acrylic acid and 1% UV active monomer (9-anthracenylmethyl acrylate) (**Figure 4.6A**). A handheld UV lamp was then illuminated on top of the patterned nanofiber mat

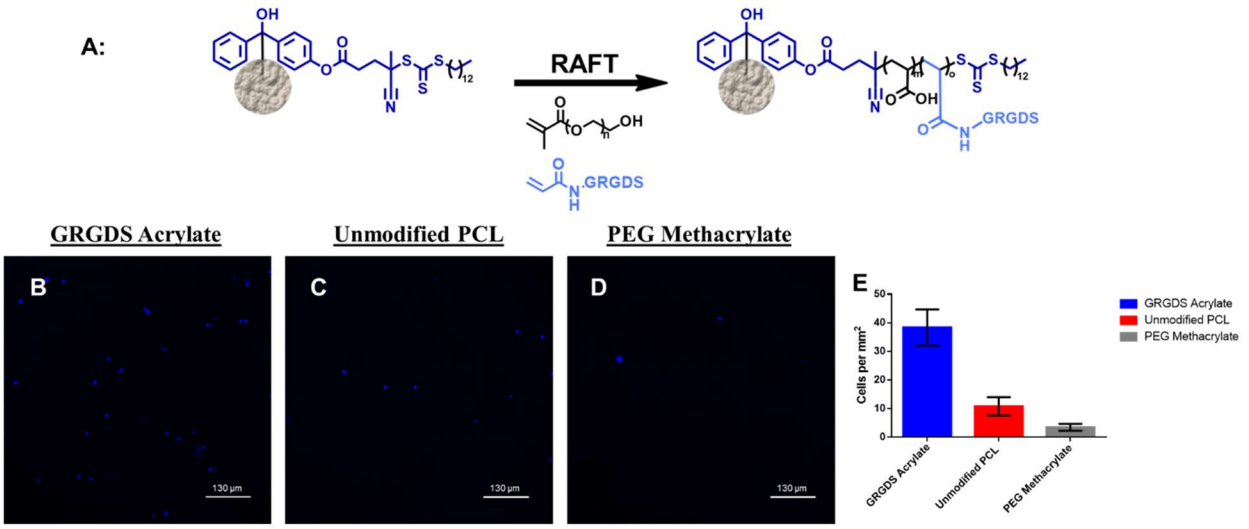

Figure 4.7: (A) Chemical scheme of nanofiber mat functionalization with PEG methacrylate and GRGDS acrylate. Confocal microscopy images of cells on nanofibers (B) functionalized with GRGDS acrylate, (C) unfunctionalized, and (D) functionalized with an antifouling PEG methacrylate polymer (scale bar = 130 µm). (E) Plot of cells on nanofiber mats per mm^2

and a photograph was taken (**Figure 4.6B**) and compared with a photograph under normal overhead lights (**Figure 4.6C**).

4.4.7 Cell Adhesion Peptide Modified Mats: A peptide-based monomer was used to functionalize the nanofiber mats to demonstrate further utility of this technology. CTA modified nanofiber mats were functionalized with 99% PEG methacrylate and 1% GRGDS-acrylate as well as 100% PEG methacrylate as a control (**Figure 4.7A**). The GRGDS peptide motif is well known to promote cell adhesion.[102–104]

Mouse fibroblasts (NIH3T3) stained with a Hoechst dye were seeded on peptide modified mats, unmodified mats, and PEG methacrylate modified mats. PEG covered surfaces are known to possess antifouling properties, preventing cells from attaching to surfaces.[30] Cell seeded nanofibers were imaged via confocal microscopy after incubating overnight (**Figure 4.7**). Peptide-modified nanofibers (**Figure 4.7B**) exhibited 38.4 ± 6.3 cells/mm^2, which is nearly a 4X increase when compared with unmodified PCL mats (**Figure 4.7C**) (10.8 ± 3.2 cells/mm^2) and a more than 10X increase when compared with PEG methacrylate antifouling mats (**Figure 4.7D**) (3.5 ± 1.2

cells/mm^2). These significant decreases in cell density (**Figure 4.7E**) confirm that the GRGDS motif significantly increases the binding ability of cells onto the nanofiber surface, opening up these materials for significant tissue engineering applications in the future.

4.5 Conclusion: This manuscript demonstrated the successful preparation of functional nanofiber mats via a high-throughput melt coextrusion process followed by functionalization via PET-RAFT. We demonstrated the diverse utility of this technique with a large library of polymers *grafted-from* the nanofiber surface as well as the ability for complex chemistries and uses including functionalizing with block copolymers, an orthogonal RAFT-ATRP system, photopatterning, and cell patterning capabilities. Future work will expand on this chemistry by entering the tissue engineering realm, and using cell adhesion peptide functionalized mats to adhere mesenchymal stem cells to the mats, allowing the differentiation into various cell types via dynamic mechanical stimuli.[105]

4.6 Acknowledgements: J.K.P., J.D.H., and D.M.W. acknowledge NSF Partnerships for International Research and Education (PIRE) for financial support (OISE 1844463). The Baer Group (Dr. Xinting Wang and Dr. Cong Zhang) is acknowledged for the access and assistance with running the melt coextrusion system. Dr. Erik Price is acknowledged for his assistance with preparations for the melt coextrusion process. The Maia Group (Dr. Dana Klein) is acknowledged for assistance with the twin-screw extruder system. We also acknowledge the use of UC San Diego Materials Research Science and Engineering Center (UCSD MRSEC) facilities (Ricardo De-Luna), grant DMR 2011924. The UCSD Microscopy Core (NINDS P30NS047101) is acknowledged for confocal microscope access.

Chapter 4, in part is currently being prepared for submission for publication of the material. Hochberg, J.D.; Wirth, D.M.; Pokorski, J.K. The dissertation author was the primary researcher and author of this material.

4.7. Supporting Information

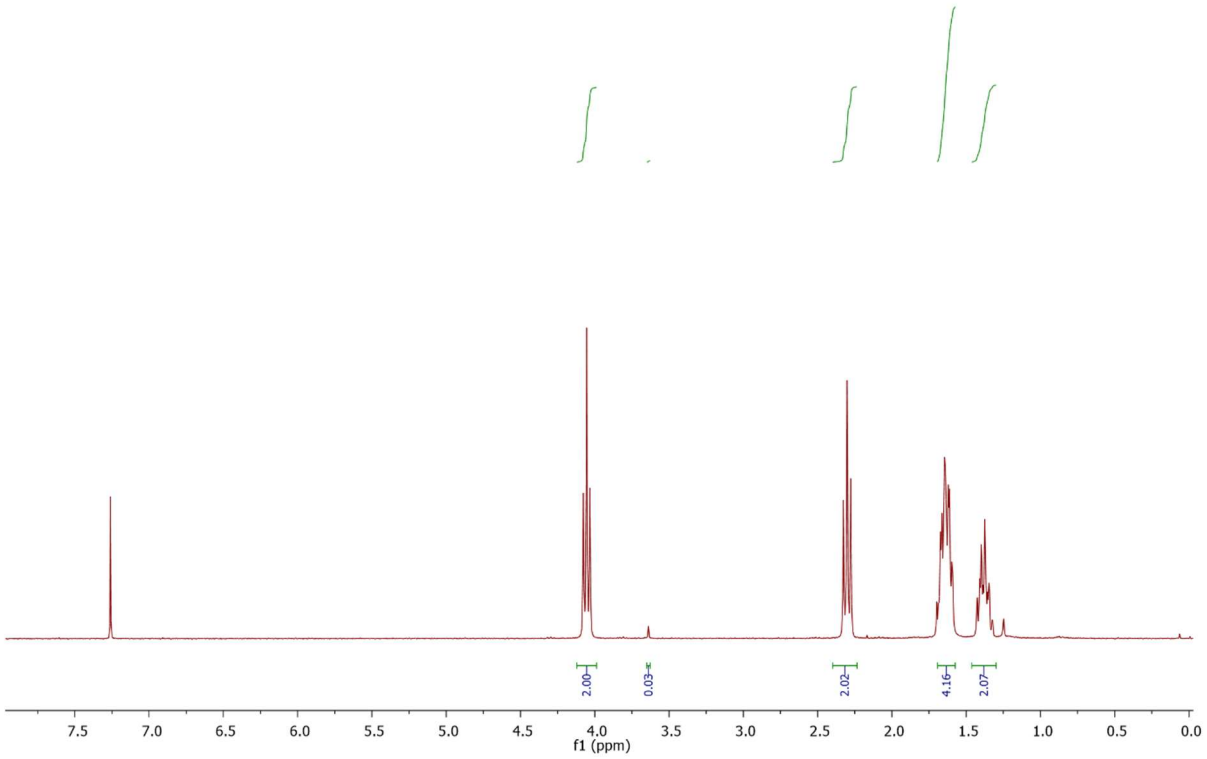

Figure 4.S1: NMR of isolated PCL nanofibers. PCL: 1H NMR (300 MHz, CDCl3), δ(ppm): 4.06 (2H, t), 2.30 (2H, t), 1.65 (4H, quint), 1.39 (2H, quint). PEO: 1H NMR (300 MHz, CDCl3), δ(ppm): 3.64 (0.03H, s)

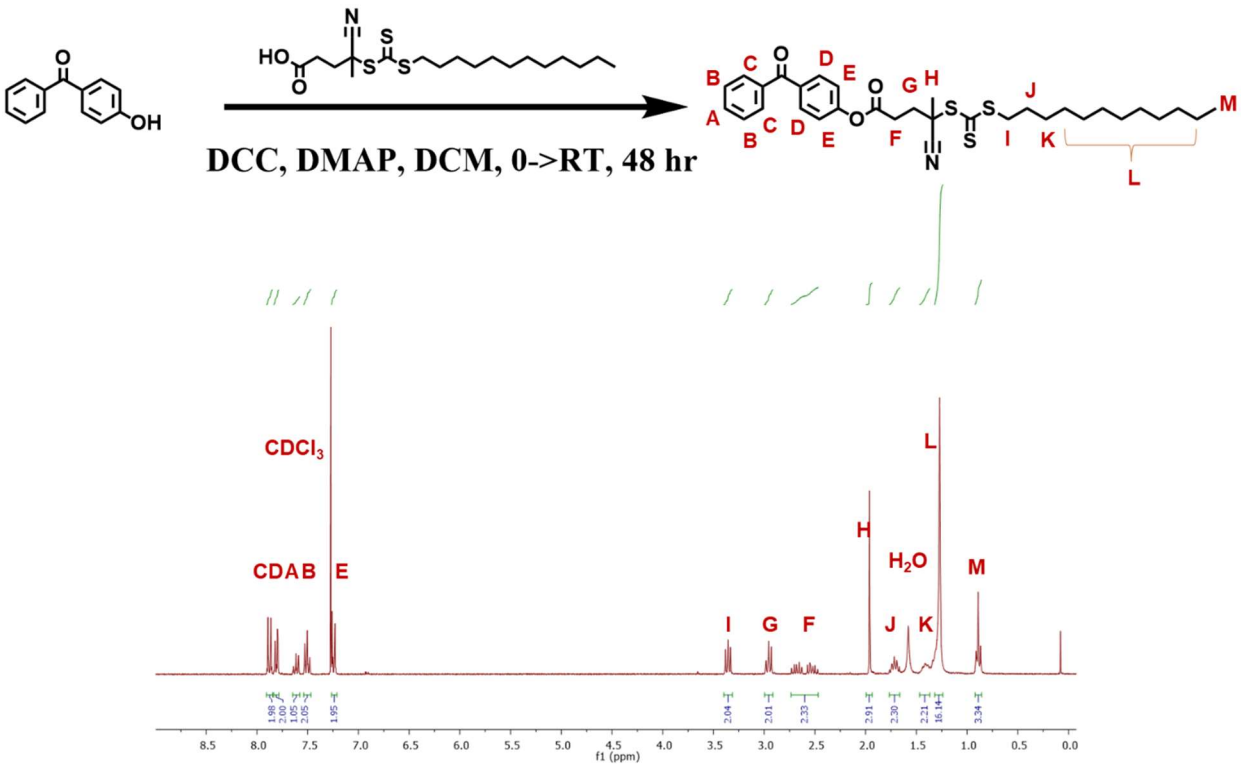

Figure 4.S2: Synthesis of benz-CTA. (A) Chemical scheme of benz-CTA synthesis. (B) NMR of benz-CTA.

CHAPTER 5: NONDESTRUCTIVE CHARACTERIZATION OF PCL NANOFIBERS

5.1 Abstract: Polymeric nanofibers increase molecular order upon uniaxial drawing. Typical methods to monitor this change in order involve destructive techniques incompatible with biological systems. Polarized light microscopy shows a correlation between traditional physical, mechanical, and thermal polymer characterization techniques and the color response of nanophoonic metasurfaces based on the molecular order of polymeric nanofibers.

5.2 Introduction: In addition to utilizing polymeric nanofibers as functional mats, they also display a unique elastomeric ability and can reach more than 700% elongation before experiencing a loss of structural integrity. The uniaxial drawing of polymeric nanofibers has been shown to have a direct impact on the mechanical and thermal properties of materials, which in turn has shown secondary effects such as leading to a decrease in modification density as the polymeric nanofibers reach higher draw ratios.[97] This leads to the question of what other secondary effects occur due to the uniaxial alignment of the polymeric nanofibers via mechanical drawing.

Polarized light microscopy is an imaging technique that analyzes the local anisotropy of a sample's optical properties including absorption and refraction, where dichroism and birefringence can be investigated. These properties display characteristic intensity variations as they are rotated between crossed linear polarizing filters, which are a consequence of molecular order.[106]

As polarized light microscopy can study molecular order, it is theorized that the chain alignment known to occur from the uniaxial drawing of polymeric nanofibers can be analyzed via polarized light microscopy. Polarized light microscopy has the unique ability to characterize nanofiber mats based on the degree of molecular alignment of the polymer chains, similarly to traditional mechanical and thermal polymer characterization methods, but in a nondestructive

manner. It is therefore possible to correlate data obtained from polarized light microscopy to the physical, mechanical and thermal properties of polymeric nanofibers. This nondestructive nature of allows for a significantly wider array of uses than the typical methods, such as in biological systems.

5.3 Methods

5.3.1 Nanofiber Drawing: Nanofibers were isolated from their composite tapes by washing in a water bath with the water replaced every hour for 6 hours, before being left in a 70% MeOH solution overnight. Once dried, isolated nanofibers were clamped onto an Instron tensile testing instrument with a 100 N load cell, and uniaxially elongated at 10 mm min^{-1} to the desired length. Draw ratios (DR) 1-10 were prepared, with DR1 having 0% elongation, and each subsequent DR increasing the elongation by 100% (e.g., DR5 = 400% elongation).

5.3.2 Differential Scanning Calorimetry: Drawn nanofibers were cut and placed into a hermetically sealed aluminum pan, completely covering the bottom. Samples were then placed in a differential scanning calorimeter (DSC) along with an empty pan as a baseline to assess their crystallinity. A starting temperature of 25 °C was used, increasing at a rate of 10 °C min^{-1} and heated to 200 °C, then held for 5 minutes before being cooled to -25 °C at a rate of -10 °C min^{-1}. Samples were held at -25 °C for 5 minutes then increased back to 25 °C, where the experiment concluded. Crystallinity was determined by comparing the ΔH of each sample with the literature value of 135.4 J g^{-1} for crystalline PCL.

5.3.3 Tensile Testing: The thickness and width of the nanofibers were measured with a caliper before the samples were clamped into an Instron tensile tester with a 100 N load cell. Once clamped, the length of nanofiber between the clamps was measured. Drawn nanofibers were then pulled at a constant rate of 10 mm min^{-1} until the sample failed. The cross-sectional surface area

was calculated by multiplying the width and thickness. The stress (MPa) was then calculated by dividing the force at each data point by the cross-sectional surface area of the nanofibers. The strain was determined by dividing the displacement at each data point by the initial length of the nanofibers. A stress versus strain curve is then plotted from the data, with elastic modulus being the slope of the initial linear region.

5.4 Results and Discussion

5.4.1 Nanofiber Drawing: Following nanofiber isolation, nanofibers were clamped on both ends to a tensile testing instrument and drawn to desired draw ratios (DR). As the draw ratio increases the polymer chains are increasing molecular alignment, thus increasing the crystallinity of the samples. Each increase in draw ratio implies a 100% increase in sample length. Starting at DR1 (0% increase), samples were drawn to DR2 (100% length increase), DR3 (200% length increase), DR4 (300% length increase), DR5 (400% length increase), DR6 (500% length increase), DR7 (600% length increase), DR8 (700% length increase), DR9 (800% length increase), and DR10 (900% length increase). Samples were observed to lose mechanical integrity during drawing beginning at DR7.

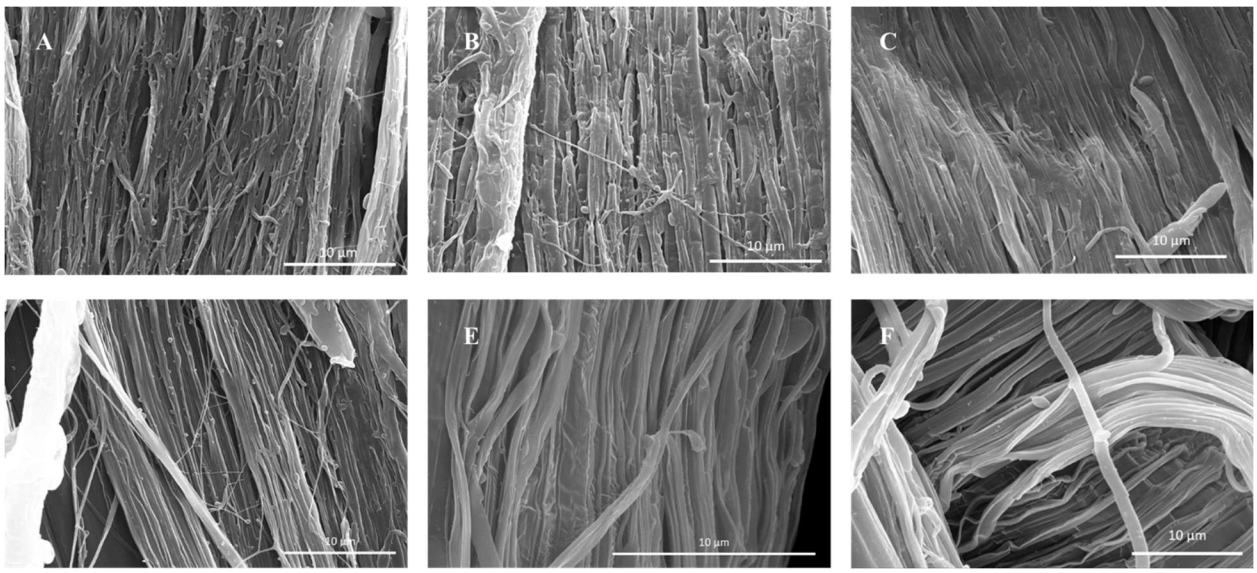

Figure 5.1: Scanning electron micrographs of (A) DR1, (B) DR2, (C) DR4, (D) DR6, (E) DR8, and (F) DR10. (Scale bar = 10 µm).

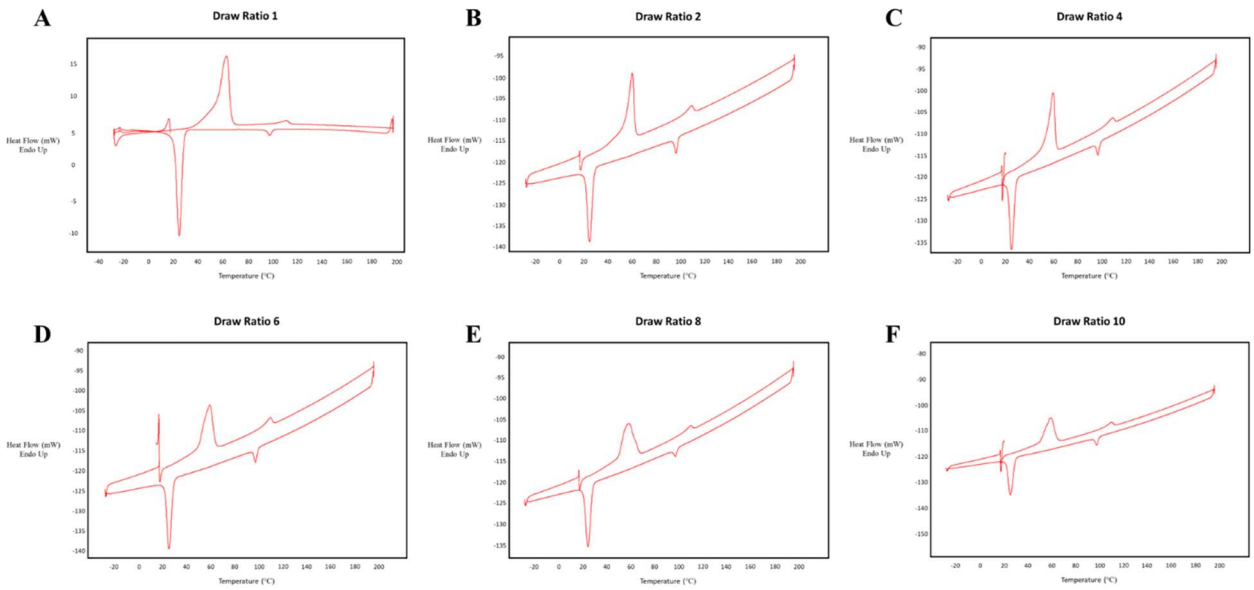

Figure 5.2: Differential scanning calorimetry of (A) DR1, (B) DR2, (C) DR4, (D) DR6, (E) DR8, and (F) DR10.

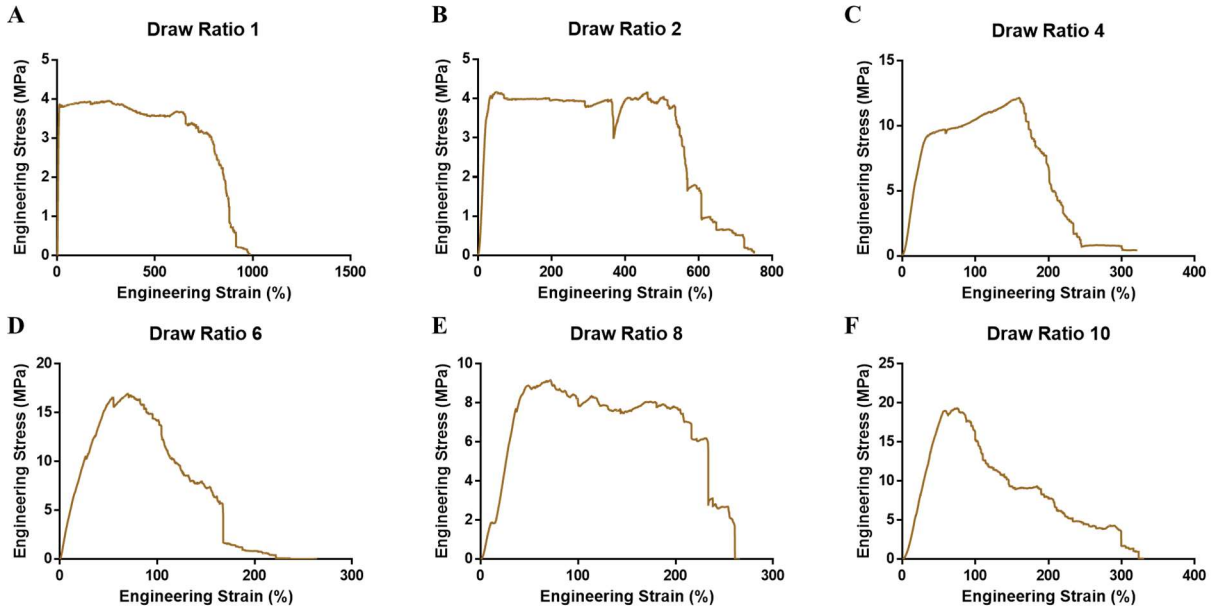

Figure 5.3: Stress-Strain plots of (A) DR1, (B) DR2, (C) DR4, (D) DR6, (E) DR8, and (F) DR10.

5.4.2 Traditional Polymer Characterization: Nanofibers with DRs of DR1, DR2, DR4, DR6, DR8, and DR10 were characterized by SEM (**Figure 5.1**), DSC (**Figure 5.2**), and tensile testing (**Figure 5.3**). The relevant data is summarized in **Table 5.1**.

SEM allows for the determination of width and thickness of the fibers. The width and thickness of each DR are as follows: DR1 (411.3 ± 91.1 by 233.1 ± 50.2 nm), DR2 (401.5 ± 63.4 by 218.9

Table 5.1: Summary of mechanical and thermal data including elastic moduli, fiber dimensions (width and thickness), nanofiber crystallinity, and melting point.

Sample	Fiber Width (nm)	Fiber Thickness (nm)	Percent Crystallinity	Melting Point (°C)	Elastic Moduli (MPa)
DR1	411.3 ± 91.1	233.1 ± 50.2	30.1	62.94	33.2 ± 11.9
DR2	401.5 ± 63.4	218.9 ± 49.5	30.8	60.60	11.6 ± 3.5
DR4	376.1 ± 82.2	214.3 ± 43.8	31.5	59.97	13.8 ± 1.2
DR6	337.8 ± 103.9	176.7 ± 45.4	35.7	58.88	18.1 ± 2.4
DR8	250.5 ± 40.4	126.8 ± 42.0	30.7	57.61	26.0 ± 7.8
DR10	189.1 ± 17.3	105.6 ± 25.8	29.7	58.88	37.8 ± 6.3

± 49.5 nm), DR4 (376.1 ± 82.2 by 214.3 ± 43.8 nm), DR6 (337.8 ± 103.9 by 176.7 ± 45.4 nm), DR8 (250.5 ± 40.4 by 126.8 ± 42.0 nm), and DR10 (189.1 ± 17.3 by 105.6 ± 25.8 nm). These results indicate that as the nanofibers are drawn, they become thinner.

DSC provides a percent crystallinity based on the enthalpy (ΔH) of a sample as well as its melting point. Compared to the physical dimensions of the nanofibers, the percent crystallinity and melting point follow a pattern until DR8: DR1 (30.1% crystalline, 62.94 °C), DR2 (30.8% crystalline, 60.60 °C), DR4 (31.5% crystalline, 59.97 °C), DR6 (35.7% crystalline, 58.88 °C), DR8 (30.7% crystalline, 57.61 °C), and DR10 (29.7% crystalline, 58.88 °C). As nanofibers begin losing their integrity at DR7, these deviations from the trend are associated with the physical breakdown of said fibers.

The mechanical properties of nanofibers also change upon drawing: DR1 (33.2 ± 11.9 MPa), DR2 (11.6 ± 3.5 MPa), DR4 (13.8 ± 1.2 MPa), DR6 (18.1 ± 2.4 MPa), DR8 (26.0 ± 7.8 MPa), and

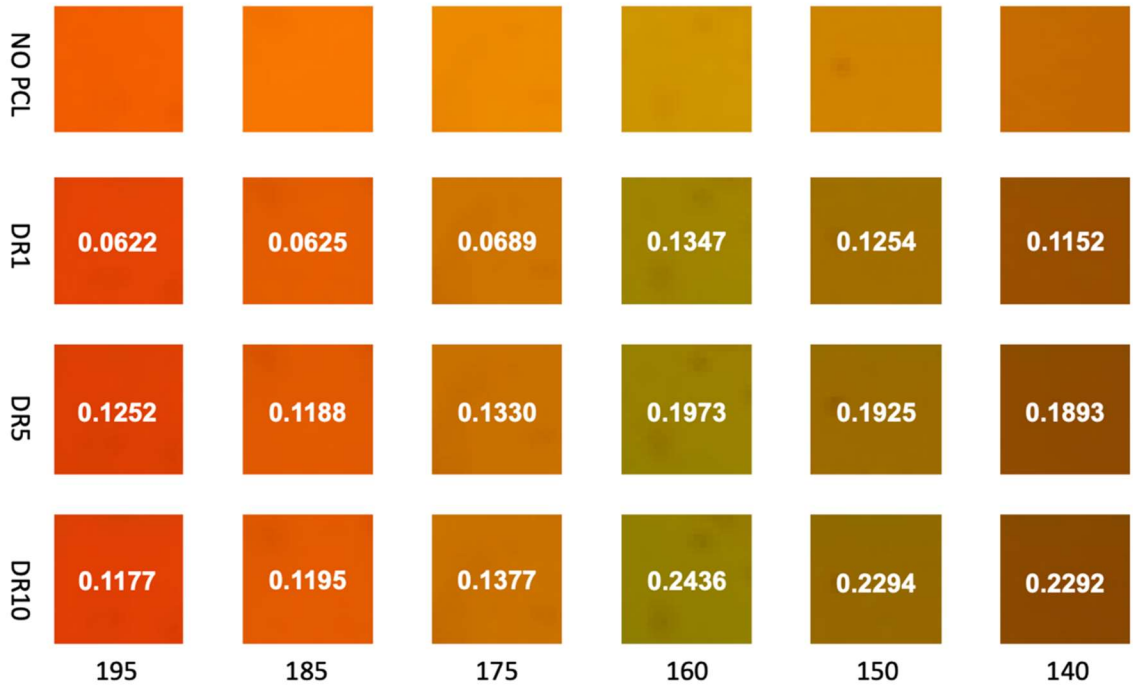

Figure 5.4: Color response of nanophotnic metasurfaces with average color discrimination overlaid on top of each metasurface.

DR10 (37.8 ± 6.3 MPa). After an initial loosening of the chains, the elastic modulus significantly increases as the DR increases, indicating a large increase of tensile strength.

5.4.3 Nanophotonic Metasurfaces: Nanophotonic metasurfaces are planar, sub-wavelength structures that dictate properties of incident light including amplitude, phase, and polarization.[107] **Figure 5.4** shows the photonic response utilizing nanophotonic metasurfaces based on the molecular order of PCL nanofibers. This color discrimination chart shows that as the DR increases and the polymeric nanofibers become more ordered via molecular alignment, the color discrimination significantly increases. This increase in color discrimination indicates a correlation between polarized light microscopy-based data and traditional polymer characterization techniques.

5.5 Conclusion: Drawn polymeric nanofibers were used to correlate traditional polymer characterization methods to the color response of nanophotonic metasurfaces obtained with polarized light microscopy. The color responses showed a relationship with an increase in

molecular order, which is traditionally shown by characterization methods including SEM, DSC, and tensile testing. This new relationship has the potential to be used in vivo while actively monitoring conditions in tissue engineering applications.

5.6 Acknowledgements: The Poulikakos Lab is acknowledged for contributing their work in nanophotonic metasurfaces to this project.

Chapter 5 contains unpublished material coauthored with Kirya, P.; Bordy, S.; Poulikakos, L.; and Pokorski J. The dissertation author was the primary author of this chapter.

CONCLUSION OF THE DISSERTATION

This dissertation described the successful functionalization of PCL nanofiber materials with functional polymers with surface initiated ATRP and PET-RAFT techniques. Utilizing this technology, nanofiber mats were developed that possessed strong antibacterial properties, efficiently eliminating both Gram-positive and Gram-negative bacteria including *E. coli* and *MRSA*, the latter of which is also antibiotic resistant. These antibacterial nanofiber mats showed sufficient biocompatibility no different from control materials and was significantly more effective than grafting-to counterpart materials.

To complement the antibacterial materials and enter the realm of multifunctional wound healing materials, blood clot enhancing functionalities were also imparted on the nanofiber mats via SI-ATRP. These materials were effective at reducing the time required for clots to form, increasing the diameter of the fibrin fibers that make up blood clots, and increasing the concentration of thrombin produced during the coagulation cascade.

Surface initiated PET-RAFT chemistry was then used to expand the functionalization capabilities of the nanofibers. A library of various monomers was first polymerized off the nanofiber surface with PET-RAFT to show the viability of the technique. Following these initial fabrications, more complex experiments were conducted with this chemistry. It was shown that these materials could be functionalized with block copolymers and orthogonal chemistries. Both showing that two different monomer units could be polymerized off the surface at different times, but by two distinct methods. UV photopatterning was also employed with fluorescent moieties to show the spatial patterning capabilities of this technology. This patterning then led to the development of nanofiber mats functionalized with a cell adhering GRGDS acrylate monomer.

This monomer allowed for the adherence of mouse fibroblasts to the surface of the nanofibers in significantly larger numbers than both unmodified and antifouling nanofiber mats.

Future directions of this work lead in many interesting directions. The first of which is a multifunctional mat with broad spectrum antimicrobial properties incorporating antibacterial, antiviral, and antifungal elements. There is a wide range of literature discussing antiviral moieties that can be included in polymeric systems. These include those affective against viruses such as adenoviruses,[108] coronaviruses,[109] HIV,[110,111] herpesviruses,[110–112] and varicella.[112] Similarly, a variety of effective antifungal polymers are known as well.[113–115] In addition to the activity of the mats being important, the immune response of the individual is extremely important as well. Manipulation of the immune system's response to foreign elements can help either mask[116] or magnify[117] the material's presence, which can be useful in tailoring the immune response to best assist in preventing infection and preventing bleed out.

These multifunctional mats can serve a wide variety of applications such multidimensional wound treatment devices as well as to serve as respirators to prevent infection. Commonly worn respirators include N95s, which prevent more than 95% of particles 75 nm or larger from passing through.[118] These N95 respirators are produced via the melt blowing polypropylene fibers to form nonwoven fabrics.[119] Incorporating multifunctional antimicrobial moieties to nonwoven nanofiber respirators has the ability to significantly improve the effectiveness of polymer fiber based respirators as well as preventing accidental exposure from improper handling of contaminated respirators.

Another direction for the further development of this technology delves into the tissue engineering realm, whereby mesenchymal stem cells (MSC) can differentiate into a variety of different cells with a mechanical stimulus. Depending on the mechanical force applied, MSCs can

differentiate into neurocytes (brain), beta cells (pancreas), chondrocytes (cartilage), myoblasts (muscle), and osteoblasts (bone) as matrix stiffness increases.[105,120] As coextruded PCL nanofibers have been previously shown to be extremely elastic, they can reach up to 700% elongation, which increases their elastic modulus and the nanofibers extend.[97] The combination of this drawing ability with the concept of mechanically derived differentiation naturally leads to the development of nanofibers functionalized with the GRGDS acrylate moiety, which was shown to significantly increase cellular adhesion to the nanofibers. These combined ideas have the potential to form synthetic tissues derived from the PCL nanofibers, which are capable of dynamic MSC differentiation when drawn to high elongation with adhered MSCs experiencing a mechanical force.

While pre-drawing nanofibers is simple and just requires a tensile testing instrument, dynamic drawing in vitro requires the design of special equipment whereby a consistent mechanical force can be applied to a sample while being in an environment conducive to cell growth. This would make characterization via traditional thermal, physical, and mechanical properties extremely difficult. Utilizing polarized light microscopy-based techniques that makes use of the color discrimination of nanophotonic metasurfaces allows for the nondestructive characterization of nanofiber alignment with cells adhered, whereby the traditional techniques such as DSC, SEM, and tensile testing would not be possible in vitro.

Melt coextrusion of PCL nanofibers and subsequent functionalization has led to the development of functional nanofiber mats. These functional nanofiber mats exhibit antibacterial and blood clot enhancing capabilities and have been manipulated with different chemistries to allow for a wide variety of complex functionalities, as well the formation of spatially patterned

materials. These materials show extreme promise in the future of biomedicine, and the potential to improve and save many lives.

REFERENCES

(1) Valente, T. A. M.; Silva, D. M.; Gomes, P. S.; Fernandes, M. H.; Santos, J. D.; Sencadas, V. Effect of Sterilization Methods on Electrospun Poly(Lactic Acid) (PLA) Fiber Alignment for Biomedical Applications. *ACS Appl. Mater. Interfaces* **2016**, *8* (5), 3241–3249. https://doi.org/10.1021/acsami.5b10869.

(2) Diao, H. J.; Wang, K.; Long, H. Y.; Wang, M.; Chew, S. Y. Highly Fluorescent and Photostable Polymeric Nanofibers as Scaffolds for Cell Interfacing and Long-Term Tracking. *Adv. Healthc. Mater.* **2016**, *5* (5), 529–533. https://doi.org/10.1002/adhm.201500693.

(3) Nagiah, N.; Johnson, R.; Anderson, R.; Elliott, W.; Tan, W. Highly Compliant Vascular Grafts with Gelatin-Sheathed Coaxially Structured Nanofibers. *Langmuir* **2015**, *31* (47), 12993–13002. https://doi.org/10.1021/acs.langmuir.5b03177.

(4) Jordan, A. M.; Viswanath, V.; Kim, S.-E.; Pokorski, J. K.; Korley, L. T. J. Processing and Surface Modification of Polymer Nanofibers for Biological Scaffolds: A Review. *J. Mater. Chem. B* **2016**, *4* (36), 5958–5974. https://doi.org/10.1039/C6TB01303A.

(5) Hochberg, J. D.; Wirth, D. M.; Spiaggia, G.; Shah, P.; Rothen-Rutishauser, B.; Petri-Fink, A.; Pokorski, J. K. High-Throughput Manufacturing of Antibacterial Nanofibers by Melt Coextrusion and Post-Processing Surface-Initiated Atom Transfer Radical Polymerization. *ACS Appl. Polym. Mater.* **2022**, *4* (1), 260–269. https://doi.org/10.1021/acsapm.1c01264.

(6) Agarwal, S.; Wendorff, J. H.; Greiner, A. Use of Electrospinning Technique for Biomedical Applications. *Polymer* **2008**, *49* (26), 5603–5621. https://doi.org/10.1016/j.polymer.2008.09.014.

(7) Smith Callahan, L. A.; Xie, S.; Barker, I. A.; Zheng, J.; Reneker, D. H.; Dove, A. P.; Becker, M. L. Directed Differentiation and Neurite Extension of Mouse Embryonic Stem Cell on Aligned Poly(Lactide) Nanofibers Functionalized with YIGSR Peptide. *Biomaterials* **2013**, *34* (36), 9089–9095. https://doi.org/10.1016/j.biomaterials.2013.08.028.

(8) Camerlo, A.; Bühlmann-Popa, Ana.-M.; Vebert-Nardin, C.; Rossi, R. M.; Fortunato, G. Environmentally Controlled Emulsion Electrospinning for the Encapsulation of Temperature-Sensitive Compounds. *J. Mater. Sci.* **2014**, *49* (23), 8154–8162. https://doi.org/10.1007/s10853-014-8524-5.

(9) Wang, N.; Burugapalli, K.; Song, W.; Halls, J.; Moussy, F.; Zheng, Y.; Ma, Y.; Wu, Z.; Li, K. Tailored Fibro-Porous Structure of Electrospun Polyurethane Membranes, Their Size-Dependent Properties and Trans-Membrane Glucose Diffusion. *J. Membr. Sci.* **2013**, *427*, 207–217. https://doi.org/10.1016/j.memsci.2012.09.052.

(10) Esmaeilzadeh, I.; Mottaghitalab, V.; Tousifar, B.; Afzali, A.; Lamani, M. A Feasibility Study on Semi Industrial Nozzleless Electrospinning of Cellulose Nanofiber. *Int. J. Ind. Chem.* **2015**, *6* (3), 193–211. https://doi.org/10.1007/s40090-015-0043-y.

(11) Chen, F.; Hochleitner, G.; Woodfield, T.; Groll, J.; Dalton, P. D.; Amsden, B. G. Additive Manufacturing of a Photo-Cross-Linkable Polymer via Direct Melt Electrospinning Writing for Producing High Strength Structures. *Biomacromolecules* **2016**, *17* (1), 208–214. https://doi.org/10.1021/acs.biomac.5b01316.

(12) Badrossamay, M. R.; McIlwee, H. A.; Goss, J. A.; Parker, K. K. Nanofiber Assembly by Rotary Jet-Spinning. *Nano Lett.* **2010**, *10* (6), 2257–2261. https://doi.org/10.1021/nl101355x.
(13) Badrossamay, M. R.; Balachandran, K.; Capulli, A. K.; Golecki, H. M.; Agarwal, A.; Goss, J. A.; Kim, H.; Shin, K.; Parker, K. K. Engineering Hybrid Polymer-Protein Super-Aligned Nanofibers via Rotary Jet Spinning. *Biomaterials* **2014**, *35* (10), 3188–3197. https://doi.org/10.1016/j.biomaterials.2013.12.072.
(14) Zuo, F.; Tan, D. H.; Wang, Z.; Jeung, S.; Macosko, C. W.; Bates, F. S. Nanofibers from Melt Blown Fiber-in-Fiber Polymer Blends. *ACS Macro Lett.* **2013**, *2* (4), 301–305. https://doi.org/10.1021/mz400053n.
(15) Wang, J.; Langhe, D.; Ponting, M.; Wnek, G. E.; Korley, L. T. J.; Baer, E. Manufacturing of Polymer Continuous Nanofibers Using a Novel Co-Extrusion and Multiplication Technique. *Polymer* **2014**, *55* (2), 673–685. https://doi.org/10.1016/j.polymer.2013.12.025.
(16) Kim, S.-E.; Jordan, A. M.; Korley, L. T. J.; Pokorski, J. K. Drawing in Poly(ε-Caprolactone) Fibers: Tuning Mechanics, Fiber Dimensions and Surface-Modification Density. *J. Mater. Chem. B* **2017**, *5* (23), 4499–4506. https://doi.org/10.1039/C7TB00096K.
(17) Kim, S.-E.; Wang, J.; Jordan, A. M.; Korley, L. T. J.; Baer, E.; Pokorski, J. K. Surface Modification of Melt Extruded Poly(ε-Caprolactone) Nanofibers: Toward a New Scalable Biomaterial Scaffold. *ACS Macro Lett.* **2014**, *3* (6), 585–589. https://doi.org/10.1021/mz500112d.
(18) Wang, J.; Ponting, M.; Zhang, C.; Olah, A.; Baer, E. Fuel Filtration Properties and Mechanism of a Novel Fibrous Filter Produced by a Melt-Process. *J. Membr. Sci.* **2017**, *526*, 229–241. https://doi.org/10.1016/j.memsci.2016.12.040.
(19) Kim, S.-E.; Wallat, J. D.; Harker, E. C.; Advincula, A. A.; Pokorski, J. K. Multifunctional and Spatially Controlled Bioconjugation to Melt Coextruded Nanofibers. *Polym. Chem.* **2015**, *6* (31), 5683–5692. https://doi.org/10.1039/C5PY00282F.
(20) Kim, S.-E.; Harker, E. C.; De Leon, A. C.; Advincula, R. C.; Pokorski, J. K. Coextruded, Aligned, and Gradient-Modified Poly(ε-Caprolactone) Fibers as Platforms for Neural Growth. *Biomacromolecules* **2015**, *16* (3), 860–867. https://doi.org/10.1021/bm501767x.
(21) Ng, I. C.; Pawijit, P.; Tan, J.; Yu, H. Anatomy and Physiology for Biomaterials Research and Development. In *Encyclopedia of Biomedical Engineering*; Elsevier, 2019; pp 225–236. https://doi.org/10.1016/B978-0-12-801238-3.99876-3.
(22) Cortizo, M. S.; Molinuevo, M. S.; Cortizo, A. M. Biocompatibility and Biodegradation of Polyester and Polyfumarate Based-Scaffolds for Bone Tissue Engineering. *J. Tissue Eng. Regen. Med.* **2008**, *2* (1), 33–42. https://doi.org/10.1002/term.62.
(23) Nair, L. S.; Laurencin, C. T. Biodegradable Polymers as Biomaterials. *Prog. Polym. Sci.* **2007**, *32* (8–9), 762–798. https://doi.org/10.1016/j.progpolymsci.2007.05.017.
(24) Gunatillake, P.; Mayadunne, R.; Adhikari, R. Recent Developments in Biodegradable Synthetic Polymers. In *Biotechnology Annual Review*; Elsevier, 2006; Vol. 12, pp 301–347. https://doi.org/10.1016/S1387-2656(06)12009-8.
(25) Dhandayuthapani, B.; Yoshida, Y.; Maekawa, T.; Kumar, D. S. Polymeric Scaffolds in Tissue Engineering Application: A Review. *Int. J. Polym. Sci.* **2011**, *2011*, 1–19. https://doi.org/10.1155/2011/290602.

(26) Bendrea, A.-D.; Cianga, L.; Ailiesei, G.-L.; Ursu, E.-L.; Göen Colak, D.; Cianga, I. 3,4-Ethylenedioxythiophene (EDOT) End-Group Functionalized Poly-ε-Caprolactone (PCL): Self-Assembly in Organic Solvents and Its Coincidentally Observed Peculiar Behavior in Thin Film and Protonated Media. *Polymers* **2021**, *13* (16), 2720. https://doi.org/10.3390/polym13162720.
(27) Zhu, Y.; Gao, C.; Liu, X.; Shen, J. Surface Modification of Polycaprolactone Membrane via Aminolysis and Biomacromolecule Immobilization for Promoting Cytocompatibility of Human Endothelial Cells. *Biomacromolecules* **2002**, *3* (6), 1312–1319. https://doi.org/10.1021/bm020074y.
(28) Sun, H.; Önneby, S. Facile Polyester Surface Functionalization via Hydrolysis and Cell-Recognizing Peptide Attachment. *Polym. Int.* **2006**, *55* (11), 1336–1340. https://doi.org/10.1002/pi.2090.
(29) Kósa, C.; Sedlačík, M.; Fiedlerová, A.; Chmela, Š.; Borská, K.; Mosnáček, J. Photochemically Cross-Linked Poly(ε-Caprolactone) with Accelerated Hydrolytic Degradation. *Eur. Polym. J.* **2015**, *68*, 601–608. https://doi.org/10.1016/j.eurpolymj.2015.03.041.
(30) Kim, S.-E.; Zhang, C.; Advincula, A. A.; Baer, E.; Pokorski, J. K. Protein and Bacterial Antifouling Behavior of Melt-Coextruded Nanofiber Mats. *ACS Appl. Mater. Interfaces* **2016**, *8* (14), 8928–8938. https://doi.org/10.1021/acsami.6b00093.
(31) Rubio, N.; Au, H.; Leese, H. S.; Hu, S.; Clancy, A. J.; Shaffer, M. S. P. Grafting from versus Grafting to Approaches for the Functionalization of Graphene Nanoplatelets with Poly(Methyl Methacrylate). *Macromolecules* **2017**, *50* (18), 7070–7079. https://doi.org/10.1021/acs.macromol.7b01047.
(32) Centers for Disease Control and Prevention (U.S.). *Antibiotic Resistance Threats in the United States, 2019*; Centers for Disease Control and Prevention (U.S.), 2019. https://doi.org/10.15620/cdc:82532.
(33) DiNubile, M. J. Complicated Infections of Skin and Skin Structures: When the Infection Is More than Skin Deep. *J. Antimicrob. Chemother.* **2004**, *53* (suppl_2), ii37–ii50. https://doi.org/10.1093/jac/dkh202.
(34) Vinh, D. C.; Embil, J. M. Rapidly Progressive Soft Tissue Infections. *Lancet Infect. Dis.* **2005**, *5* (8), 501–513. https://doi.org/doi:10.1016/s1473-3099(05)70191-2.
(35) Sukumaran, V.; Senanayake, S. Bacterial Skin and Soft Tissue Infections. *Aust. Prescr.* **2016**, *39* (5), 159–163. https://doi.org/10.18773/austprescr.2016.058.
(36) Kurtz, I.; Schiffman, J. Current and Emerging Approaches to Engineer Antibacterial and Antifouling Electrospun Nanofibers. *Materials* **2018**, *11* (7), 1059. https://doi.org/10.3390/ma11071059.
(37) Rieger, K. A.; Cho, H. J.; Yeung, H. F.; Fan, W.; Schiffman, J. D. Antimicrobial Activity of Silver Ions Released from Zeolites Immobilized on Cellulose Nanofiber Mats. *ACS Appl. Mater. Interfaces* **2016**, *8* (5), 3032–3040. https://doi.org/10.1021/acsami.5b10130.
(38) Rieger, K. A.; Schiffman, J. D. Electrospinning an Essential Oil: Cinnamaldehyde Enhances the Antimicrobial Efficacy of Chitosan/Poly(Ethylene Oxide) Nanofibers. *Carbohydr. Polym.* **2014**, *113*, 561–568. https://doi.org/10.1016/j.carbpol.2014.06.075.
(39) Ignatova, M.; Manolova, N.; Markova, N.; Rashkov, I. Electrospun Non-Woven Nanofibrous Hybrid Mats Based on Chitosan and PLA for Wound-Dressing Applications. *Macromol. Biosci.* **2009**, *9* (1), 102–111. https://doi.org/10.1002/mabi.200800189.

(40) Kayaci, F.; Umu, O. C. O.; Tekinay, T.; Uyar, T. Antibacterial Electrospun Poly(Lactic Acid) (PLA) Nanofibrous Webs Incorporating Triclosan/Cyclodextrin Inclusion Complexes. *J. Agric. Food Chem.* **2013**, *61* (16), 3901–3908. https://doi.org/10.1021/jf400440b.
(41) Nguyen, T.-H.; Kim, Y.-H.; Song, H.-Y.; Lee, B.-T. Nano Ag Loaded PVA Nano-Fibrous Mats for Skin Applications. *J. Biomed. Mater. Res. B Appl. Biomater.* **2011**, *96B* (2), 225–233. https://doi.org/10.1002/jbm.b.31756.
(42) Schiffman, J. D.; Wang, Y.; Giannelis, E. P.; Elimelech, M. Biocidal Activity of Plasma Modified Electrospun Polysulfone Mats Functionalized with Polyethyleneimine-Capped Silver Nanoparticles. *Langmuir* **2011**, *27* (21), 13159–13164. https://doi.org/10.1021/la202605z.
(43) Lin, N.; Berton, P.; Moraes, C.; Rogers, R. D.; Tufenkji, N. Nanodarts, Nanoblades, and Nanospikes: Mechano-Bactericidal Nanostructures and Where to Find Them. *Adv. Colloid Interface Sci.* **2018**, *252*, 55–68. https://doi.org/10.1016/j.cis.2017.12.007.
(44) Schiffman, J. D.; Elimelech, M. Antibacterial Activity of Electrospun Polymer Mats with Incorporated Narrow Diameter Single-Walled Carbon Nanotubes. *ACS Appl. Mater. Interfaces* **2011**, *3* (2), 462–468. https://doi.org/10.1021/am101043y.
(45) Zasloff, M. Antimicrobial Peptides of Multicellular Organisms. *Nature* **2002**, *415* (6870), 389–395. https://doi.org/10.1038/415389a.
(46) Yeaman, M. R.; Yount, N. Y. Mechanisms of Antimicrobial Peptide Action and Resistance. *Pharmacol. Rev.* **2003**, *55* (1), 27–55. https://doi.org/10.1124/pr.55.1.2.
(47) Brogden, K. A. Antimicrobial Peptides: Pore Formers or Metabolic Inhibitors in Bacteria? *Nat. Rev. Microbiol.* **2005**, *3* (3), 238–250. https://doi.org/10.1038/nrmicro1098.
(48) Paslay, L. C.; Abel, B. A.; Brown, T. D.; Koul, V.; Choudhary, V.; McCormick, C. L.; Morgan, S. E. Antimicrobial Poly(Methacrylamide) Derivatives Prepared via Aqueous RAFT Polymerization Exhibit Biocidal Efficiency Dependent upon Cation Structure. *Biomacromolecules* **2012**, *13* (8), 2472–2482. https://doi.org/10.1021/bm3007083.
(49) Teuber, M.; Bader, J. Action of Polymyxin B on Bacterial Membranes. *Arch Microbiol* **1976**, *109*, 8.
(50) Parandhaman, T.; Choudhary, P.; Ramalingam, B.; Schmidt, M.; Janardhanam, S.; Das, S. K. Antibacterial and Antibiofouling Activities of Antimicrobial Peptide-Functionalized Graphene–Silver Nanocomposites for the Inhibition and Disruption of *Staphylococcus Aureus* Biofilms. *ACS Biomater. Sci. Eng.* **2021**, acsbiomaterials.1c01253. https://doi.org/10.1021/acsbiomaterials.1c01253.
(51) Wuersching, S. N.; Huth, K. C.; Hickel, R.; Kollmuss, M. Inhibitory Effect of LL-37 and Human Lactoferricin on Growth and Biofilm Formation of Anaerobes Associated with Oral Diseases. *Anaerobe* **2021**, *67*, 102301. https://doi.org/10.1016/j.anaerobe.2020.102301.
(52) Kumar, A.; Boyer, C.; Nebhani, L.; Wong, E. H. H. Highly Bactericidal Macroporous Antimicrobial Polymeric Gel for Point-of-Use Water Disinfection. *Sci. Rep.* **2018**, *8* (1), 7965. https://doi.org/10.1038/s41598-018-26202-0.
(53) Zuo, H.; Wu, D.; Fu, R. Synthesis of Antibacterial Polymers from 2-Dimethylamino Ethyl Methacrylate Quaternized by Dimethyl Sulfate. *Polym. J.* **2010**, *42* (9), 766–771. https://doi.org/10.1038/pj.2010.63.
(54) Cuthbert, T. J.; Hisey, B.; Harrison, T. D.; Trant, J. F.; Gillies, E. R.; Ragogna, P. J. Surprising Antibacterial Activity and Selectivity of Hydrophilic Polyphosphoniums

Featuring Sugar and Hydroxy Substituents. *Angew. Chem. Int. Ed.* **2018**, *57* (39), 12707–12710. https://doi.org/10.1002/anie.201806412.

(55) Judzewitsch, P. R.; Corrigan, N.; Trujillo, F.; Xu, J.; Moad, G.; Hawker, C. J.; Wong, E. H. H.; Boyer, C. High-Throughput Process for the Discovery of Antimicrobial Polymers and Their Upscaled Production via Flow Polymerization. *Macromolecules* **2020**, *53* (2), 631–639. https://doi.org/10.1021/acs.macromol.9b02207.

(56) Cannon, J. W. Hemorrhagic Shock. *N. Engl. J. Med.* **2018**, *378* (4), 370–379. https://doi.org/10.1056/NEJMra1705649.

(57) Lozano, R.; Naghavi, M.; Foreman, K.; Lim, S.; Shibuya, K.; Aboyans, V.; Abraham, J.; Adair, T.; Aggarwal, R.; Ahn, S. Y.; AlMazroa, M. A.; Alvarado, M.; Anderson, H. R.; Anderson, L. M.; Andrews, K. G.; Atkinson, C.; Baddour, L. M.; Barker-Collo, S.; Bartels, D. H.; Bell, M. L.; Benjamin, E. J.; Bennett, D.; Bhalla, K.; Bikbov, B.; Abdulhak, A. B.; Birbeck, G.; Blyth, F.; Bolliger, I.; Boufous, S.; Bucello, C.; Burch, M.; Burney, P.; Carapetis, J.; Chen, H.; Chou, D.; Chugh, S. S.; Coffeng, L. E.; Colan, S. D.; Colquhoun, S.; Colson, K. E.; Condon, J.; Connor, M. D.; Cooper, L. T.; Corriere, M.; Cortinovis, M.; de Vaccaro, K. C.; Couser, W.; Cowie, B. C.; Criqui, M. H.; Cross, M.; Dabhadkar, K. C.; Dahodwala, N.; De Leo, D.; Degenhardt, L.; Delossantos, A.; Denenberg, J.; Des Jarlais, D. C.; Dharmaratne, S. D.; Dorsey, E. R.; Driscoll, T.; Duber, H.; Ebel, B.; Erwin, P. J.; Espindola, P.; Ezzati, M.; Feigin, V.; Flaxman, A. D.; Forouzanfar, M. H.; Fowkes, F. G. R.; Franklin, R.; Fransen, M.; Freeman, M. K.; Gabriel, S. E.; Gakidou, E.; Gaspari, F.; Gillum, R. F.; Gonzalez-Medina, D.; Halasa, Y. A.; Haring, D.; Harrison, J. E.; Havmoeller, R.; Hay, R. J.; Hoen, B.; Hotez, P. J.; Hoy, D.; Jacobsen, K. H.; James, S. L.; Jasrasaria, R.; Jayaraman, S.; Johns, N.; Karthikeyan, G.; Kassebaum, N.; Keren, A.; Khoo, J.-P.; Knowlton, L. M.; Kobusingye, O.; Koranteng, A.; Krishnamurthi, R.; Lipnick, M.; Lipshultz, S. E.; Ohno, S. L.; Mabweijano, J.; MacIntyre, M. F.; Mallinger, L.; March, L.; Marks, G. B.; Marks, R.; Matsumori, A.; Matzopoulos, R.; Mayosi, B. M.; McAnulty, J. H.; McDermott, M. M.; McGrath, J.; Memish, Z. A.; Mensah, G. A.; Merriman, T. R.; Michaud, C.; Miller, M.; Miller, T. R.; Mock, C.; Mocumbi, A. O.; Mokdad, A. A.; Moran, A.; Mulholland, K.; Nair, M. N.; Naldi, L.; Narayan, K. M. V.; Nasseri, K.; Norman, P.; O'Donnell, M.; Omer, S. B.; Ortblad, K.; Osborne, R.; Ozgediz, D.; Pahari, B.; Pandian, J. D.; Rivero, A. P.; Padilla, R. P.; Perez-Ruiz, F.; Perico, N.; Phillips, D.; Pierce, K.; Pope, C. A.; Porrini, E.; Pourmalek, F.; Raju, M.; Ranganathan, D.; Rehm, J. T.; Rein, D. B.; Remuzzi, G.; Rivara, F. P.; Roberts, T.; De León, F. R.; Rosenfeld, L. C.; Rushton, L.; Sacco, R. L.; Salomon, J. A.; Sampson, U.; Sanman, E.; Schwebel, D. C.; Segui-Gomez, M.; Shepard, D. S.; Singh, D.; Singleton, J.; Sliwa, K.; Smith, E.; Steer, A.; Taylor, J. A.; Thomas, B.; Tleyjeh, I. M.; Towbin, J. A.; Truelsen, T.; Undurraga, E. A.; Venketasubramanian, N.; Vijayakumar, L.; Vos, T.; Wagner, G. R.; Wang, M.; Wang, W.; Watt, K.; Weinstock, M. A.; Weintraub, R.; Wilkinson, J. D.; Woolf, A. D.; Wulf, S.; Yeh, P.-H.; Yip, P.; Zabetian, A.; Zheng, Z.-J.; Lopez, A. D.; Murray, C. J. Global and Regional Mortality from 235 Causes of Death for 20 Age Groups in 1990 and 2010: A Systematic Analysis for the Global Burden of Disease Study 2010. *The Lancet* **2012**, *380* (9859), 2095–2128. https://doi.org/10.1016/S0140-6736(12)61728-0.

(58) Okumura, N.; Terasawa, F.; Haneishi, A.; Fujihara, N.; Hirota-Kawadobora, M.; Yamauchi, K.; Ota, H.; Lord, S. T. B:B Interactions Are Essential for Polymerization of

Variant Fibrinogens with Impaired Holes 'a.' *J. Thromb. Haemost.* **2007**, *5* (12), 2352–2359. https://doi.org/10.1111/j.1538-7836.2007.02793.x.
(59) Spraggon, G.; Everse, S. J.; Doolittle, R. F. Crystal Structures of Fragment D from Human Fibrinogen and Its Crosslinked Counterpart from Fibrin. *Nature* **1997**, *389* (6650), 455–462. https://doi.org/10.1038/38947.
(60) Budzynski, A. Z.; Olexa, S. A.; Pandya, B. V. Fibrin Polymerization Sites in Fibrinogen and Fibrin Fragments. *Ann. N. Y. Acad. Sci.* **1983**, *408*, 301–314. https://doi.org/10.1111/j.1749-6632.1983.tb23253.x.
(61) Yang, Z.; Mochalkin, I.; Doolittle, R. F. A Model of Fibrin Formation Based on Crystal Structures of Fibrinogen and Fibrin Fragments Complexed with Synthetic Peptides. *Proc. Natl. Acad. Sci.* **2000**, *97* (26), 14156–14161. https://doi.org/10.1073/pnas.97.26.14156.
(62) Lord, S. T. Molecular Mechanisms Affecting Fibrin Structure and Stability. *Arterioscler. Thromb. Vasc. Biol.* **2011**, *31* (3), 494–499. https://doi.org/10.1161/ATVBAHA.110.213389.
(63) Blomblckl, B.; Carlsson, K.; Fatah, K.; Hesse, B. Fibrin in Human Plasma: Gel Architectures Governed by Rate and Nature of Fibrinogen Activation. *Thromb. Res.* **1994**, *75* (5), 18.
(64) Kattula, S.; Byrnes, J. R.; Wolberg, A. S. Fibrinogen and Fibrin in Hemostasis and Thrombosis. *Arterioscler. Thromb. Vasc. Biol.* **2017**, *37* (3). https://doi.org/10.1161/ATVBAHA.117.308564.
(65) Nossel, H. L. Differential Consumption of Coagulation Factors Resulting from Activation of the Extrinsic (Tissue Thromboplastin) or the Intrinsic (Foreign Surface Contact) Pathways. *Blood* **1967**, *29* (3), 331–340. https://doi.org/10.1182/blood.V29.3.331.331.
(66) Smith, S. A.; Travers, R. J.; Morrissey, J. H. How It All Starts: Initiation of the Clotting Cascade. *Crit. Rev. Biochem. Mol. Biol.* **2015**, *50* (4), 326–336. https://doi.org/10.3109/10409238.2015.1050550.
(67) Lin, E.-W.; Boehnke, N.; Maynard, H. D. Protein–Polymer Conjugation via Ligand Affinity and Photoactivation of Glutathione *S* -Transferase. *Bioconjug. Chem.* **2014**, *25* (10), 1902–1909. https://doi.org/10.1021/bc500380r.
(68) Prucker, O.; Brandstetter, T.; Rühe, J. Surface-Attached Hydrogel Coatings via C,H-Insertion Crosslinking for Biomedical and Bioanalytical Applications (Review). *Biointerphases* **2018**, *13* (1), 010801. https://doi.org/10.1116/1.4999786.
(69) Lancaster, J. R.; Smilowitz, R.; Turro, N. J.; Koberstein, J. T. 1H NMR Study of Hydrogen Abstraction in Model Compound Mimics of Polymers. *Photochem. Photobiol.* **2014**, *90* (2), 394–401. https://doi.org/10.1111/php.12214.
(70) Li, M.; Fromel, M.; Ranaweera, D.; Rocha, S.; Boyer, C.; Pester, C. W. SI-PET-RAFT: Surface-Initiated Photoinduced Electron Transfer-Reversible Addition–Fragmentation Chain Transfer Polymerization. *ACS Macro Lett.* **2019**, *8* (4), 374–380. https://doi.org/10.1021/acsmacrolett.9b00089.
(71) Shanmugam, S.; Xu, J.; Boyer, C. Exploiting Metalloporphyrins for Selective Living Radical Polymerization Tunable over Visible Wavelengths. *J. Am. Chem. Soc.* **2015**, *137* (28), 9174–9185. https://doi.org/10.1021/jacs.5b05274.
(72) Ng, G.; Yeow, J.; Xu, J.; Boyer, C. Application of Oxygen Tolerant PET-RAFT to Polymerization-Induced Self-Assembly. *Polym. Chem.* **2017**, *8* (18), 2841–2851. https://doi.org/10.1039/C7PY00442G.

(73) Mei, N.; Chen, G.; Zhou, P.; Chen, X.; Shao, Z.-Z.; Pan, L.-F.; Wu, C.-G. Biocompatibility of Poly(ε-Caprolactone) Scaffold Modified by Chitosan—The Fibroblasts Proliferation in Vitro. *J. Biomater. Appl.* **2005**, *19* (4), 323–339. https://doi.org/10.1177/0885328205048630.
(74) Park, H.-S.; Gong, M.-S.; Knowles, J. C. Synthesis and Biocompatibility Properties of Polyester Containing Various Diacid Based on Isosorbide. *J. Biomater. Appl.* **2012**, *27* (1), 99–109. https://doi.org/10.1177/0885328212447245.
(75) Sato, T.; Dunderdale, G. J.; Hozumi, A. Simple and Scalable Protocol for Producing Hydrophobic Polymer Brushes Beyond Wafer-Scale Dimensions toward Real-Life Applications. *ACS Appl. Polym. Mater.* **2021**, *3* (3), 1395–1405. https://doi.org/10.1021/acsapm.0c01244.
(76) Ziemann, E.; Coves, T.; Levin, O.; Bernstein, R. Zwitterion Polymer Brushes on Porous Membranes: Characterization, Tribology, Performance, and the Effect of Electrolyte Anions. *ACS Appl. Polym. Mater.* **2020**, *2* (11), 4613–4625. https://doi.org/10.1021/acsapm.0c00686.
(77) Jordan, A. M.; Korley, L. T. J. Toward a Tunable Fibrous Scaffold: Structural Development during Uniaxial Drawing of Coextruded Poly(ε-Caprolactone) Fibers. *Macromolecules* **2015**, *48* (8), 2614–2627. https://doi.org/10.1021/acs.macromol.5b00370.
(78) Liu, P.; Su, Z. Surface-Initiated Atom Transfer Radical Polymerization (SI-ATRP) of Styrene from Chitosan Particles. *Mater. Lett.* **2006**, *60* (9–10), 1137–1139. https://doi.org/10.1016/j.matlet.2005.10.094.
(79) Negmadjanov, U.; Godic, Z.; Rizvi, F.; Emelyanova, L.; Ross, G.; Richards, J.; Holmuhamedov, E. L.; Jahangir, A. TGF-B1-Mediated Differentiation of Fibroblasts Is Associated with Increased Mitochondrial Content and Cellular Respiration. *PLOS ONE* **2015**, *10* (4), e0123046. https://doi.org/10.1371/journal.pone.0123046.
(80) Sung, J. Y.; Yoon, K.; Ye, S.-K.; Goh, S.-H.; Park, S.-Y.; Kim, J. H.; Kang, H. G.; Kim, Y.-N.; Park, B.-K. Upregulation of Transforming Growth Factor-Beta Type I Receptor by Interferon Consensus Sequence-Binding Protein in Osteosarcoma Cells. *Biochim. Biophys. Acta BBA - Mol. Cell Res.* **2019**, *1866* (5), 761–772. https://doi.org/10.1016/j.bbamcr.2019.01.015.
(81) Gilbert, R.; Vickaryous, M.; Viloria-Petit, A. Signalling by Transforming Growth Factor Beta Isoforms in Wound Healing and Tissue Regeneration. *J. Dev. Biol.* **2016**, *4* (2), 21. https://doi.org/10.3390/jdb4020021.
(82) Grotendorst, G. R.; Rahmanie, H.; Duncan, M. R. Combinatorial Signaling Pathways Determine Fibroblast Proliferation and Myofibroblast Differentiation. *FASEB J.* **2004**, *18* (3), 469–479. https://doi.org/10.1096/fj.03-0699com.
(83) Pangilinan, K. D.; de Leon, A. C. C.; Mangadlao, J. D.; Baer, E.; Advincula, R. C. Grafting of a Stimuli Responsive Polymer on Nanolayered Coextruded PS/PCL Films by Surface Initiated Polymerization. *Macromol. Mater. Eng.* **2016**, *301* (7), 870–875. https://doi.org/10.1002/mame.201600019.
(84) Sperling, C.; Fischer, M.; Maitz, M. F.; Werner, C. Blood Coagulation on Biomaterials Requires the Combination of Distinct Activation Processes. *Biomaterials* **2009**, *30* (27), 4447–4456. https://doi.org/10.1016/j.biomaterials.2009.05.044.
(85) Shiu, H. T.; Goss, B.; Lutton, C.; Crawford, R.; Xiao, Y. Controlling Whole Blood Activation and Resultant Clot Properties by Carboxyl and Alkyl Functional Groups on

Material Surfaces: A Possible Therapeutic Approach for Enhancing Bone Healing. *J Mater Chem B* **2014**, *2* (20), 3009–3021. https://doi.org/10.1039/C4TB00009A.
(86) Rausch, M. K.; Parekh, S. H.; Dortdivanlioglu, B.; Rosales, A. M. Synthetic Hydrogels as Blood Clot Mimicking Wound Healing Materials. *Prog. Biomed. Eng.* **2021**, *3* (4), 042006. https://doi.org/10.1088/2516-1091/ac23a4.
(87) Arul, G.; Bowley, D.; DiRusso, S. The Use Of Celox™ Gauze as an Adjunct to Pelvic Packing in Otherwise Uncontrollable Pelvic Haemorrhage Secondary to Penetrating Trauma. *J. R. Army Med. Corps* **2012**, *158* (4), 331–334. https://doi.org/10.1136/jramc-158-04-12.
(88) Ayres, N.; Holt, D. J.; Jones, C. F.; Corum, L. E.; Grainger, D. W. Polymer Brushes Containing Sulfonated Sugar Repeat Units: Synthesis, Characterization, and *in Vitro* Testing of Blood Coagulation Activation. *J. Polym. Sci. Part Polym. Chem.* **2008**, *46* (23), 7713–7724. https://doi.org/10.1002/pola.23075.
(89) Salvagno, G. L.; Berntorp, E. Thrombin Generation Assays (TGAs). In *Hemostasis and Thrombosis*; Favaloro, E. J., Lippi, G., Eds.; Methods in Molecular Biology; Springer New York: New York, NY, 2017; Vol. 1646, pp 515–522. https://doi.org/10.1007/978-1-4939-7196-1_37.
(90) Förch, R.; Schönherr, H.; Jenkins, A. T. A. *Surface Design: Applications in Bioscience and Nanotechnology*; John Wiley & Sons, 2009.
(91) Calcium and Blood Coagulation. *Proc. R. Soc. Lond. Ser. B - Biol. Sci.* **1940**, *128* (851), 201–213. https://doi.org/10.1098/rspb.1940.0005.
(92) Mann, K. G.; Whelihan, M. F.; Butenas, S.; Orfeo, T. Citrate Anticoagulation and the Dynamics of Thrombin Generation. *J. Thromb. Haemost.* **2007**, *5* (10), 2055–2061. https://doi.org/10.1111/j.1538-7836.2007.02710.x.
(93) Ryan, E. A.; Mockros, L. F.; Weisel, J. W.; Lorand, L. Structural Origins of Fibrin Clot Rheology. *Biophys. J.* **1999**, *77* (5), 2813–2826. https://doi.org/10.1016/S0006-3495(99)77113-4.
(94) Nagata, S.; Atkinson, G. M.; Pestov, D.; Tepper, G. C.; Mcleskey, J. T. Electrospun Polymer-Fiber Solar Cell. *Adv. Mater. Sci. Eng.* **2013**, *2013*, 1–6. https://doi.org/10.1155/2013/975947.
(95) Oliveira, J. E.; Medeiros, E. S.; Cardozo, L.; Voll, F.; Madureira, E. H.; Mattoso, L. H. C.; Assis, O. B. G. Development of Poly(Lactic Acid) Nanostructured Membranes for the Controlled Delivery of Progesterone to Livestock Animals. *Mater. Sci. Eng. C* **2013**, *33* (2), 844–849. https://doi.org/10.1016/j.msec.2012.10.032.
(96) Lyu, S.; Huang, C.; Yang, H.; Zhang, X. Electrospun Fibers as a Scaffolding Platform for Bone Tissue Repair. **2013**, 8.
(97) Kim, S.-E.; Jordan, A. M.; Korley, L. T. J.; Pokorski, J. K. Drawing in Poly(ε-Caprolactone) Fibers: Tuning Mechanics, Fiber Dimensions and Surface-Modification Density. *J. Mater. Chem. B* **2017**, *5* (23), 4499–4506. https://doi.org/10.1039/C7TB00096K.
(98) Neises, B.; Steglich, W. Simple Method for the Esterification of Carboxylic Acids. *Angew. Chem. Int. Ed. Engl.* **1978**, *17* (7), 522–524. https://doi.org/10.1002/anie.197805221.
(99) Woodruff, M. A.; Hutmacher, D. W. The Return of a Forgotten Polymer—Polycaprolactone in the 21st Century. *Prog. Polym. Sci.* **2010**, *35* (10), 1217–1256. https://doi.org/10.1016/j.progpolymsci.2010.04.002.

(100) Pal, J.; Kankariya, N.; Sanwaria, S.; Nandan, B.; Srivastava, R. K. Control on Molecular Weight Reduction of Poly(ε-Caprolactone) during Melt Spinning — A Way to Produce High Strength Biodegradable Fibers. *Mater. Sci. Eng. C* **2013**, *33* (7), 4213–4220. https://doi.org/10.1016/j.msec.2013.06.011.
(101) Agarwal, K.; Sharma, A.; Talukder, G. Effects of Copper on Mammalian Cell Components. *Chem. Biol. Interact.* **1989**, *69* (1), 1–16. https://doi.org/10.1016/0009-2797(89)90094-X.
(102) Li, J.; Yun, H.; Gong, Y.; Zhao, N.; Zhang, X. Investigation of MC3T3-E1 Cell Behavior on the Surface of GRGDS-Coupled Chitosan. *Biomacromolecules* **2006**, *7* (4), 1112–1123. https://doi.org/10.1021/bm050913r.
(103) Hersel, U.; Dahmen, C.; Kessler, H. RGD Modified Polymers: Biomaterials for Stimulated Cell Adhesion and Beyond. *Biomaterials* **2003**, *24* (24), 4385–4415. https://doi.org/10.1016/S0142-9612(03)00343-0.
(104) Bellis, S. L. Advantages of RGD Peptides for Directing Cell Association with Biomaterials. *Biomaterials* **2011**, *32* (18), 4205–4210. https://doi.org/10.1016/j.biomaterials.2011.02.029.
(105) Engler, A. J.; Sen, S.; Sweeney, H. L.; Discher, D. E. Matrix Elasticity Directs Stem Cell Lineage Specification. *Cell* **2006**, *126* (4), 677–689. https://doi.org/10.1016/j.cell.2006.06.044.
(106) Oldenbourg, R. Polarized Light Microscopy: Principles and Practice. *Cold Spring Harb. Protoc.* **2013**, *2013* (11), pdb.top078600. https://doi.org/10.1101/pdb.top078600.
(107) Zhan, A.; Colburn, S.; Dodson, C. M.; Majumdar, A. Metasurface Freeform Nanophotonics. *Sci. Rep.* **2017**, *7* (1), 1673. https://doi.org/10.1038/s41598-017-01908-9.
(108) Pan, Y.; Xue, Y.; Snow, J.; Xiao, H. Tailor-Made Antimicrobial/Antiviral Star Polymer via ATRP of Cyclodextrin and Guanidine-Based Macromonomer. *Macromol. Chem. Phys.* **2015**, *216* (5), 511–518. https://doi.org/10.1002/macp.201400525.
(109) Mouritz, A. P.; Galos, J.; Linklater, D. P.; Ladani, R. B.; Kandare, E.; Crawford, R. J.; Ivanova, E. P. Towards Antiviral Polymer Composites to Combat COVID-19 Transmission. *Nano Sel.* **2021**, *2* (11), 2061–2071. https://doi.org/10.1002/nano.202100078.
(110) Herold, B. C.; Scordi-Bello, I.; Cheshenko, N.; Marcellino, D.; Dzuzelewski, M.; Francois, F.; Morin, R.; Casullo, V. M.; Anderson, R. A.; Chany, C.; Waller, D. P.; Zaneveld, L. J. D.; Klotman, M. E. Mandelic Acid Condensation Polymer: Novel Candidate Microbicide for Prevention of Human Immunodeficiency Virus and Herpes Simplex Virus Entry. *J. Virol.* **2002**, *76* (22), 11236–11244. https://doi.org/10.1128/JVI.76.22.11236-11244.2002.
(111) Zaneveld, L. J. D.; Waller, D. P.; Anderson, R. A.; Chany, C.; Rencher, W. F.; Feathergill, K.; Diao, X.-H.; Doncel, G. F.; Herold, B.; Cooper, M. Efficacy and Safety of a New Vaginal Contraceptive Antimicrobial Formulation Containing High Molecular Weight Poly(Sodium 4-Styrenesulfonate)1. *Biol. Reprod.* **2002**, *66* (4), 886–894. https://doi.org/10.1095/biolreprod66.4.886.
(112) Carraher, C. E.; Sabir, T. S.; Roner, M. R.; Shahi, K.; Bleicher, R. E.; Roehr, J. L.; Bassett, K. D. Synthesis of Organotin Polyamine Ethers Containing Acyclovir and Their Preliminary Anticancer and Antiviral Activity. *J. Inorg. Organomet. Polym. Mater.* **2006**, *16* (3), 249–257. https://doi.org/10.1007/s10904-006-9050-y.

(113) Swift, T.; Caseley, E.; Pinnock, A.; Shepherd, J.; Shivshetty, N.; Garg, P.; Ian Douglas, C. W.; MacNeil, S.; Rimmer, S. Branched Amphotericin Functional Poly(*N* - *Iso* Propyl Acrylamide): An Antifungal Polymer. *R. Soc. Open Sci.* **2021**, *8* (1), 201655. https://doi.org/10.1098/rsos.201655.
(114) Hassan, M. M. Binding of a Quaternary Ammonium Polymer-Grafted-Chitosan onto a Chemically Modified Wool Fabric Surface: Assessment of Mechanical, Antibacterial and Antifungal Properties. *RSC Adv.* **2015**, *5* (45), 35497–35505. https://doi.org/10.1039/C5RA03073K.
(115) Haley, R. M.; Zuckerman, S. T.; Gormley, C. A.; Korley, J. N.; von Recum, H. A. Local Delivery Polymer Provides Sustained Antifungal Activity of Amphotericin B with Reduced Cytotoxicity. *Exp. Biol. Med.* **2019**, *244* (6), 526–533. https://doi.org/10.1177/1535370219837905.
(116) Fang, R. H.; Hu, C.-M. J.; Zhang, L. Nanoparticles Disguised as Red Blood Cells to Evade the Immune System. *Expert Opin. Biol. Ther.* **2012**, *12* (4), 385–389. https://doi.org/10.1517/14712598.2012.661710.
(117) Liu, Q.; Jia, J.; Yang, T.; Fan, Q.; Wang, L.; Ma, G. Pathogen-Mimicking Polymeric Nanoparticles Based on Dopamine Polymerization as Vaccines Adjuvants Induce Robust Humoral and Cellular Immune Responses. *Small* **2016**, *12* (13), 1744–1757. https://doi.org/10.1002/smll.201503662.
(118) Bałazy, A.; Toivola, M.; Adhikari, A.; Sivasubramani, S. K.; Reponen, T.; Grinshpun, S. A. Do N95 Respirators Provide 95% Protection Level against Airborne Viruses, and How Adequate Are Surgical Masks? *Am. J. Infect. Control* **2006**, *34* (2), 51–57. https://doi.org/10.1016/j.ajic.2005.08.018.
(119) Campos, R. K.; Jin, J.; Rafael, G. H.; Zhao, M.; Liao, L.; Simmons, G.; Chu, S.; Weaver, S. C.; Chiu, W.; Cui, Y. Decontamination of SARS-CoV-2 and Other RNA Viruses from N95 Level Meltblown Polypropylene Fabric Using Heat under Different Humidities. *ACS Nano* **2020**, *14* (10), 14017–14025. https://doi.org/10.1021/acsnano.0c06565.
(120) Lv, H.; Li, L.; Sun, M.; Zhang, Y.; Chen, L.; Rong, Y.; Li, Y. Mechanism of Regulation of Stem Cell Differentiation by Matrix Stiffness. *Stem Cell Res. Ther.* **2015**, *6* (1), 103. https://doi.org/10.1186/s13287-015-0083-4.